Bridgette Webb, MSc

Post-mortem MR imaging techniques for the assessment of sudden cardiac death: Quantitative and angiography-based approaches

DOCTORAL THESIS

to achieve the university degree of

Doktorin der technischen Wissenschaften

submitted to

Graz University of Technology

Supervisor

Univ.-Prof. Dipl-Ing. Dr.techn. Rudolf Stollberger
Institute for Medical Engineering

Graz, April 2018

Affidavit

I declare that I have authored this thesis independently, that I have not used other than the declared sources/resources, and that I have explicitly indicated all material which has been quoted either literally or by content from the sources used. The text document uploaded to TUGRAZ online is identical to the present doctoral thesis.

Date	Signature

Eidesstattliche Erklärung

Ich erkläre an Eides statt, dass ich die vorliegende Arbeit selbstständig verfasst, andere als die angegebenen Quellen/Hilfsmittel nicht benutzt, und die den benutzten Quellen wörtlich und inhaltlich entnommenen Stellen als solche kenntlich gemacht habe. Das in TUGRAZ online hochgeladene Textdokument ist mit der vorliegenden Dissertation identisch.

Datum	Unterschrift

Abstract

Assessment of sudden cardiac death (SCD), specifically SCD related to acute coronary events and acute myocardial infarction, represents the diagnostic context for the evaluation of post-mortem magnetic resonance imaging (PMMR) techniques presented in this thesis. To date, research in this area has primarily focussed on visualising vessels and calcifications using post-mortem computed tomography angiography (PMCTA) and on the quantification of tissue alterations in post-mortem myocardium using accelerated quantitative PMMR. Through systematic investigation of the premises and considerations for performance of post-mortem MR angiography (PMMRA) and presentation of additional quantitative MR imaging techniques for the assessment of acute myocardial infarction, this thesis advances research regarding the radiological assessment of cardiac causes of death.

Systematic evaluation commenced with the characterisation of viscosity and MR relaxation properties (T_1, T_2) of candidate perfusates for PMMRA at temperatures between 1-23°C. Perfusates demonstrating stable, medium dynamic viscosity (20-100 mPa·s) and T_1 relaxation times at least 100 ms below corresponding cadaveric tissue (myocardium, fat) were preferred for angiography-based post-mortem MR of the coronary arteries. Clinically available MR sequences such as T2w SPACE and T1w gradient echo (GRE) delivered high contrast between perfusates and surrounding tissue as well as good spatial resolution for the assessment of filled vessel-like structures similar in size to human coronary arteries.

The visualisation and intravascular retention of three selected perfusates (paraffin oil, polyethylene glycol (PEG) 200 and Gadovist®-doped physiological solution) were quantitatively investigated in an *ex situ* porcine heart model. At 23-25°C all perfusates demonstrated an excellent contrast-to-noise ratio with post-mortem myocardium and epicardial fat using a 3D T1w GRE sequence. Fast perfusate extravasation ($<$ 1 hour) was observed for PEG200 and the Gadovist® solution, as evidenced by statistically significant changes in the signal intensity of the filled vessel and T_1 relaxation times in adjacent myocardium in this time. Conversely, paraffin oil remained intravascular for the entire duration of the experiment (12 hours). The technical feasibility of paraffin oil as perfusate in combination with 3D T1-weighted imaging sequences could be successfully demonstrated in a forensic cohort, where PMMRA was performed directly following PMCTA using 6% paraffin oil & Angiofil®.

Additionally, quantitative MR imaging was applied in a preclinical porcine heart model to characterise early tissue alterations in post-mortem myocardium following fatal induced myocardial infarction. Longitudinal and transverse relaxation times, as well as diffusion parameters such as fractional anisotropy (FA) and mean diffusivity (MD) were examined in infarcted and remote regions of the myocardium. While observed trends in FA and MD were not found to be statistically significant in this study, T_1 and T_2 relaxation times were found to be shortened in the infarcted regions compared with remote regions (p-value < 0.05).

Kurzfassung

Die Befundung von plötzlichem Herztod, insbesondere in Zusammenhang mit einem akuten Ereignis, stellt den diagnostischen Rahmen für die Evaluierung von postmortaler Magnetresonanztomographie (PMMR), die in dieser Arbeit präsentiert wird, dar. Bisher liegt der Fokus der Forschung in diesem Bereich auf der Darstellung von postmortalen Gefäßen und Verkalkungen mittels postmortaler Computertomographie Angiographie (PMCTA) und der Quantifizierung von Änderungen im *ex vivo* Myokard anhand von beschleunigter quantitativer PMMR. Durch die systematische Methodenentwicklung für die Durchführung der postmortalen MR Angiographie (PMMRA) und Untersuchung von zusätzlichen quantitativen MRT-Ansätzen für die Charakterisierung von akutem Myokardinfarkt, trägt diese Doktorarbeit zur Weiterentwicklung des Forschungsgebiets und zur Verbesserung der radiologischen Befundung von kardiovaskulären Todesursachen bei.

Zu Beginn der systematischen Methodenentwicklung wurden die Viskosität und MR Relaxationszeiten (T_1, T_2) von Kandidatenperfusaten für den Temperaturbereich von 1 bis 23°C untersucht. Perfusate mit stabiler, mittelmäßiger Viskosität (20-100 mPa·s) und T_1 Relaxationszeiten mindesten 100 ms kurzer als Leichengewebe (z.B. Myokard, Fett) wurden für einen PMMRA Ansatz in den Koronararterien herangezogen. Klinisch verfügbare MR Sequenzen, z.B. T2w SPACE und T1w Gradientenecho (GRE), lieferten sowohl guten Kontrast zwischen Perfusaten und dem umliegenden Gewebe als auch eine gute räumliche Auflösung, die auch für die Beurteilung von menschlichen Koronararterien geeignet war.

Die Darstellung und intravaskuläre Retention von drei ausgewählten Perfusaten (Paraffinöl, Polyethylenglykol (PEG) 200 und Gadovist® in physiologischer Lösung) wurden anhand eines *ex situ / ex vivo* Schweinherzmodells untersucht. In 3D T1w GRE Bilddaten bei 23-25 °C zeigten alle Perfusaten ein exzellentes Kontrast-Rausch-Verhältnis, sowohl gegenüber postmortalem Myokard als auch Fett. Der Perfusataustritt fand bei PEG200 und bei der Gadovist® Lösung sehr schnell ($<$ 1 Stunde) statt, was sich durch einen statistisch signifikanten Unterschied in der Signalintensität und T_1 Zeiten im gefüllten Gefäß und umliegenden Myokard gezeigt hat. Paraffinöl wiederum blieb intravaskulär für die gesamte Dauer der Untersuchungen (12 Stunden). Die technische Machbarkeit des Einsatzes von Paraffinöl in Kombination mit zwei 3D T1-gewichteten MR Sequenzen konnte erfolgreich durch die Anwendung von PMMRA an Leichen unmittelbar nach PMCTA mit 6% Paraffinöl & Angiofil® gezeigt werden.

Zusätzlich zur Charakterisierung und Anwendung der Perfusate wurde quantitative MRT an einem präklinischen Schweineherzmodell angewandt, um postmortale Gewebeänderungen in der Frühphase nach der Induzierung eines tödlichen Herzinfarktes darzustellen. Sowohl MR Relaxationszeiten als auch Diffusionseigenschaften wie *fractional anisotropy* (FA) und *mean diffusivity* (MD) wurden im Infarktareal und im nicht pathologischen Myokard untersucht. In dieser Studie waren Unterschiede in Bezug auf FA und MD nicht statistisch signifikant, T_1 und T_2 Relaxationszeiten waren jedoch kurzer in den Infarktarealen (p-value < 0.05).

Acknowledgements

Firstly, I would like to thank Eva Scheurer. Her confidence in me sparked my move to Graz, a city I had barely heard of, let alone dreamed of someday calling home. Secondly, I acknowledge the generous financial support of the Austrian Academy of Sciences, who enabled the research conducted for this thesis. Thirdly, I would like to thank my supervisor Rudolf Stollberger for his guidance through the perplexing world of MRI. In particular, thank you for the opportunity to complete my thesis under your supervision, for your questions, which I at times didn't know how to answer and for the technical perspectives you have offered me during the past years.

I express my immense gratitude to all of the team members at the LBI CFI, past and present, who have supported, encouraged and motivated me since my arrival in Graz. Specifically, I would like to thank Reingard Riener-Hofer for her constant positivity towards my research and ideas as well as Thorsten Schwark for his assistance in grasping the medical aspects related to sudden cardiac death. For her office companionship, unwaivering support and patience I express my sincere thanks to Sylvia Scheicher, whom it has been a pleasure to work with and who always made time to help me with everything from funding applications to German grammar. From the LBI CFI team I would also like to particularly thank Thomas Widek for the countless hours we spent scanning to acquire much of the data presented in this thesis, Bernhard Neumayer and Johannes Höller for their ongoing willingness to 'fix' my computer and finally Hanna Sprenger, Sophie Kerbacher and Katharina Baron - our interdisciplinary stress management endeavours continuously provided much needed moral and physical strength, thank you all!

I would additionally like to thank the entire team at the CURML and in particular, Silke Grabherr for her interest in and endorsement of my project right from the beginning. I am thankful for the time I was able to spend at the CURML during my thesis and for our close collaboration, which I hope will continue to flourish in the coming years. From Lausanne, I would specifically like to thank Christine Bruguier. Thanks for patiently answering my questions, for teaching me the ins and outs of the Philips MR system and for being amazingly dedicated to recruitment for my project - without you, there probably would not be a Chapter 7.

It is a pleasure to acknowledge Martin Manninger-Wünscher for his steady hand and cardiological insights during preclinical experiments, Marlene Leoni, for her preparation and interpretation of histological samples and Christoph Aigner for his perceptive proofreading skills, your comments greatly helped and motivated me in the last stage of writing.

I extend my deepest gratitude to my friends, in particular Mariève, Danni and Gwen, although we are scattered around the world, you always manage to offer perfectly timed motivation and/or distraction. To my parents, thank you for having always encouraged and supported me and for having given me the confidence to try anything. Finally, I would like to thank Lukas, I am forever grateful for your love and kindness as well as your support and constant reminders to eat and sleep during the final phases of this thesis.

Contents

List of abbreviations

Abbreviations frequently used in this thesis are listed below:

ADC	Apparent diffusion coefficient
ANOVA	Analysis of variance
ATP	Adenosine triphosphate
BR	Block radius
BW	Bandwidth
CAD	Coronary artery disease
CNR	Contrast-to-noise ratio
CNR_{eff}	Effective contrast to noise ratio
CURML	University Center of Legal Medicine (Lausanne-Geneva)
DTI	Diffusion tensor imaging
EPI	Echo planar imaging
ETL	Echo train length
FA	Flip angle
FOV	Field-of-view
GPAPPA	Generalized autocalibrating partial parallel acquisition
GRE	Gradient echo
IHC	Immunohistochemistry
IHD	Ischaemic heart disease
IQR	Inter-quartile range
IR-SE	Inversion recovery spin echo
LAD	Left anterior descending
LCX	Left circumflex
MD	Mean diffusivity
MI	Myocardial infarction
MIP	Maximum intensity projection
MOLLI	Modified Look-Locker inversion recovery
MPMCTA	Multi-phase post-mortem computed tomography angiography
MRI	Magnetic resonance imaging
MSE	Multi-echo spin echo
NLM	Non-local means
PEG	Polyethylene glycol
PMCT	Post-mortem computed tomography
PMCTA	Post-mortem computed tomography angiography
PMI	Post-mortem interval
PMMR	Post-mortem magnetic resonance (imaging)
PMMRA	Post-mortem magnetic resonance angiography
PR	Patch radius
RCA	Right coronary artery
RMSE	Root mean square error
ROI	Region-of-interest
RSD	Relative standard deviation
RSE	Residual standard error
SASHA	Saturation recovery single-shot acquisition
SCD	Sudden cardiac death
SD	Standard deviation
SI	Signal intensity
SNR	Signal-to-noise ratio
SPACE	Sampling perfection with application optimized contrasts using different flip angle evolution
STEMI	ST-elevation myocardial infarction
TA	Acquisition time
TE	Echo time
TI	Inversion time
TIR	Turbo inversion recovery
TOF	Time of flight
TR	Repetition time
TSE	Turbo spin echo
VOI	Volume-of-interest

1 Introduction

Forensic pathology and its primary objective, the determination of cause of death, represent the context for the systematic investigation of post-mortem magnetic resonance imaging (PMMR) techniques presented in this thesis. The corresponding diagnostic focus of these methods is the assessment of sudden cardiac death (SCD), specifically SCD due to early acute myocardial infarction (MI) (survival time $<$ 6-8 hours). The reliable detection and evaluation of early acute MI is a current challenge not only for post-mortem imaging, but also during conventional autopsy. Therefore, there is a need to systematically investigate novel imaging approaches to improve the post-mortem radiological assessment of acute MI and its common cause, coronary artery disease (CAD). Current post-mortem imaging techniques mainly take advantage of computed tomography (CT)-based technologies, such as native post-mortem CT (PMCT) and post-mortem CT angiography (PMCTA). Increasingly, native magnetic resonance imaging (MRI) techniques are being implemented, although still to a lesser extent. A natural extension of the aforementioned techniques is post-mortem magnetic resonance angiography (PMMRA). The systematic evaluation of possible approaches to PMMRA and the potential combination of quantitative MR imaging approaches to improve the post-mortem radiological evaluation of acute cardiovascular pathologies has not yet been performed. These investigations form the fundamental basis of this thesis.

1.1 Research questions

It is hypothesised that PMMRA can offer enhanced **visualisation of the coronary arteries**, compared with native MRI. Additionally, it is hypothesised that PMMRA can enable **improved characterisation of infarcted and normal myocardium**, compared to CT. PMMRA can be viewed as the fusion of angiographic (vascular) information and parametric, tissue-specific (pathological) information. The research questions posed in this work are therefore initially approached separately to address these two aspects before being combined to evaluate the feasibility of PMMRA as a whole.

1.1.1 Vascular visualisation

The first part of this thesis will focus on the visualisation of post-mortem coronary arteries. This can be achieved based on principles similar to those found in clinical imaging, with two significant differences - flow and the liquid with which vessels are filled. In clinical practice,

(blood) flow is associated with both advantages (e.g. implementation of inflow-based and flow-encoding techniques) and disadvantages (e.g. motion artifacts caused by the beating heart, signal inhomogeneity in pooled blood). Furthermore, compared with post-mortem examinations, the possibilities for achieving contrast based on the relaxation properties of blood itself are limited in a clinical context. Either a contrast-enhanced approach (e.g. injection of contrast agent, such as gadolinium-based agents) or relaxation-based angiography, which seeks to exploit the intrinsic relaxation properties of blood itself can be applied. For post-mortem examinations, it is possible to approach the problem from a different direction, namely that a suitable liquid with which vessels can be filled can be pre-selected to achieve the desired contrast. This approach has already been explored in the context of post-mortem CT examinations, where radio-opaque contrast agents have been mixed with either a hydrophilic [1–3], hygroscopic [4–6] or lipophilic [7–9] solution and used to fill the vascular system in both targeted or whole body approaches. Given the complex mechanisms for generation of signal in MRI, the possibilities in this regard are even broader. Therefore, the selection of a suitable liquid lies at the centre of the research process to develop and implement PMMRA. Additionally, the determination and application of appropriate image acquisition techniques to further optimise image contrast and quality, given influences specific to post-mortem imaging (e.g. temperature), is essential.

The following specific research questions were determined to be relevant to the visualisation of the coronary arteries and will be explored in this thesis:

1. What are the physical and relaxation properties of perfusates potentially suitable for visualisation of post-mortem coronary arteries in MRI?
2. What is the temperature dependence of these properties?
3. Which MR sequences deliver sufficient resolution and contrast between filled vessels and post-mortem tissue?
4. How do perfusate characteristics influence intravascular retention in post-mortem coronary arteries?

1.1.2 Characterisation of post-mortem myocardium

In the second part of this work, focus is shifted to the evaluation of myocardial infarction, a common occurrence in cases of SCD. For this evaluation, preference was given to the implementation of parametric mapping techniques over morphological images. In clinical cardiac imaging practice, these techniques are increasingly considered to offer improved quantitative diagnostic value and higher comparability of data [10]. Furthermore, while clinical conditions often prevent the implementation of gold standard sequences for the

quantification of tissue relaxation and diffusion properties due to time constraints and associated complications, the post-mortem environment offers an excellent opportunity to investigate **alterations in the myocardium** due to infarction on imaging, macroscopic (*ex situ*) and histological levels. The following specific research questions will be addressed to investigate the quantitative MRI characteristics of post-mortem myocardium:

1. Can post-mortem myocardium be characterised using quantitative post-mortem MR imaging techniques?
2. Do quantitative parameters values differ in infarcted (ischaemic) and non-pathological post-mortem myocardium?

1.1.3 Feasibility of post-mortem MR angiography

Finally, the developed approach to PMMRA will be applied in a small cohort of forensic cadavers to determine its feasibility in cases of suspected SCD. The focus of this study is to investigate the feasibility of PMMRA following multi-phase PMCTA (MPMCTA) and to provide insight into the different MR imaging techniques which can be applied to visualise the vascular system. The following specific research questions will be addressed:

1. Is the performance of PMMRA following MPMCTA in feasible in routine forensic practice?
2. Which MR sequences are optimal for the visualisation of post-mortem reperfused cardiac vessels?

1.2 Forensic medicine

Forensic medicine describes the medical field responsible for determination of cause of injury and/or death, primarily as it relates to criminal investigations. The classical branch, forensic pathology (i.e. not clinical forensic medicine), involves the performance of medico-legal (forensic) autopsies and the documentation of associated findings and conclusions, in particular as they are relevant to cause, circumstances and time of death, as well as the identity of the deceased.

1.2.1 Role and importance of forensic pathology in determining cause of sudden death

Depending on the country and jurisdiction, the responsibility of determining cause of death falls to one or more administrative bodies and depending on the type of post-mortem medical examination, judicial, professional and medical consequences may ensue. Specialists responsible for performing clinical (pathological) autopsies are primarily concerned with diagnosis of underlying disease mechanisms which may have contributed to the death [11]. On the other hand, medico-legal (forensic) autopsies are performed primarily in cases of sudden, unnatural (violent), unexpected and in certain unwitnessed deaths, for example where suspicion of third-party involvement cannot be excluded [12]. In such cases, autopsies aim to establish the cause and circumstances of death, as well as to address questions of interest for investigating authorities, for example regarding identity and time of death [11]. Cases of sudden death can be examined in either of these settings [13]. The post-mortem examination generally seeks to establish whether the underlying condition may have been inherited, the possibility of toxic or illicit drug abuse, trauma and other unnatural causes and any potential role of third persons in the death [13]. In this context, the attribution of sudden death to a cardiac disease is assessed, including the nature of the cardiac disease and whether the mechanism of death was arrhythmic or mechanical.

With these purposes in mind, a conventional autopsy generally involves a thorough external and internal examination of the cadaver. In addition to the morphological observations documented during the autopsy itself, biological samples are also collected for histological, (bio)chemical and toxicological analysis which can offer additional relevant information, for example regarding prior medical conditions or the level of intoxication.

Although not the primary focus of forensic pathology, results of forensic examinations can also influence mortality statistics, indicate the health status of the population [14] and can provide family members with timely information, for example regarding genetic disorders [15].

1.2.2 Sudden cardiac death

Approximately 85-90% of all deaths in Germany can be classified as 'natural death' (manner of death), of which approximately 10-15% are classified as unexpected, sudden deaths [16]. The proportion of unexpected, sudden natural deaths with underlying cardiac causes is between 50-75% [16]. In cases of SCD, cause of death is determined to be either due to ischaemic heart disease (IHD) or one of a variety of non-coronary related causes (Figure

1.1), whereby IHD is further divided into two categories: atherosclerosis induced conditions and non-atherosclerotic causes [16]. In adults, IHD, also known as coronary heart disease or coronary artery disease (CAD), is by far the most frequent cause of SCD [16]. In addition to or independent of the presence of a cardiovascular substrate, such as CAD, an acute event or specific circumstances often contribute to sudden cardiac death. Predominant examples of such events are coronary occlusions or high-grade stenosis resulting from thrombosis or atherosclerotic plaque [16], which cause reduced perfusion, potentially leading to myocardial infarction, the induction of ventricular arrhythmia or sudden muscular dysfunction in the left ventricle [16].

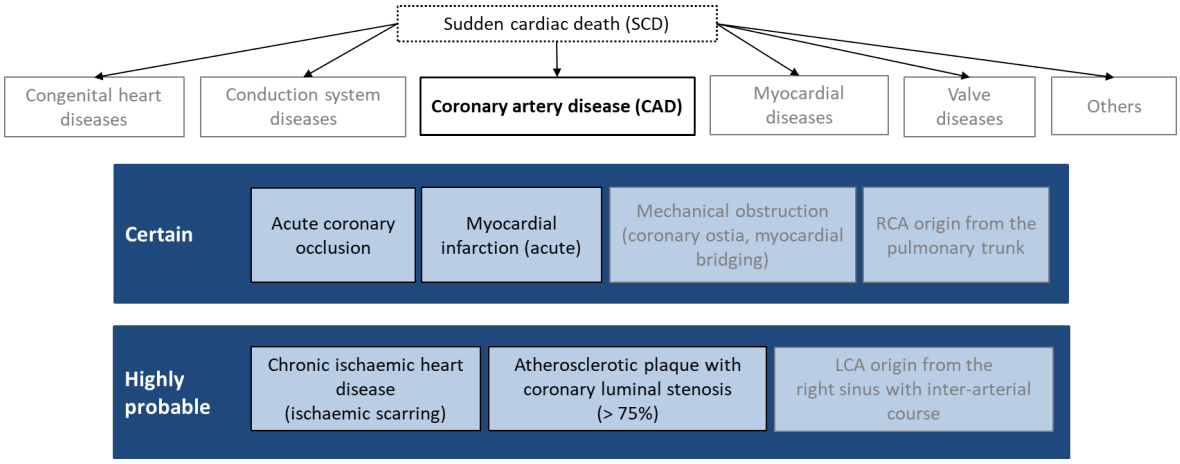

Figure 1.1: Post-mortem findings for the diagnosis of cardiovascular substrates of sudden cardiac death and their associated certainty (certain, highly probable) for coronary artery disease [13].

Although numerous cardiac conditions can lead to SCD (Figure 1.1), this work will focus on the MRI-based assessment of a single cardiovascular substrate of sudden cardiac death - coronary artery disease. As depicted in Figure 1.1, post-mortem findings commonly associated with a diagnosis of CAD include acute coronary occlusion, (acute) myocardial infarction, signs of chronic IHD and atherosclerotic plaque with coronary luminal stenosis of greater than 75%. The observation of these phenomena indicates, with various degrees of certainty, that the death in question can be attributed to CAD. The following sections discuss these findings and their significance in post-mortem investigations in more detail.

Acute coronary occlusion

An acute coronary occlusion refers to the sudden partial or complete obstruction of blood flow in a coronary artery, for example due to a thrombus, spasm or atherosclerosis [17]. A recent examination of the pathomorphological and CT-angiographical characteristics of coronary atherosclerotic plaques in cases of SCD found that when cause of death was mainly attributed to acute coronary artery thrombosis (n=57), these originated from either plaque

rupture or intra-plaque haemorrhage (n=31) or plaque erosion (n=26) [18]. These findings are approximately in line with the distribution of rupture (55-65%) and erosion (30-35%) in individuals dying suddenly with confirmation of coronary thrombus as determined by Virmani et al. [19]. The study by Michaud et al. [18] additionally demonstrated that approximately 70% and 84% of erosions and ruptures, respectively, were found in either the left anterior descending (LAD) or right coronary artery (RCA) and also that 82% of ruptures and 77% of erosions were localised in the proximal segment of the main coronary arteries [18]. According to an additional clinical study by Wang et al. [20] coronary occlusions leading to ST-elevation MI (STEMI) tend to cluster in the proximal third of each of the coronary arteries, with decreasing probability of an acute coronary occlusion as distance from the ostium increases. This indicates that proximal occlusions are more prevalent, or at least more frequently sympomatic, than their distal counterparts. Nevertheless, the obstructive effects of platelet aggregate and early fibrin formation on flow and blood coagulation are experienced both proximally and distally to the occlusion itself [21].

In a clinical context, the mechanisms and events leading to acute artery occlusion are important for diagnostic and therapeutic purposes. In particular, as depicted in Figure 1.2 a distinction is made between partial and complete occlusions, where partial occlusions generally lead to unstable angina and non-STEMI while complete occlusions result in more severe ischaemia and necrosis, clinically manifesting as STEMI.

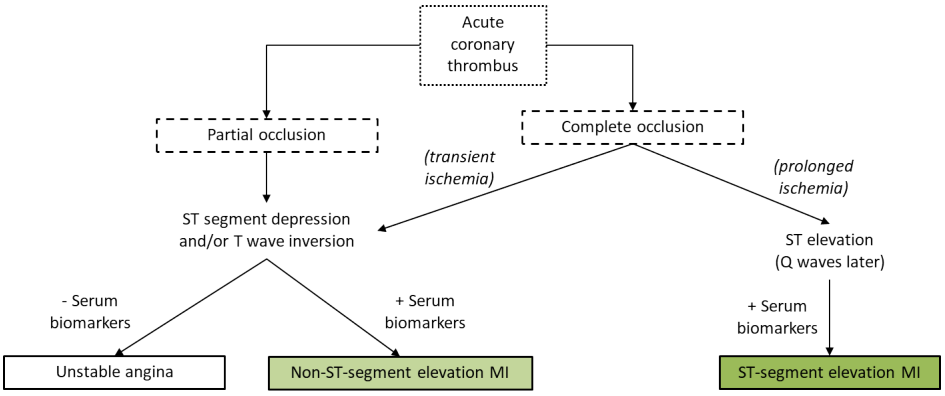

Figure 1.2: Partially and completely occlusive thrombus and consequences (adapted from [22]).

In a post-mortem context, the detection and degree of the occlusion, as well as the subsequent pathophysiological processes (e.g. myocardial ischaemia) directly following the obstruction or reduction of blood flow in a coronary artery are deciding factors in determining the role a partial or complete coronary occlusion played in the death of a person.

Acute myocardial infarction

The clinical criteria for acute myocardial infarction published by the Task Force for the Redefinition of Myocardial Infarction indicate that "the term acute MI should be used when there is evidence of myocardial necrosis in a clinical setting consistent with myocardial ischaemia" [23]. It is characterised by a number of different clinical, electrocardiographic, biochemical, imaging and pathological parameters [23]. In a post-mortem context, the related pathological characteristics, determined by macroscopic morphological assessment, histology and imaging of the heart, stand at the forefront of a diagnosis of acute MI.

Pathologically acute MI is characterised by the necrosis of myocardial cells due to prolonged ischaemia. Following the onset of myocardial ischaemia, restricted blood flow leads to the inadequate supply of oxygen to a certain region of the heart [24]. Histological cell death develops over a finite period of time, for example in as little as 20 minutes [23]. Depending on collateral circulation, persistence of the responsible coronary occlusion, myocyte sensitivity to ischaemia and individual oxygen and nutrient demand, the time required for complete necrosis of myocardial cells in the region at risk differs [23]. Generally, complete cell necrosis does not occur prior to at least 2-4 hours, potentially longer [23]. The identification of myocardial necrosis via macroscopic and microscopic post-mortem examinations is therefore only possible, when the survival time (i.e. time between onset and death) is at least several hours [16, 23].

The exact mechanisms related to the initiation and development of myocardial infarction are dependent on the coronary occlusion itself (e.g. rate of progression, duration, continuous/intermittent), the mass of the region normally perfused by the occluded vessel, the oxygen demand of the region, the localisation of the region, the extent and adequacy of collateral vasculature and finally the response of the myocardium to ischaemia [17, 22]. The absence of a relationship between death and infarct size as well as between infarct size and the number of severe stenoses, observed in post-mortem studies, further reflects the important and complex role of coronary collaterals [25].

Regarding the pathophysiological alterations which occur in the presence of MI, this thesis will focus on early changes (survival time: < 24 hours) as these are most relevant in the diagnosis of SCD and additionally represent a significant challenge for current morphological and post-mortem imaging techniques due to the difficulty in detecting and visualising such lesions. Alterations include the histological progression of the infarct and the impact of oxygen deprivation on cardiac function (i.e. myocardial contractility) [22]. The onset of myocardial hypoxia is rapidly followed by a shift from aerobic to anaerobic metabolism and a reduction in intracellular adenosine triphosphate (ATP) as cells attempt to counteract the reduced

oxygen supply in the region [22]. The rapid shift to anaerobic metabolism causes intracelluar acidosis (i.e. increased intracelluar H^+) ultimately contributing to cell death. Additonally, ATP reduction interferes with the maintenance of the Na^+ and K^+ gradients across the cell membrane due to impairment of the sodium-potassium pump (Na^+ K^+-ATPase), which consequently leads to an increase in extracellular K^+ and intracellular Na^+ [22]. The metabolic alterations which follow this imbalance include intracellular oedema, due to increased intracellular Na^+ and accumulated Ca^{++}, cell death and changes in the membrane potentially caused by membrane leakage and higher extracellular K^+ concentration, making the myocardium predisposed to arrhythmias [22].

These metabolic changes are summarised in Figure 1.3 and can commence only minutes after coronary artery occlusion. In the absence of intervention, such metabolic alterations can quickly lead to irreversible cell death (at least 20-24 minutes) [22].

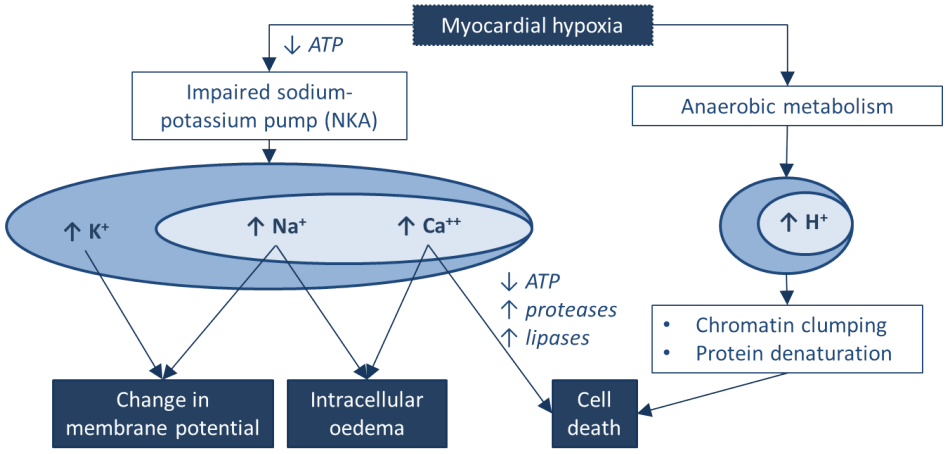

Figure 1.3: Cellular changes due to myocardial hypoxia (adapted from [22])

A summary of the pathological processes and corresponding microscopic findings which are observable post-mortem can be found in Table 1.1. The earliest histological findings of irreversible injury include the appearance of wavy myofibers, due to intracellular oedema, followed by the appearance of contraction bands at the periphery of the infarct area [22]. If the survival time exceeds four hours, acute inflammatory responses (e.g. infiltration of neutrophils) may have commenced and can lead to additional tissue damage [22], which may be visible during post-mortem examinations. For longer survival times, evidence of increasing degrees of necrosis and leukocyte reactions are expected [22, 26].

Table 1.1: Chronology of metabolic and pathological changes [22] as well as the corresponding histological and immunohistochemical findings in MI [26]. Time is given in m (minutes) or h (hours) after onset.

Time	Metabolic & pathological findings [22]	Time	Histological and IHC findings [26]
1-2 m	Decrease in ATP, contraction ceases.		
$\sim$ 10 m	50% of ATP depleted, cellular oedema, membrane potential decreases, increased predisposition to arrhythmia.	$>$15 m	Changes in distances between horizontal stripes in myocardial fibers.
20-24 m	Irreversible cell injury.	$\leq$30 m	Swelling & dissolution of christae mitochondriales.
		30-60 m	Oedema (myocardial fibers), decrease in glycogen, loss of myoglobin & detection of fibrinogen, contraction bands.
1-3 h	Wavy myofibers.	1-3 h	Initial homogeneous hyalinization (myocardial fibers) in periphery of MI
4-12 h	Haemorrhage, oedema, infilitration of polymorphonuclear leukocytes (inflammartory response).	3-4 h	Agglutinated sarcolemma tubesfatty degeneration of myocardial fibers, haemorrhage (demarcation) of MI with hyperemic edges, shrinkage of myocyte nuclei.
		4-5 h	IHC indications of early necrosis (fibronectin, C5b-9(m), fibrogen, loss of demin & myoglobin.
		4-7 h	Necrosis (infarct area), leukocyte reaction (periphery), eosinophilia of myocardial fibers, tamping of heart muscle cells (infarct area), nuclear dyeability.
		$\sim$9 h	Pronouced necrosis (infarct area), strong leukocyte reaction (infarct area), nuclear dyeability (cardiomyocytes) no longer possible.
18-24 h	Coagulation necrosis, oedema.	18-24 h	Pronounced necrosis, leukocyte penetration (infarct area).

Chronic cardiac pathologies

In the aforementioned work by Michaud et al. [18], cause of death was attributed to chronic coronary pathologies in approximately one third of cases (n=28) of SCD. Signs of ischaemic scarring and the presence of significant coronary luminal stenosis ($>$ 75%) due to

atherosclerotic plaque are findings considered highly probable in cases of sudden cardiac death due to CAD [13]. These findings and their relevance in the diagnosis of SCD are introduced below.

1. **Atherosclerotic plaque with coronary luminal stenosis**: According to Guidelines issued by the Association for European Cardiovascular Pathology (AECVP), the observation of a stable atherosclerotic plaque with luminal stenosis of $> 75\%$ with or without healed myocardial infarction leads to the highly probable diagnosis of SCD, if no other cause of death is observed during autopsy and additional examinations [13, 18]. Therefore, accurate assessment of atherosclerotic plaque composition and the degree of luminal stenosis are important for the determination of SCD.
2. **Chronic ischaemic heart disease**: Generally manifesting as (disseminated) myocardial scarring, chronic IHD is a common finding in cases of sudden cardiac death [13]. However, although old MI have been observed in 40-80% of cases, death was often attributed to an acute coronary occlusion [27]. Nevertheless, the detection of chronic IHD can provide information important in the global assessment of cause of death.

1.2.3 Post-mortem examination: Sudden cardiac death

During a conventional autopsy the forensic pathologist performs both a detailed external examination of the cadaver as well as a dissection to examine the internal organs [28]. Recently, updated *Guidelines for autopsy investigation of sudden cardiac death* were published by the AECVP [13].

Autopsy and conventional histology

Autopsy practice and the associated dissection techniques are country specific. The description provided in this section is designed to give an overview of common practices, as presented in [13].

In cases of sudden death, a sequential approach to exclude non-cardiac causes of natural sudden death is initially taken. This is then followed by a gross examination of the heart, including photographic documentation [13]. Particular attention is given to the macroscopic assessment of the state of coronary arteries including size, shape, position, number and patency of coronary ostia, dominance of the major epicardial arteries as well as the presence of coronary artery disease (plaque, ruptured plaque, blood clots, occlusions/partial occlusions) through multiple transverse cuts at small (approximately 3 mm) intervals along the arteries [13]. Assessment of the myocardium and endocardium is completed by macroscopically

examining multiple parallel transverse slices of the heart and performing triphenyltetrazolium staining to obtain a preliminary diagnosis of acute MI [13].

At many institutes conventional histological staining methods are routinely applied and these can validate macroscopic findings as well as assist in detecting additional microscopic alterations. Standard histological examination of the heart commences with systematic, labelled sampling of a representative transverse slice of both ventricles, examples of the most severe coronary artery lesions as well as all other relevant cardiac samples [13]. Haemotoxylin and Eosin (H & E) and connective tissue staining of the myocardium and coronary arteries are standard [13]. Certain processes related to myocardial ischaemia and infarction which commence approximately 6-8 hours after onset of ischaemia are detectable if the deceased person has survived the incident for at least this amount of time. Additional, non-specific histological findings can also be observed [29], however the detection of early acute MI based only on forensic autopsy and conventional histology frequently fails [30].

Immunohistochemistry

In cases of early acute MI, improved diagnosis can be achieved using immunohistochemical (IHC) methods. Primary antibodies have been proven effective for demonstrating repair proteins (e.g. fibronectin, C5b-$9_{(m)}$ and fibrinogen) as well as for determining loss of structual proteins (e.g. myoglobin) [26]. For example, increased fibronectin expression has been detected following coronary ligation ($\geq$ 4 h) in a rat model [31]. The C5b-$9_{(m)}$ complex is particularly well-documented in the literature and is considered a reliable marker for early myocardial infarction [29] both in the absence of histological signs of ischemia and for short survival times $\geq$ 30-120 minutes [32–35]. Examination of emerging markers found that non-phosphorylated connexin43 (np-Cx43) was detectable in the cytoplasm of cardiac tissue, even in the absence of apparent myocardial necrosis [36]. Sabatasso et al. recently presented findings of early expression of np-Cx43 ($\leq$ 30 min), fibronectin($\leq$ 1 h) and C5b-9($\leq$ 2 h) in a porcine model [34], before going on to use fibronectin and C5b-9 as a validation technique to determine that np-Cx43 is an early, sensitive marker for MI in humans and that the tissular distribution correlates with specificity of the technique [35]. Nevertheless, IHC diagnosis of early acute myocardial infarction remains complex and challenging [37].

Despite these well-documented advances, IHC techniques are not yet routinely used in forensic diagnostics [26] and these techniques did not receive mention in the recently published AECVP-Guidelines [13]. This may be due to a number of factors including time constraints, requirement for detailed tissue sampling in the absence of macroscopic findings and the associated costs of IHC analyses. Factors such as the primary focus of the forensic examination (i.e. exclusion of third-party involvement), the specific field of application of

individual IHC techniques and the frequent requirement to apply multiple techniques to achieve specific detection of peracute myocardial infarction, may have influenced the slow uptake of these methods in forensic applications.

Post-mortem imaging

Although the AECVP task force does not currently recommend the routine use of post-mortem imaging, the added value of imaging techniques has been recognised for specific applications and suspected causes of death. In a survey performed by the International Society of Forensic Radiology and Imaging, the imaging modality with which participants were most familar was PMCT (55%), followed by radiographs (30%) and PMMR (5%), with the remainder of participants selecting other modalities [38].

1.3 Post-mortem imaging

Since the conception of the *Virtopsy* research program [39], the application of diagnostic imaging techniques in routine forensic practice has seen dramatic developments. A comparison between forensic radiology and other medical specialities demonstrated the exponential increase in scientific publications related to forensic radiology compared with general radiology and forensic pathology in the past years [40]. Post-mortem imaging techniques are fundamentally based on clinical diagnostic imaging techniques which are adapted to account for, and in certain cases, exploit, differences between cadavers and living patients. Significant differences include, lack of blood flow, temperature, anatomical positioning of organs as well as findings influenced by general post-mortem phenomena such as decomposition, putrefaction and blood sedimentation. Conventional radiography, CT, MRI and 3D surface scanning are tools most often categorized as forensic imaging techniques [41]. Here, the discussion will be restricted to CT and MRI examinations which take place in a post-mortem context.

The advantages of medical imaging in post-mortem investigations are numerous, however of particular significance are its contributions in the diagnosis of gas accumulations (e.g. putrefaction gases, air embolisms) and foreign bodies (e.g. projectiles and weapon fragments) inside the body, as well as the diagnostics related to broken bones or cardiovascular interventions [42]. The application of one modality over another depends on the case circumstances and suspected cause of death. In cases of sudden death, the identification of an underlying internal cause represents an important field of application for post-mortem

imaging techniques [16], with both autopsy and imaging methods demonstrating advantages and disadvantages in this regard.

In this section, discussion will be restricted to a general description of the most relevant post-mortem imaging techniques, in the context of sudden death and cardiovascular diseases, and the respective challenges and approaches in performing these examinations in a post-mortem context.

1.3.1 Post-mortem computed tomography

The strengths of CT in a post-mortem context lie namely in the evaluation of skeletal findings, visualisation of foreign objects and the gases in the body. According to Recommendations published by the Germany Society of Forensic Medicine, PMCT should as a general rule be applied in all cases of suspected homocide, suspected presence of foreign objects, suspicion of air embolism or child abuse and in cases of sudden infant death [43]. Furthermore, application on a case-by-case basis is recommended following traffic accidents, suspected medical malpractice and in cases involving children, extremely decomposed and unidentified cadavers [43]. The addition of an angiographic adjunct, post-mortem CT angiography (PMCTA) has further enhanced the visualisation and assessment of the vascular system [43].

1.3.2 Post-mortem computed tomography angiography

As observed in clinical radiology, the sensitivity of CT can be increased by injection of a contrast agent to improve the visualisation of organs and the vascular system [42]. The various approaches to performing PMCTA which have been developed in recent years follow clinical experience and also seek to improve the sensitivity of PMCT, specifically focusing on the investigation of the vascular system and related lesions [42], such as the source of haemorrhage [44], quantification of blood loss and the detection of pathological and anatomical abnormalities of the vascular system [45].

Different approaches have been developed to address the various technical challenges, which depend on the application (targeted vs. whole-body), the properties of the injected perfusate and the pump/circulation mechanism. These challenges can be categorised as being associated with the practical performance of PMCTA, the integrity of additional post-mortem analysis of bodily fluids and tissue and the interpretation of the resulting images [42].

Practicalities of PMCTA

Practical problems for the performance of PMCTA include the absence of cardiovascular circulation, emptiness of vessels, permeability of post-mortem vessels and general post-mortem changes due to autolysis [42].

The absence of circulation means there is no natural carrier for distribution of contrast agent throughout the vascular system. This problem has been counteracted through the use of external forces to distribute contrast agent within the vascular system. Current applications include the use of a pump either conceptually based on a heart-lung machine [6, 9], a flow-calibrated roller pump [46], manual injection [1] or the use of an automatic clinical pump injector with [47] or without [2] cardiopulmonary resuscitation to assume the role of circulation in a post-mortem context.

The empty or partially empty vascular system leads to collapsed vessels, further contributing to interpretation problems in native PMCT. Through injection of a significant volume of perfusate mixture containing a solvent and contrast agent, vessels can be refilled, thereby approaching their ante-mortem appearance in images. The volume of perfusate depends on the specific application. Targeted PMCTA techniques focusing on a specific region (e.g. heart) require less perfusate, between 120-150 ml [1–3], compared with whole-body multi-phase approaches which require approximately 3.3-3.7 litres [9, 46], again, depending on the technique used.

The increased permeability or porosity of post-mortem vessels leads to a greater degree of extravasation through the vascular wall [42]. These effects are time-dependent [48] with the chemical nature (i.e hydrophilic, lipophilic, hyogroscopic) and viscosity of the perfusate influencing the rate at which perfusate is extravasated [4, 5, 7, 48–50]. Different approaches have been developed using various perfusates. Targeted PMMRA uses a combination of negative and positive contrast through initial vascular filling with air followed by a diluted, water-soluble contrast agent (e.g. Urografin) [1–3]. Moreover, multiple techniques for whole-body PMCTA have also been developed using either polyethylene glycol (PEG) [4–6] or paraffin oil as solvent, to which either a water-soluable contrast agent (e.g. Optiray 300 [6], Imagopaque 300 [4], Omnipaque 300 [50]) or lipophilic contrast agent (e.g. Lipiodol Ultra Fluide [7] and later Angiofil [9]) is added.

Depending on the nature and viscosity of the perfusate used, additional problems related to autolysis in regions of high enzymatic activity can arise resulting in expedited or more extreme extravasation of the contrast agent into these regions (e.g. due to vulnerability of the pancreatic capillary bed or gastrointestinal tract) [4, 51, 52]. Technique-based artifacts such as filling defects, layering and contrast extravasation which cause specific enhancement

patterns were retrospectively evaluated in 49 cases examined with multi-phase PMCTA using paraffin oil and Angiofil® [52]. In the current thesis, discussion of these artifacts will be limited to those directly related to or influencing visualisation of the heart and its vessels (i.e. aorta, aortic arch, coronary arteries as well as the cardiac atria and ventricles). Filling defects, which presented as inhomogeneous opacification in the absence of layering, were primarily observed in the cardiac cavities [52]. Layering artifacts were observed more frequently in larger vessels (e.g. in the descending aorta in 67.3% cases) and in the cardiac cavities (16.3-55.1% in the left and right atria and ventricles) [52]. The prevalance of contrast layering observed in the coronary arteries (unchanged over all phases) was 6.1% [52]. These potential artifacts can contribute to the interpretation challenges associated with PMCTA images.

Biological sample integrity for additional analysis

Given the legal context in which forensic autopsies are mandated and performed, the consequences of injecting a given liquid into a cadaver prior to the internal examination need to be carefully weighed in terms of the potential effect on subsequent biochemical, toxicological and immunological investigations [42, 53]. An investigation of the influence of targeted PMCTA using air and Urografin on further analyses, found that this technique did not have a diagnostic affect on femoral blood toxicology or biochemical analysis of vitreous humour [53]. Further studies have examined the effects of multiphase whole-body PMCTA on the macroscopic and histological diagnosis coronary thrombosis, finding no influence [54] and on the biochemical analysis performed using vitreous humour [55], finding no diagnostically relevance influences. In contrast, preliminary findings based on urine samples have indicated that the interpretation of toxicology results related to tetrahydrocannabinol and its metabolites may be potentially altered by multiphase PMCTA [56]. In general, asservation of all samples for toxicological and biochemical analysis prior to the performance of PMCTA is recommended [56, 57].

Interpretation of PMCTA images

The main challenges associated with interpreting PMCTA images are related to blood, including post-mortem clotting processes and blood which remains in the vascular system despite vessel filling leading to inhomogenous contrast with or without visible layering. Additionally, the previously mentioned extravasation of contrast agent due to post-mortem changes can lead to unexpected enhancement patterns, which need to be interpreted with caution [42]. The use of standardised methods and the establishment of guidelines is

recommended to prevent incorrect interpretation of post-mortem blood clots as either vascular occlusions or stenosis [42]. The interpretation of filling defects is considered particularly challenging given the similar appearance of post-mortem clots occluding the vascular lumen and actual ante-mortem occlusions such as thrombi in PMCTA [52], with a recent study demonstrating that autopsy is still much better in diagnosing pulmonary thromboembolism than PMCTA [3].

1.3.3 Post-mortem magnetic resonance imaging

Post-mortem MR applications are less widespread compared with routine PMCT [38]. Nevertheless, PMMR can be a powerful diagnostic tool to not only enhance autopsy results, but to also enable the assessment of otherwise undetectable findings [58]. The diagnostic strengths of MRI in a post-mortem context lie mainly in its ability to depict subtle soft tissue alterations and fluid accumulation, for example due to ischaemic injury, brain oedema, subcutaneous haematoma or internal haemorrhage [58]. PMMR is of particular importance for cardiovascular causes of death, specifically those related to sudden cardiac death [59].

The post-mortem state of the cadaver examined in PMMR influences expected findings and has led to certain findings, despite their initial *abnormal* appearance, to be classified as normal findings on PMMR images. Factors which influence PMMR images include the absence of motion arteficts, position-dependent sedimentation (livores), post-mortem clotting, sedimentation of blood components within the vessel, gas formation and putrefaction processes as well as metal artifacts [51, 60, 61]. Additionally, the temperature dependence of MR tissue relaxation and diffusion properties has been investigated in various studies [62–66] indicating that signal, and consequently contrast behaviour are temperature-dependent [61, 67, 68]. Research is currently ongoing to investigate these effects as well as to determine the influence of post-mortem interval (PMI) on tissue properties relevant in MRI [69–73].

A division of PMMR applications according to their nature was originally proposed in [74] where the two existing approaches were described as either *clinical MRI* or *isotropic quantitative PMMR*. This division is important and provides the basis for the terms used in this thesis to differentiate between two specific applications of native PMMR. The term *morphological PMMR* will be used to describe MR images acquired for radiological assessment using sequences adapted from clinical practice. *Quantitative PMMR* refers to data which have been acquired and correspondingly, often on a pixel-wise basis, fitted or reconstructed to generate so-called quantitative parameter maps, where pixel values have a real, numerical meaning. The diagnostic assessment of the post-mortem heart and its immediate vascular system is therefore best discussed according to the specific application

of PMMR employed.

Morphological cardiac PMMR

For post-mortem radiological assessment of images, T2-weighted images are considered an important diagnostic tool for a range of pathologies as they highlight fluid accumulations [58] and coronal whole-body approaches to maximise coverage are recommended in the literature [58]. Most applications of PMMR found in the current literature employ adapted clinical protocols to achieve morphological images which can then be interpreted by (forensic) radiologists. Due to the influences mentioned above, the interpretation of these images can be challenging and requires the ability to differentiate between normal post-mortem observations and pathologies or lesions relevant in the assessment of cause of death [58].

Quantitative cardiac PMMR

While more extensive work has been completed concerning the post-mortem brain [63, 75–81], current applications of *in situ* quantitative PMMR in a forensic context have focussed on the thoracic and upper abdominal region [30, 64, 65, 82–88]. Parameters of tissues in this region which have been investigated include the longitudinal relaxation (T_1), transverse relaxation (T_2), proton density (PD) as well as diffusion-related parameters including fractional anisotrophy (FA) and mean diffusivity (MD). For the quantification of T_1, T_2 and PD, an approach based on so-called *Synthetic MR* [89] has been taken in numerous publications [30, 64, 65, 82–85]. This technique, originally presented in [90] is based on the simultaneous quantification of T_1, T_2 and PD. It additionally generates a map of the amplitude of the local B_1 field from a single acquisition multi-slice, multi-echo, multi-delay acquisition. Briefly the sequence can be described in two parts. In the initial segment, a slice-selective saturation pulse is applied to a particular slice. In the second segment of the sequence, a slice-selective multi-echo spin echo acquisition is performed elsewhere in the imaging volume. This approach incorporates multiple acquisitions with different time delays T_D between application of the saturation pulse and data acquisition, resulting in data for T_1 fitting [90]. The multi-slice approach used enables simultaneous acquisition of data for T_1 and T_2 fits.

Lastly, a study aiming to establish reference values (T_1, T_2, T_2* and apparent diffusion coefficient (ADC)) for post-mortem myocardium in the absence of cardiac causes of death and the correlation of these values with temperature and post-mortem interval was recently published [88]. This is one of the first post-mortem cardiac quantitative MRI studies which

has used a universally available relaxation mapping tool (syngo MapIt, Siemens) for the determination of quantitative MRI values.

1.3.4 Post-mortem magnetic resonance angiography

Experimental investigation of factors significant for the performance of PMMRA, as well as two feasibility studies can be found in the literature. Development of PMCTA has demonstrated the feasibility of various pump/injection mechanisms and perfusates which can be applied in the context of post-mortem angiography. The systematic investigation of PMMRA presented in this thesis incorporates and extends upon a selected number of assumptions made during the development of PMCTA, which, given the significantly different time factor for PMMR compared to its CT counterpart, play an important role.

Experimental approaches

Ex situ animal and human hearts have been examined in MRI using a similar lipophilic contrast agent mixture (paraffin oil and Angiofil®) to that used in the standardised protocol for PMCTA [9, 91]. This work describes important aspects for the examination of *ex situ* hearts in MRI (e.g. choice of container, positioning of the heart, filling of cardiac cavities) and presents adapted various clinical MR sequences suitable for the visualisation of post-mortem coronary arteries. 2D T1-weighted and T2-weighted sequences with and without fat saturation, as well as two 3D sequences (T1-weighted and T2-weighted (fat saturation)) were explored [91]. Image quality was reported to be assessed in future work, which has not yet been published.

In a different approach, we have systematically investigated a broader range of liquids potentially suitable for use as perfusates in PMMRA [92]. Viscosity, known to influence post-mortem extravasation of liquids was characterised for various potential perfusates over a forensically relevant temperature range. Additionally, intrinsic relaxation properties of the perfusates were also determined at four different temperatures to establish the temperature dependence of these potential perfusates [92]. In our more recent work, we evaluated the intravascular retention of three proposed perfusates (Hygroscopic (PEG200), hydrophilic (Gadovist®-doped physiological solution) and lipophilic (paraffin oil) over 12 hours, revealing significant differences in the leakage properties and attainable contrast in MRI [48].

Feasibility studies

To date PMMRA has been assessed in two small cohorts (n=4 [93]; n=7 [94]) with a PEG200 solvent and Optiray300 [93, 94] to investigate the technical feasibility and image quality. Ruder et al. [93] found the technical quality of PMMRA images to be equal to that of PMCTA in the head, heart and chest in 4/4 cases and in 3/4 cases for the abdomen and pelvis. However, they also reported a signficant decrease in the intravascular contrast volume (46%) between PMCTA and PMMRA, performed in that order [93]. This study highlights the potential feasbility of PMMRA and also eludes to the interesting combination of soft tissue contrast with vascular information determined by angiography [93], while at the same time dermonstrating the imporance of intravascular retention in PMMRA. In a recent study, the order of image acquisition was reversed to obtain PMMRA images immediately after perfusate injection without cadaver movement, thereby avoiding bias due to perfusate extravasation over time [94]. To qualitatively assess the visualisation of vessels as a function of contrast filling, a scoring system was defined (Table 1.2) [94].

Table 1.2: Summary of scoring for qualitative image analysis [94].

Score	Description
1	No contrast agent in vessel
2	Vessel not completely filled along course
3	Vessel filled along entire course; partially insufficient vessel distension (smallest contrast vessel diameter $<$ 50% largest diameter)
4	Vessel filled along entire course; good vessel distension (smallest contrast vessel diameter $\geq$ 50% largest diameter)

Scoring was determined to be significantly lower for PMMRA images than for PMCTA images over all vessels [94]. However, analysis of grouped vessels (large ($>$3 mm), small ($\leq$3 mm), vessels of the head and neck and vessels of the thorax (with/without coronary arteries), vessels of the abdomen and pelvis) indicated that statistically significant differences were only observed for small vessels (all regions) and for vessels of the thorax (including coronary arteries) [94], leading to the conclusion that under the study conditions visualisation quality in PMMRA images was comparable to PMCTA for vessels diameters larger than 3 mm and inferior in smaller vessels.

1.4 Post-mortem imaging of cardiac pathologies

Currently, CT, CT angiography and MRI are applied in the post-mortem radiological examination of cardiovascular pathologies [59]. Following the previous description of these approaches and the general challenges associated with each, this section will mainly focus on specific applications in study cohorts to assess cardiovascular causes of death, in particular those related to sudden cardiac death. Early literature in the field of forensic imaging presented many feasibility studies and case reports [41] with preliminary work placing a great deal of value on describing and comparing findings observed in the applied imaging modalities and at autopsy [95]. In line with recent technical, infrastructural and mandating developments, scientific studies with larger cohorts have begun to examine the sensitivity and specificity of individual modalities for the assessment specific causes of death or disease groups. In this context, the most profound source of information relates to cause of death in foetuses and children [96–98].

In the current literature, either discrepancy, sensitivity and/or specificity data could be identified for the assessment of cardiovascular diseases in adults in seven post-mortem imaging studies [3, 86, 99–103]. A systematic review by Eriksson et al. [104] identified 22 studies in the field of post-mortem imaging which presented a moderate risk of bias (no studies were found to display low bias). A moderate level of bias was assigned when minor shortcomings in study design were present (e.g. unclear selection criteria), time between imaging and autopsy > 72 hours (adults), when the pathologist was not blinded. Of those studies, five investigated imaging findings for coronary artery disease and compared these with a reference test, which was defined as a combination of autopsy and histology [104]. This detailed review focused primarily on studies in which a defined index test (imaging modality, diagnosis by radiologist) and reference test (autopsy and/or histology, diagnosis by pathologist) were compared [104]. Other important contributions in the field of post-mortem cardiac MRI, specifically quantitative approaches to cardiac PMMR [30, 64, 65, 84] seem to have been excluded (or not assessed), possibly due to the strict bias criteria applied (i.e. blinding requirements).

Based on published work, the exact role and diagnostic contribution of current post-mortem imaging techniques for the assessment of acute events conventionally associated with the diagnosis of cardiovascular substrates of SCD, such as acute coronary occlusion and acute myocardial infarction, is still being established. No gold standard currently exists for the radiological assessment of such pathologies [59]. A selection of scientific studies which are considered representative of the current state of research in this regard are discussed below and summarised in Table 1.3 and Table 1.4.

Table 1.3: Summary of studies presenting results regarding the evaluation of cardiovascular pathologies using PMCTA.

Technique	Population	Type	Pathology
Whole-body multiphase PMCTA [9]	n=50 [100]	P	Trauma, intoxication, natural death
	n=23 [95]	R	Suspected IHD
	n=80 [105]	R	MI, 2 approaches (n=40, n=40)
	n=10 [106]	R	Suspected IHD
Targeted PMCTA	n=210 [3]	P	Natural & non-suspicious unnatural deaths

P = prospective, R = retrospective

Table 1.4: Summary of post-mortem imaging studies presenting results regarding the evaluation of cardiovascular pathologies using PMMR.

Technique	Field	Population	Type	Parameters	Pathology
Morphological PMMR	3T	n = 136 [107]	P	T1w TSE, T2w TSE*, T2w TSE (FS), near PDw TSE, near PDw TSE (FS), GRE	History of chronic/acute cardiac anamnesis, suspected cardiac death. Cardiac death (n=76), non-cardiac death (n=60).
Quantitative PMMR (SyMRI®)	3T	n=50 [84]	P	T_1, T_2, PD	Known history of MI or symptoms of acute coronary syndrome.
	3T	n=81 [65]	P	T_1, T_2, PD	
	1.5T	n=80 [30]	P	T_1, T_2, PD	
Quantitative PMMR	3T	n=40 [86]	P	FA , MD	History of IHD / at least three positive risk factors for CAD (after exclusion criteria, n=26).

*P = prospective, *Grading predominantly based on T2-weighted images*

1.4.1 Cardiac causes of death: PMCTA

Using a consecutive sampling method without specific exclusion criteria, Chevallier et al. [100] found that across all tissue and lesion types, autopsy (macroscopic examinations) and MPMCTA reported 77.2% and 93.3% of essential findings respectively [100]. Essential findings referred to those which were essential in determining cause of death [100]. If discussion is restricted to findings in the vascular system, these statistics become 83.8% and 97.1% respectively. This notably highlights the usefulness of MPMCTA in the detection of post-mortem vascular lesions. Nevertheless, it was noted in this study that currently definitive determination of the vitality of vascular occlusions (i.e. to differentiate between post-mortem clots and thrombi/emboli which formed ante-mortem) was only possible via

conventional autopsy [100]. Four other retrospective studies applying the same PMCTA method [9] have additionally demonstrated the potential of the technique. Michaud et al. [95] determined from 23 cases that PMCT, despite its ability to localise calcifications, only had limited diagnostic value for IHD, while PMCTA delivered good visualisation of the coronary arteries, enabling exclusion of significant coronary stenoses and localisation of occlusions for direct sampling and histological analysis [95]. PMCTA enabled assessment of the degree of stenosis and indicated a potential correlation between infarcted myocardium and enhancement on PMCTA images [59]. Two studies [105, 106] have recently followed up on this aspect. Vanhaebost et al. reported PMCTA enhancement patterns in the presence of both increased levels of cardiac troponins and morphological findings of ischemia (n=80) [105]. Additionally, investigations in a study population, where cause of death was attributed to MI or cardiovascular pathology (n=10) and control population (n=10) also confirmed the presence of myocardial enhancement in cardiac death cases and absence of enhancement in control cases [106].

Using a targeted approach, Rutty et al. recently published results from a prospective, controlled study which included natural and non-suspicious unnatural deaths (n=210) indicating the gold standard for post-mortem investigations should, under the local juridical conditions (England), include PMCTA and autopsy [3]. This study provides an evaluation of independent PMCTA and autopsy error through the definition of a combined gold standard (PMCTA & autopsy). Major discrepancies between PMCTA and the aforementioned gold standard were observed in 6% of cases, for autopsy this number was 5% [3], however this difference was not found to be statistically significant. Results indicated that PMCTA was significanty more accurate (less discrepancies) in the identification of trauma and haemorrhage ($p = 0.008$), while autopsy was more accurate in the detection of pulmonary thromboembolism ($p = 0.004$) [3]. Contrary to other work [105, 106] a case of myocardial infarction with a perfusion deficit, instead of enhancement, was presented. Unfortunately no further details regarding the prevalence of this finding were given in the publication.

1.4.2 Cardiac causes of death: PMMR

The detection of myocardial infarctions and the differentiation between early acute and older infarctions, represent important findings in post-mortem investigations and are developing applications for PMMR. Representative observations for the various stages of myocardial infarction (i.e. peracute, acute, subacute and chronic) were initially presented in a small cohort (n=8) by Jackowski et al. [5]. Thereafter, a larger study (cardiac death, n=76) demonstrated a correspondence between the histological staging of MI and certain MRI contrast behaviour in the marginal and necrotic regions of infarctions based on T1-weighted,

T2-weighted and PD-weighted images [107]. In their work, Jackowski et al. presented a time course of MR signal alterations due to myocardial lesions [107]. Interestingly, the peracute (early acute) phase (0 - $\sim$6 hours) tissue at the centre of the lesion tended to present as hypointense on T2-weighted and to a lesser degree on PD-weighted images [107]. Signal intensity alterations in the marginal regions were not observed for lesions categorised as peracute in this work [107].

The post-mortem application of quantitative MRI has enabled the additional characterisation of myocardial lesions as presented in studies at both 1.5T [30] and 3T [65, 84]. Two studies [30, 65] temperature-corrected the T_1, T_2 and PD values to 37°C facilitating comparison across cases and studies. Results from these studies are summarised in Table 1.5 and indicate that an increase in both T_1 and T_2 values can be observed between non-pathologic myocardium and lesions categorised as corresponding to early acute myocardial infarction [30, 65]. Differences in relaxation times between the two studies for the same tissue may be explained by field strength differences, where values obtained at 1.5T are expected to be lower than at 3T [108]. All three studies performed using quantitative PMMR demonstrate the potential for multi-parameteric characterisation of tissue [30, 65, 84].

Table 1.5: Definition of myocardial lesions [5, 107] and temperature corrected values (integers) obtained at 1.5T [30] and 3T [65]. n refers to the number of lesions except for non-pathological findings where n defines the number of control hearts. Times are given in h (hours) and d (days) after presumed onset.

	Histological findings	Time frame	T_1 in ms (mean±SD)		T_2 in ms (mean±SD)	
			1.5T	3T	1.5T	3T
Non-pathological			521±4 (n=10)	1194±60 (n=10)	75±2 (n=10)	54±6 (n=10)
Early acute	Wavy fibers, hypereosinophilia, loss of cross striation (myocardial fibers).	6-24 h	564±22 (n=39)	1280±72 (n=16)	85±6 (n=39)	72±7 (n=16)
Acute I	Early coagulation necrosis, no granulocyte infiltration, no haemorrhage.	1-7 d	388±9 (n=8)	1012±87 (n=10)	48±2 (n=8)	39±8 (n=10)
Acute II	Coagulation necrosis, nuclear pyknosis, karyolysis, granulocyte infiltration, myocardial edema, hemorrhage.	1-7 d	567±5 (n=6)	1440±45 (n=9)	128±4 (n=6)	81±7 (n=9)
Sub-acute	Fibroblasts (loose connective tissue), angiogenesis.	7-28 d	480±15 (n=10)	N/A (n=3)	83±5 (n=10)	N/A (n=3)
Chronic	Nuclei free, blood vessel free collagenous fibers.	>28 d	405±29 (n=10)	907±75 (n=11)	67±8 (n=10)	38±9 (n=11)

1.5 Clinical MRI of the cardiovascular system and cardiac diseases

In this section a selection of relevant techniques for the clinical performance of MR angiography are presented and discussed in terms of the mechanisms of contrast generation and relevance in post-mortem applications. Additionally, current trends in quantitative cardiac imaging relevant to the clinical assessment of myocardial infarction are briefly described.

1.5.1 Clinical MR angiography

According to the contrast generated, the pulse sequences used for clinical MR angiography can be categorised as either dark or bright blood angiography.

Dark blood angiography

Dark blood angiography attenuates signal originating from blood, and is especially useful in the evaluation of vessel walls and can additionally reduce artifacts related to pulsatile flow [109]. These techniques primarily exploit signal loss due to the outflow of blood using conventional spin echo sequences or the longitudinal relaxation of blood itself through the application of single of double inversion recovery pulses [109]. In this thesis, techniques related to dark blood angiography were not considered appropriate due to two principle reasons. Firstly, the outflow of blood cannot be reliably exploited for signal generation due to the lack of circulation in the cadaver. Secondly, air is omnipresent in cadavers, including within the vascular system. The differentiation between between air and vascular occlusions is essential in the post-mortem evaluation of vessels and would not be optimised by the application of dark blood angiography techniques. Therefore, discussion of clinical MR angiography sequences will be mainly limited to bright blood techniques.

Bright blood angiography

Bright blood MR angiography, in which vascular signal is enhanced, can be further categorised depending on the mechanism of contrast generation. Clinically, flow effects (e.g. Time of Flight (TOF), phase contrast or arterial spin labelling), contrast agents (e.g. gadolinium-based chelates) and the relaxation properties of blood are typically exploited [109, 110].

TOF relies on the contrast generated through the inflow of fresh, unsaturated blood, which is enhanced due to the saturation of the stationary components in an imaging section (slice or slab). This inflow enhancement technique is velocity-dependent, with slow movement blood generating less contrast compared with faster flowing blood [110]. Although primarily applied to image and quantify flow in blood vessels, phase contrast can also be expoited for specific MR angiography applications [109]. As with the previously described TOF, phase contrast is also dependent on the flow of blood and to which flow-encoding bipolar gradients are applied. Dephasing the spins of moving blood introduces flow sensitivity along the gradient axis, thereby encoding flow information in the acquired phase images [109]. As mentioned in the discussion of dark blood techniques, the absence of flow blood in post-mortem imaging is a significant consideration in the determination of an appropriate image acquisition strategy for post-mortem MR angiography. Therefore, the work presented in this thesis will focus on the remaining two techniques for vascular contrast generation, namely the use of contrast agents and relaxation-based imaging techniques.

Contrast-enhanced MR angiography is based on the T_1 shortening effect experienced by protons in blood following injection of a contrast agent such as a paramagnetic substance

(e.g. gadolinium(Gd)-chelate, iron oxides). T_1 shortening causes signal enhancement on T1-weighted images thereby enabling improved differentiation between vessels and surrounding tissue [109]. In a clinical setting and for contrast agents which do not remain intravascular (E.g. Gd-chelates) image acquisition is required to be completed on the first pass of the bolus, necessitating precise timing and fast image acquisition. Alternatively, the fundamental differences in the relaxation behaviour of blood and surrounding tissue can be used as a contrast mechanism for vascular enhancement. Generally, the longitudinal relaxation of blood is slower than that of surrounding tissue. Furthermore, differences in T_2 and T_2* exist between venous and arterial blood, where reduced haemoglobin oxygenation levels in venous blood increase the rate of signal decay. Therefore, the selective flow-independent depiction of arterial signal through suppression of signal originating from veins and stationary tissue is possible [110].

In the context of post-mortem MR angiography, the approach investigated in this thesis adopts features of both relaxation-based and contrast-enhanced MR angiography. Under the premise of post-mortem filling of the vascular system and the absence of motion, PMMRA can be optimised to exploit the intrinsic properties of the liquid used for filling and post-mortem conditions. To avoid confusion with classical, *in vivo* MR contrast agent terminology, the term perfusate is used in this work to describe the liquid employed for post-mortem vascular filling. As such, the term perfusate is independent of the presence or absence of a MR contrast agent.

1.5.2 Quantitative cardiac MRI

Clinical cardiac research has demonstrated an increasing interest in quantification of both relaxation and diffusion properties in myocardium [10].

Relaxometry

MRI parameter mapping of relaxation times enables simultaneous visualisation and quantification of pathological processes including *intracellular* disturbances of cardiomyocytes, *extracellular* changes in the myocardial interstitium as well as a combination of both, as seen in myocardial edema and/or infarction [10]. Furthermore, quantitative mapping can minimise subjectivity and offer major advantages in terms of reproducibility [111, 112]. Parameteric mapping of T_1 relaxation is frequently applied in the context of pre and post-contrast enhancement examinations and can be used to estimate the myocardial extracellular volume, related to the diagnosis of fibrosis [10]. Compared with conventional T2w imaging, native

T_1 mapping has demonstrated superior detection of myocardial damage in patients with non STEMI and equal performance in patients with STEMI [113] as well as the ability to identify infarct core regions [114]. T_2 mapping has also demonstrated its relevance in native cardiac magnetic resonance [10, 115], particularly for quantification of myocardial edema where changes in the tissue water content influence the transverse relaxation of myocardial tissue [116–118]. T_2* mapping has been found to correspond to a diagnosis of iron overload and making it relevant in the assessment of myocardial overload [115]. In clinical cardiac practice, rapid acquisition strategies including modified Look-Locker, modified Look-Locker inversion recovery (MOLLI) and saturation recovery single shot acquisition (SASHA) are often applied for myocardial tissue characterisation to address one of the major challenges in quantitative parameter mapping of the heart - cardiac motion [10, 118]. These techniques have improved the clinical feasibility of quantitative myocardial mapping and have led to their increasing application to quantify pathological changes in myocardial composition [10].

Diffusion tensor imaging

Further to relaxometry-based techniques, additional parameters can be quantified to provide supplementary information regarding tissue integrity and micro-structure. While clinical *in vivo* diffusion tensory imaging (DTI) is technically challenging due to cardiac motion and signal-to-noise ratio (SNR) limitations [119], *ex vivo* studies, where motion is no longer an issue, have already demonstrated the potential of DTI in characterising the structure, organisation and integrity of the myocardium [120]. Using various techniques to quantify diffusion properties, such studies have demonstrated alterations in fiber structure, depictable for example through measurements of fractional anisotropy (FA) or molecular diffusion rate (mean diffusivity (MD) or ADC) [86, 121], as well as the presence of a complex network of residual myofibers in infarcted myocardium [122]. While most studies were conducted using animal models and following tissue fixation, exceptions are to be found in the field of forensic imaging, where cardiac DTI was performed *in situ* prior to autopsy. The feasibility of DTI to detect MI (n=2) was investigated through the application of a novel diffusion weighted double-echo steady state sequence and generation of MD maps, which were histologically validated to reveal acute myocardial infarction [87]. The second study (n=26), which compared healthy and infarcted myocardium, indicated that FA and MD were associated with good sensitivity [86] for the detection of MI. However, results also demonstrated these measures exhibited poor specificity, highlighting the importance of including temperature and post-mortem interval (PMI) into the statistical models [86].

1.6 Objectives, approach and expected outcomes

As previously described, current research regarding the radiological assessment of cardiac causes of death primarily focusses on visualising vessels and calcifications using post-mortem CT angiography and on the quantification of tissue alterations in post-mortem myocardium using accelerated quantitative PMMR. Building on this research and expanding in a new direction, this thesis presents an investigation of the premises and considerations for performance of post-mortem MR angiography as well as the determination of the feasibility of PMMRA in a small forensic cohort. To address the research questions described in Section 1.1 a systematic and sequential methodology was applied. This section details the specific objectives for each phase of the investigation process, the general approach taken to achieve these objectives, the specific research questions addressed and the expected outcomes of the work undertaken.

Regarding the general structure of this work, the methodology and results from each phase are individually described before progressing to a combined interpretation and discussion of the outcome. Thereafter, a brief summary and glimpse into future work is provided to conclude this thesis.

1.6.1 In vitro characterisation of potential perfusates for PMMRA

The objective of this initial phase, was to evaluate various solutions and pure liquids to determine their suitability for use as perfusates in PMMRA. To achieve this objective, a preliminary selection of perfusates was performed, the main factors affecting suitability were defined (e.g. chemical nature, viscosity, MR relaxation behaviour) and these properties were characterised across a forensically relevant temperature. The specific research questions addressed were:

- ⇒ What are the physical and relaxation properties of perfusates potentially suitable for visualisation of post-mortem coronary arteries in MRI?
- ⇒ What is the temperature dependence of these properties?

The expected outcome following completion of this phase, was a reduced number of perfusates for potential application in PMMRA.

1.6.2 Visualisation of vessel-like structures in an *ex vivo* porcine tissue phantom

MRI contrast is determined by the intrinsic properties and applied imaging parameters. Following characterisation of potential perfusates, this phase aimed to determine optimal sequences and scan parameters for the visualisation of vessels filled with a given perfusate. To achieve this, images from clinically available sequences were evaluated using a porcine tissue phantom to represent post-mortem tissue and vessel-like structures. The specific research question addressed was:

⇒ Which MR sequences deliver sufficient resolution and contrast between filled vessels and post-mortem tissue?

The expected outcome of this phase was an MRI protocol which provided reliable vessel visualisation using clinically available sequences.

1.6.3 Extravasation of perfusates in *ex situ* porcine hearts

This phase aimed to determine the intravascular retention of three perfusates deemed suitable for PMMRA following in vitro investigations. MRI examinations were performed in non-pathological *ex situ* porcine hearts within a short PMI to determine the rate of extravasation out of porcine coronary arteries into surrounding tissue as well as to investigate the specificity of extravasation patterns in myocardium. The relevant research question addressed in this section was:

⇒ How do perfusate characteristics influence intravascular retention in post-mortem coronary arteries?

An improved understanding of the behaviour of selected perfusates in post-mortem vessels and the selection of an optimal perfusate for application in PMMRA were the expected outcomes of this phase.

1.6.4 Detection of MI in *ex situ* porcine hearts using MRI at 3T

Contrary to the earlier stages in this work, which have focused primarily on visualising vascular structure and associated pathologies, this phase aimed to investigate a broader range of MR contrast mechanisms, specifically quantitative parametric mapping including relaxometry and diffusion. The specific objective was to evaluate MRI sequences regarding

the detection of induced MI in porcine hearts and the corresponding research questions were as follows:

- ⇒ Can post-mortem myocardium be characterised using quantitative post-mortem MR imaging techniques?
- ⇒ Do quantitative parameters values differ in infarcted (ischaemic) and non-pathological post-mortem myocardium?

The expected outcome was an improved understanding of the relaxation and diffusion properties of pathological and non-pathological post-mortem myocardium.

1.6.5 Post-mortem MR angiography: Feasibility and imaging approaches in a forensic cohort

The objective of the final phase of this thesis was to apply the developed approach and propose a final imaging strategy for PMMRA in a forensic cohort. Selected clinically available sequences were adapted from the previous phases of this thesis and implemented to image forensic cadavers at 1.5T. A feasibility study was conducted using this final MR protocol. The following research questions were addressed in this final stage:

- ⇒ Is the performance of PMMRA following MPMCTA feasible in routine forensic practice?
- ⇒ Which MR sequences are optimal for the visualisation of post-mortem reperfused cardiac vessels?

The expected outcome of this phase was an initial assessment of the feasibility and potential of the implemented approach to PMMRA.

2 Applied MRI data acquisition and image processing techniques

This chapter presents the image acquisition, processing and analysis techniques applied during the experiments and examinations undertaken in this thesis. These methods are directly related to the evaluation and development of PMMRA as well as relevant for quantitative post-mortem MRI applications to improve the post-mortem evaluation of sudden cardiac death. In Section 2.1, general information related to MRI data acquisition is summarised. Thereafter, the methodology for image evaluation and processing is described in Sections 2.2 and 2.3. Finally, the relevant image and statistical analysis procedures are briefly discussed. For clarity, the aspects relating to morphological MR images and quantitative MRI data (quantitative parameter mapping) are discussed separately in each section.

2.1 Image acquisition

In vitro and animal experiments were conducted on a clinical 3T scanner (Skyra, Siemens Healthcare GmbH, Germany). All *in vitro* measurements and *ex vivo* examinations on porcine hearts were performed using the built-in birdcage Rx/Tx (transmit) and the 20-channel head/neck coil (receive). Porcine tissue phantom examinations were performed with a 15-channel Rx/Tx knee coil (Siemens Healthcare GmbH, Germany). All MRI examinations of forensic cadavers were conducted on a 1.5T scanner (Ingenia (Achieva dStream), Philips, Netherlands) with two FlexCoverage coils (anterior) as well as posterior FlexCoverage (total: 64 channels) at the University Center of Legal Medicine (Lausanne-Geneva) (CURML) in Switzerland. All cadavers included in this study were forensic cases in which an autopsy, including post-mortem imaging, was commissioned by the local prosecuting authority. To achieve the high-resolution images necessary for visualisation of the coronary arteries in PMMRA, clinical MRI sequences were investigated and adapted. MR data for quantitative parameter mapping of post-mortem myocardium were acquired using standard, universally available sequences. A general description of image acquisition strategies for both morphological images and quantitative MR data is given below, with detailed parameters included in the image acquisition section of each of the upcoming chapters.

2.1.1 Data format

DICOM images were exported from the scanner, for inversion recovery sequences DICOM images contained the real part of the image. All other images were saved as magnitude images. DICOM Images were converted to NIfTI images to facilitate image processing. Conversion was performed using dcm2nii (integrated in the MRIcron [123]) which additionally corrected for image scaling (slope, intercept) as recorded in the metadata. All image evaluation, processing and analysis was performed using these NIfTI images unless otherwise stated.

2.1.2 Morphological MRI images

The investigation and adaptation of clinically available sequences for morphological assessment of vasculature is the focus of the work presented in Chapter 4. In this phase, clinical sequences were adapted and form the basis for acquisition of morphological images in the subsequent phases of this work (i.e. in experiments investigating the extravasation of perfusates in *ex situ* porcine hearts (Chapter 5) and investigation of PMMRA feasibility and imaging approaches at 1.5T (Chapter 7)). Specific acquisition parameters for these examinations are found in the image acquisition section of each of the corresponding chapters.

2.1.3 Quantitative parameter maps

2D turbo inversion recovery (TIR) and 2D multi-echo spin echo (MSE) data were acquired for T_1 and T_2 mapping. *Ex situ* examinations of porcine hearts also included diffusion weighted imaging using two sequences to compare and evaluate these sequences for future work. Quantitative parameter mapping was performed in the *in vitro* characterisation of potential perfusates (Chapter 3), investigation of the extravasation of perfusates in *ex situ* porcine hearts (Chapter 5) and the detection of myocardial infarction in *ex situ* porcine hearts at 3T (Chapter 6). The acquisition parameters applied for these examinations are found in the image acquisition section of each of the corresponding chapters.

2.2 Evaluation of image quality

The quality of morphological images and MR data used to generate quantitative parameter maps was evaluated during various phases of this work. The methods used to objectively assess image quality, are presented here.

2.2.1 Morphological MRI images

The ultimate purpose of morphological MR images is to provide a sound basis for radiological evaluation. For method development purposes and prior to radiological evaluation of images, an initial assessment of the technical image quality was completed using the implemented methods described in this section. Details regarding the specific application of the metrics described in this section are provided in the relevant chapters.

Signal-to-noise and contrast-to-noise ratios

Signal-to-noise ratio (SNR) is a quantitative measure which can be employed to describe and evaluate image quality as well as to compare MR images [124]. Estimation of SNR in this thesis used the frequently employed "two region" approach, where SNR is calculated based on the mean signal intensity in a region of interest (S_1) and the standard deviation of noise (σ_{noise}) in image background (Eq. 2.1,[124]). This approach requires fulfilment of two assumptions: a uniform distribution of noise over the entire image and knowledge of the statistical distribution of the noise [124]. The use of phased-array coils and accelerated imaging reconstruction methods interferes with both of these assumptions as detailed in [124].

$$\text{SNR} = \frac{S_1}{\sigma_{noise}}. \tag{2.1}$$

In the current thesis, SNR measurements were used for one of three purposes: evaluation of image quality prior to quantitative parameter mapping, comparison of MR imaging sequences using a single perfusate and comparison of perfusates under consistent MR imaging conditions and parameters. Additional details of the actual noise distribution for each of these purposes is provided in the corresponding chapters. Statistical distribution of noise differed depending on the application of parallel imaging techniques (e.g. GRAPPA), the receiver coil used for data acquisition and whether real or magnitude images were reconstructed. The factors discussed above directly contribute to the complexities associated with the correct and accurate estimation of noise and therefore SNR in MRI images. In the presence of phased-array coils and parallel imaging reconstructions, if the statistical distribution of noise can be determined, the original σ_{noise} can be calculated by the various equations described in [125]. However, these equations are valid only for circumstances in which the noise in the background image, or defined region thereof, is representative of the entire image.

Since detailed investigation of the satisfaction of these preconditions exceeded the scope of this work, the solution (Eq. 2.3) proposed by Dietrich et al. [125], where completely uncorrelated receiver channel noise is not assumed, was adopted for SNR calculations. In this approach, the second moment of voxel intensities in the defined background region, where N is the number of voxels in the region, is calculated [125]. The second moment $E(x^2)$ is not affected by noise correlation and can therefore be taken in combination with knowledge of the number of channels in the receiver coil n to estimate σ_{noise} according to Eq. 2.3 [125].

$$E(x^2) = \frac{\sum_{k=1...N} x_k^2}{N} = 2n\sigma_{noise}^2, \tag{2.2}$$

$$\sigma_{noise} = \sqrt{\frac{E(x^2)}{2n}}. \tag{2.3}$$

The contrast-to-noise ratio (CNR) was further calculated to assess contrast between two defined regions according to Eq. 2.4.

$$\mathrm{CNR} = \frac{S_1 - S_2}{\sigma_{noise}}. \tag{2.4}$$

CNR efficiency ($\mathrm{CNR_{eff}}$), considered to provide a fairer comparison across imaging sequences with differing acquisition times (TA) [126, 127] was also assessed according to Eq. 2.5 [126].

$$\mathrm{CNR_{eff}} = \frac{\mathrm{CNR}}{\sqrt{\mathrm{TA}}}. \tag{2.5}$$

where S_1 is the main region of interest (ROI) (e.g. perfusate or pathological tissue) and S_2 is the secondary ROI (e.g. surrounding tissue). Calculation of SNR, CNR and $\mathrm{CNR_{eff}}$ were performed in Matlab R2016 and Python [128].

Blur metric

To provide a quantitative measure of the perceived blur in morphological images, a *perceptual blur metric* was used to evaluate the sharpness of MR images and provide additional information regarding image quality. This objective metric was selected as it required no reference and enables robust discrimination between different levels of blur perceived in the same image. The metric was previously validated through subjective tests and psychophysics functions [129]. It is based on the concept that image sharpness influences the variation of gray levels in the neighbouring voxels in an image when blurring (e.g. low pass filter) is applied [129]. Thus, blurring of sharp images leads to larger variation in the grey levels

of neighbouring voxels compared with blurring of an already blurry image. Therefore, the perceptual blur metric analyses the behaviour of neighbouring voxel variation to estimate blur [129]. Blur annoyance in an image is quantified in a process in which the original image $I_{h,v}$ was initially blurred through application of a strong low pass filter in the horizontal and vertical direction $f_{h,v}$.

$$B_{h,v} = I_{h,v} f_{h,v}. \tag{2.6}$$

For both the original $I_{h,v}$ and blurred $B_{h,v}$ images, the absolute difference between neighbouring voxels was calculated in the horizontal ($i = 1...h-1$) (Eq. 2.7) and vertical ($j = 1...v-1$) directions (Eq. 2.8).

$$D(I_h) = |I_{i,j} - I_{i+1,j}|, \quad D(B_h) = |B_{i,j} - B_{i+1,j}|, \tag{2.7}$$

$$D(I_v) = |I_{i,j} - I_{i,j+1}|, \quad D(B_v) = |B_{i,j} - B_{i,j+1}|. \tag{2.8}$$

Thereafter, the difference in variation was determined to give the maximum (positive) variation ($V_{h,v}$) in each direction (Eq. 2.9).

$$V_h = D(I_h) - D(B_h), \qquad V_v = D(I_v) - D(B_v). \tag{2.9}$$

To compare variation in the original images $D(I_{h,v})$ with the variation observed between the original and blurred images $V_{h,v}$, the sums of the coefficients over all voxels in the horizontal and vertical directions were calculated (Eq. 2.10, Eq. 2.11).

$$SoC(I_h) = \sum D(I_h)_{(i,j)}, \quad SoC(I_v) = \sum D(I_v)_{(i,j)}, \tag{2.10}$$

$$SoC(V_h) = \sum V_{h(i,j)}, \quad SoC(V_v) = \sum V_{v(i,j)}. \tag{2.11}$$

The blur metric was computed in the horizontal and vertical directions from the difference between $SoC(I)$ and $SoC(V)$, normalised over the sum of the coefficients in the original images $SoC(I)$ (Eq. 2.12).

$$\text{blur}_{h,v} = \frac{SoC(I_{h,v}) - SoC(V_{h,v})}{SoC(I_{h,v})}. \tag{2.12}$$

The final blur metric (blur) was taken as the maximum blur, independent of direction (Eq. 2.13).

$$\text{blur} = \max(\text{blur}_h, \text{blur}_v) \tag{2.13}$$

This metric gave an estimate of the perceptual blur in a range between 0 and 1, which respectively represented low and high levels of blur in the original image.

2.2.2 Quantitative parameter mapping

Signal-to-noise ratio

The presence of noise in MR images, which are used as a basis for quantitative parameter mapping, can affect the quality and accuracy of the fitting of relaxation and diffusion-related parameters, thereby influencing the final parameter maps [130]. SNR was assessed in quantitative MR imaging data in Chapter 6 as described for the morphological images. Signal masks were defined via automatic masking of the object (e.g. *ex situ* porcine heart) using median filter smoothing based on an automatic histogram thresholding technique (Otsu) [131]. This process was optimised by adjusting the radius and number of passes of the applied median filter [131]. The noise mask was generated by inverting and eroding the signal mask. Signal and noise masks were applied to all data to extract and calculate the values S_1 and σ_{noise} required for calculation for SNR Eq. 2.1.

2.3 Image processing

This section describes the various algorithms implemented following image acquisition, focussing on procedures undertaken prior to image analysis, which are described separately in the next section. Specifically, the processes and algorithms related to image denoising, fitting and registration are described here.

2.3.1 Morphological MR images

Morphological images were primarily acquired for radiological analysis and with the exception of post-processing applied prior to data export from the scanner, these images were not subjected to additional image processing steps.

2.3.2 Quantitative parameter mapping

Image processing of quantitative data included denoising, data extraction (background masking), parameter fitting and registration.

Non-local means denoising

With the objective of improving the robustness and reliability of parameter fitting and diffusion tensor modelling, noise which could influence the precision and accuracy of voxel-wise fitting was removed using a blockwise implementation of a non-local means (NLM) denoising filter [131, 132]. NLM denoising has been recently applied in saturation recovery-based myocardial T_1 mapping [130] as well as in diffusion kurtosis imaging [133] and DTI, where it outperformed other classical denoising methods (e.g. Gaussian smoothing, anisotropic diffusion and total variation) [134].

In the classical voxel-wise NLM approach, an estimated (restored) intensity value is computed for each voxel $NL(u)(x_i)$. The estimated value is based on the intensity of other voxels $u(x_j)$ in the search radius V_i and their attributed weighting $w(x_i, x_j)$ (Eq. 2.14, [135]).

$$NL(u)(x_i) = \sum_{x_j \in V_i} w(x_i, x_j) u(x_j). \tag{2.14}$$

The weighting factor $w(x_i, x_j)$ is determined according to similarities between the local neighbourhood N_j and the neighbourhood N_i surrounding the voxel of interest x_i [135]. Based on their neighbourhood configuration, similar voxels x_j, measured as a decreasing function of the weighted Euclidean distance, have a greater weighting for the restoration of a given x_i than dissimilar voxels (Eq. 2.14). For a full description of the original NLM algorithm, the reader is referred to [135].

Conceptually, the blockwise implementation of NLM divides the image volume into partially overlapping blocks (B_{ik}) instead of voxels. NLM-like restoration is performed on these blocks [131, 132, 136]. The restored value of a given block $NL(u)(B_{ik})$ is a function of other block intensities $u(B_j)$ in the search volume V_{ik} and the block weighting $w(B_i, B_j)$ (Eq. 2.15,[132]).

$$NL(u)(B_{ik}) = \sum_{B_j \in V_{ik}} w(B_i, B_j) u(B_j). \tag{2.15}$$

For additional information regarding the mathematical determination of the weighting factors $w(x_i, x_j)$ and $w(B_i, B_j)$, the reader is referred to the full description of the algorithm, which can be found in [132, 136].

Since blocks partially overlap, multiple estimations for $NL(u)(x_i)$ are obtained for each of the different blocks to which it belongs. The various estimations given by different blocks $NL(u)(B_{ik})$ are stored in a vector A_i from which the final restored intensity of a voxel x_i

is calculated according to Eq. 2.16 [132].

$$NL(u)(x_i) = \frac{1}{|A_i|} \sum_{p \in A_i} A_i(p). \tag{2.16}$$

Key differences between the classic voxel-wise NLM, originally described by Buades et al. [135], and the blockwise approach implemented by Coupé et al. [132] are presented in Figure 2.1. In the implementation applied in this work [131], selection of the smoothing parameter was automated as a function of global standard deviation of the noise estimated from the image volume and number of coils in the receiver array. Noise estimation was based on a Rician noise distribution [132, 136]. Optimal parameters (e.g. patch radius (PR), block radius (BR)) were tested and defined for each dataset. Examples of NLM denoising results for 2D TIR and 2D MSE data is given in Figures 2.2 and 2.3 respectively.

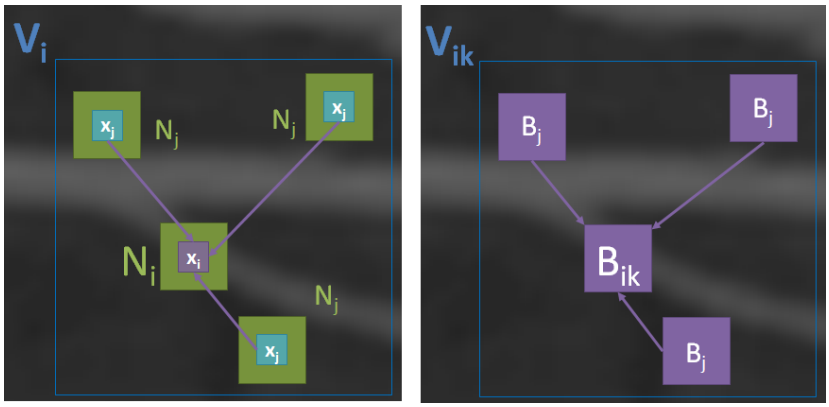

Figure 2.1: 2D representation of the classical NLM principle (left) where weighting $w(x_i, x_j)$ takes all voxelsin the search radius V_i into account. 2D representation of the blockwise NLM implementation (right), where weighting is determined from blocks $w(B_i, B_j)$ in the search radius V_{ik}. Image adapted from [132].

Compared with neighbourhood filtering methods, classical NLM offers improved robustness and the preservation of structures due to its comparison of not only grey levels at a single point, but also of the geometric configuration of neighbourhoods [135]. The optimised blockwise NLM denoising algorithm applied in our work was found to outperform both the classical version [132], as well as alternative denoising methods based on anisotropic diffusion [137] and total variation minimisation processes [138]. This evaluation was performed using a set of synthetically generated T1w and T2w MR images (9% Rician noise) and performance was measured in terms of peak signal to noise ratio [132]. Furthermore, blockwise NLM with the assumption of Rician noise has specifically demonstrated improved robustness when estimating diffusion related parameters such as ADC [139]. For the analysis of quantitative MRI data, NLM and extensions thereof have been applied to control noise propagation [140] and improve precision [130] in parameteric maps.

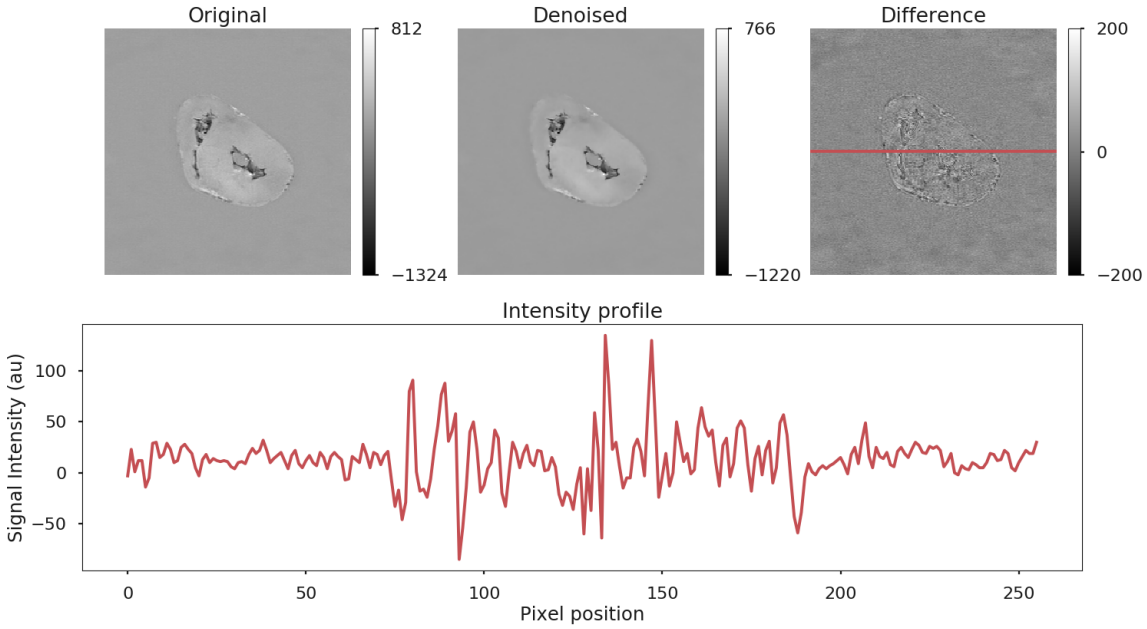

Figure 2.2: Example of image denoising in 2D TIR data (TI = 600 ms). Original image (left) and NLM restored voxel intensities (middle). The difference image (right) displays the difference between original and denoised data. An intensity profile corresponds to signal intensities along the red line in the difference image.

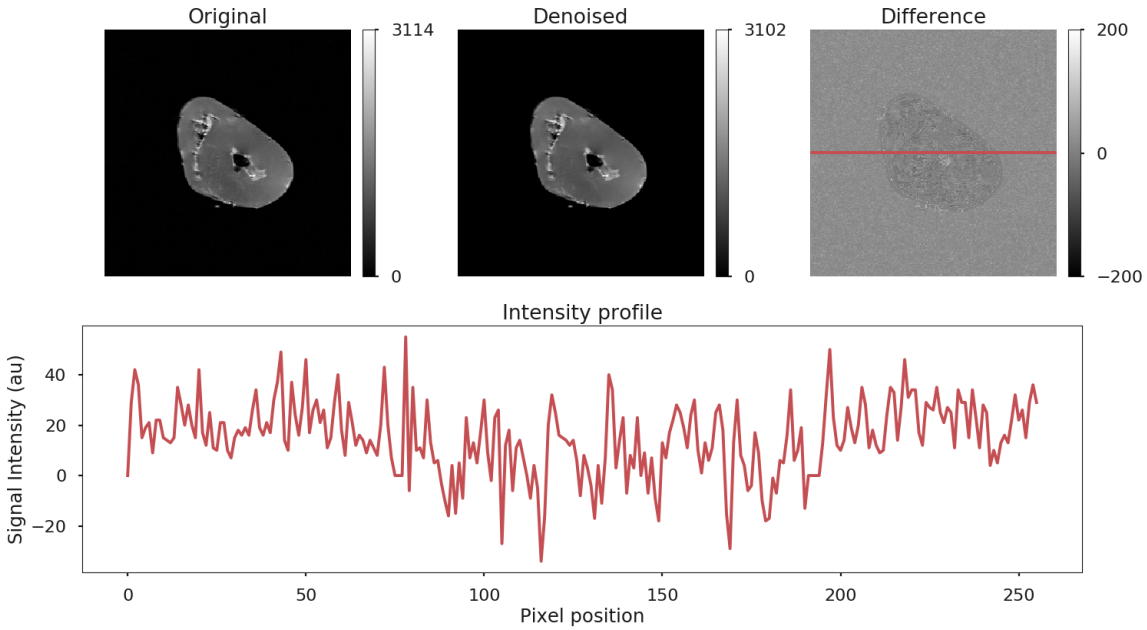

Figure 2.3: Example of image denoising in 2D MSE data (TE = 21.2 ms). Original image (left) and NLM restored voxel intensities (middle). The difference image (right) displays the difference between original and denoised data. An intensity profile corresponds to signal intensities along the red line in the difference image.

Data extraction

Different approaches were implemented to mask image background, depending on the acquired data. For experiments investigating extravasation, segmentation was achieved using a semi-automatic active contour segmentation in ITK-SNAP [141]. Segmentations were performed using TIR data (single inversion time, TI = 100 ms) and applied to additional images acquired at the same point in time (no movement of sample). For images acquired during the animal experiments involving induced MI, the noise mask generated in Python [128] to estimate SNR was applied to remove image background.

Parameter fitting (T_1, T_2)

For *in vitro* samples, slice-wise parameter fitting was performed using average signal intensity in each ROI (Chapter 3). For all other data, voxel-wise parameter fitting was performed. Signal intensity data were fitted using non-linear least squares. Parameter fitting was implemented in R [142] using the NLME package [143] nlslist function (Chapter 3), in Matlab R2016 (Chapter 5) using *lsqcurvefit* and in Python [128] *lmfit* [144] (Chapter 6). Mono-exponential behaviour was assumed for T_1 recovery as well as for T_2 decay in *in vitro* samples and *ex vivo* myocardium. Parameter fitting was performed according to Eq. 2.17 [145] and Eq. 2.18 [145].

$$S(TI) = S_0(1 - 2Ae^{(\frac{-TI}{T_1})}). \tag{2.17}$$

$S(TI)$ is the signal measured at a given inversion time TI using an inversion recovery sequence. The fitted parameters in Eq. 2.17 correspond to the signal that would be acquired from the equilibrium longitudinal magnetization S_0, a correction factor for incomplete inversion approaching one A and the longitudinal relaxation time T_1.

T_2 decay was modelled according to 2.18, with the first echo from the MSE acquisition discarded as suggested in [146, 147]

$$S(TE) = S_0e^{(\frac{-TE}{T_2})}. \tag{2.18}$$

$S(TE)$ is the signal measured as a function of echo time TE, where the fitted parameters correspond to the signal that would be acquired from the equilibrium longitudinal magnetization S_0 and the transverse relaxation time T_2.

Diffusion Tensor Modelling

The shorter transverse relaxation times in myocardium compared to brain tissue impose intrinsic limitations on TE in cardiac DTI [120]. Additionally, increased B_0 inhomogeneities due to the location of the heart in the thorax and the increased presence of air in the post-mortem cadaver or surrounding *ex situ* samples can induce susceptibility-related distortions in Echo Planar Imaging (EPI) sequences [120]. Nevertheless, the lack of cardiac motion in a post-mortem context presented an opportunity to explore diffusion-related parameters in myocardium. DTI was applied in the examination of *ex vivo* porcine hearts following induced myocardial infarction. DTI analysis was performed in Python (*dipy.reconst.dti*) [131].

Since molecule displacement cannot be precisely determined, molecular diffusion behaviour can only be described by modelling the distribution of possible locations (diffusion propagator) [131]. Modelling the diffusion tensor signal was performed according to Eq. 2.19 under the assumption that the diffusion propagator is described by a single 3D Gaussian distribution [131].

$$\frac{S(g_k, b)}{S_0} = e^{-b g_k^T D g_k}. \tag{2.19}$$

S_0 is the signal in the absence of the applied magnetic diffusion gradient (i.e. b = 0), and $S(g_k, b)$ is the signal in measured in the gradient directions g_k [148]. A 3 x 3 symmetric matrix D (diffusion tensor) was fitted in a voxel-wise manner according to Eq. 2.20 to describe diffusion in all directions within a given voxel [149]. The elements D_{xx},D_{yy} and D_{zz} correspond to the diffusion coefficients in the x, y and z directions [149].

$$D = \begin{pmatrix} D_{xx} & D_{xy} & D_{xz} \\ D_{yx} & D_{yy} & D_{yz} \\ D_{zx} & D_{zy} & D_{zz} \end{pmatrix}. \tag{2.20}$$

B-values (Eq. 2.21, [148]), which depend on parameters related to the duration of the gradient δ, centre to centre spacing between pulses Δ, gradient amplitude G as well as the gyromagnetic ratio for ^{1}H γ were extracted from the image metadata. The b-vectors describing the encoding of the different directions in which the field gradient was applied were also extracted from the metadata.

$$b = \gamma^2 G^2 \delta^2 (\Delta \frac{-\delta}{3}). \tag{2.21}$$

Due to the symmetry of the diffusion tensor, $D_{xy} = D_{yx}$, $D_{xz} = D_{zx}$ and $D_{zy} = D_{yz}$, D is essentially comprised of only six unique elements. Ideally, the diffusion tensor is viewed

in a coordinate system based on a centred 3D ellipsoid, which is described by its three eigenvectors (ε_1, ε_2 ,ε_3) and corresponding eigenvalues ($\lambda_1 \geq \lambda_2 \geq \lambda_3$) [149]. These values form the basis of parameter maps in DTI and enable the voxel-wise calculation of additional parameters such as fractional anisotropy (FA) and mean diffusivity (MD) according to Eq. 2.22 and 2.23 [150].

$$FA = \sqrt{\frac{(\lambda_1 - \lambda_2)^2 + (\lambda_1 - \lambda_3)^2 + (\lambda_2 - \lambda_3)^2}{2(\lambda_1^2 + \lambda_2^2 + \lambda_3^2)}} \tag{2.22}$$

$$MD = \frac{(\lambda_1 + \lambda_2 + \lambda_3)}{3}. \tag{2.23}$$

Registration

In cases where samples or porcine hearts were not moved during a single scan session and where data were acquired with identical matrices and field-of-view (FOV), image registration was not performed. Nevertheless, for certain data sets image registration was required due to differences in resolution or removal of porcine hearts from the scanner (overnight). Image registration was performed in Matlab R2016 (Chapter 5) and with a Python (Version 3.4) [151] implementation of SimpleElastix [152] (Chapter 6). A more comprehensive description of the image registration procedure applied is found in the corresponding chapters.

2.4 Image analysis

A detailed description of image analysis procedures undertaken in each phase of this work is provided in the upcoming chapters. Generally, image analysis was performed on morphological MR images as well as on the generated parametric maps. Analysis was based on a ROI or voxel of interest (VOI) approach. VOIs were defined over multiple slices, while ROIs generally corresponded to a region in a single slice. In a forensic context, this approach has been applied in post-mortem MRI studies [30, 65, 84, 88] as well as in the examination of myocardial enhancement following PMCTA [105, 106]. For ROI-based image analysis in this work, manual segmentation was used to define ROIs. The manual definition of ROIs was deemed particularly suitable in this work as it enabled comparison with histological samples taken following macroscopic examination (e.g. in Chapter 6).

2.5 Statistical analysis

2.5.1 Relative standard deviation

Relative standard deviation (RSD), also termed the coefficient of variation, describes standard deviation in relation to the mean. RSD is expressed as a percentage and was calculated according to Eq. 2.24 from the standard deviation σ_x and mean $\hat{x}$.

$$RSD = \frac{\sigma_{x_{T_1,T_2}}}{\hat{x}_{T_1,T_2}} * 100. \tag{2.24}$$

2.5.2 Goodness-of-fit

The goodness-of-fit of the various models established in this work was assessed and statistically verified to ensure that models were appropriate for application and that they explained the underlying data to a suitable degree. To evaluate the accuracy of predicted responses ($\hat{y}_i$) against data values (y_i), either the residual standard error (RSE) or root mean squared error (RMSE) were used. Specific application of these statistical estimators is provided in the relevant upcoming chapters. Briefly, RSE is used to estimate the variability of predicted responses taking into consideration the degrees of freedom (DF) and is calculated according to Eq. 2.25.

$$RSE = \sqrt{\frac{\sum_{i=1}^{n}(\hat{y}_i - y_i)^2}{DF}}. \tag{2.25}$$

The root mean squared error (RMSE), a known measure of the goodness-of-fit for models, assesses the accuracy of predicted responses considering the sample size (n).

$$RMSE = \sqrt{\frac{\sum_{i=1}^{n}(\hat{y}_i - y_i)^2}{n}}. \tag{2.26}$$

2.5.3 Statistical tests

A number of statistical tests (e.g. test for normality, test for equal sample variance, test for equal means between two samples) were applied to determine the significance of quantitative MR parameter mapping results in infarcted and remote post-mortem porcine myocardium. These tests, the corresponding hypotheses and assumptions are detailed in Chapter 6. To assess correlation, Pearson's correlation coefficient (Pearson's r) was used.

3 *In vitro* characterisation of potential perfusates for PMMRA

An *in vitro* approach was taken to characterise selected perfusates across a forensically relevant temperature range. Specifically, the viscosity and relaxation behaviour (T_1,T_2) were determined at three (viscosity) or four (relaxation) temperatures. The temperature dependence of these characteristics was also modelled. Finally, perfusates were evaluated resulting in the definition of a small group of suitable perfusates for application in routine PMMRA.

This chapter summarises the methods and results published in [92].

3.1 Methods

This section details the methods used for the *in vitro* characterisation of selected perfusates and modelling of their relaxation and physical properties.

3.1.1 Samples

The preliminary selection of liquids was based on perfusates used in current applications of PMCTA [4, 9, 153, 154]. These were supplemented with additional solutions with similar physical and/or relaxation properties. *In vitro* experiments were complemented by numerical investigation of a well-characterised clinical contrast agent, Gadovist®.

In vitro experiments

The longitudinal and transverse relaxation behaviour as well as the dynamic viscosity of liquids considered potentially suitable for post-mortem MR angiography (n=9) were characterised at different temperatures between 0.6 and 23.2°C. This temperature range reflects forensically relevant temperatures. Both hygroscopic and lipophilic solutions were investigated experimentally. A brief description of these liquids is provided in Table 3.1.

Table 3.1: Summary of perfusates characterised *in vitro* including their chemical nature.

Liquid	Nature	Description
Angiofil®	Lipophilic	Oil-based, non-polar CT contrast component
Paraffin Oil & Angiofil® (6% PA)	Lipophilic	Mixture of paraffin oil and Angiofil® (6%)
Paraffin oil	Lipophilic	Highly refined mineral oil, n-alkane based
PEG200	Hygroscopic	Polyethylene glycol (PEG200), mol wt: 190-210)
PEG400	Hygroscopic	Polyethylene glycol (PEG400), mol wt: 380-420)
Silicon oil	Lipophilic	Liquid polymerized siloxane (polydimethylsiloxane)
232 Hydroseal® (232H)	Lipophilic	Hydrocarbons (C13-16, <0.03% aromatics)
240 Hydroseal® (240H)	Lipophilic	Hydrocarbons (C15-20, <0.03% aromatics)
250 Hydroseal® (250H)	Lipophilic	Hydrocarbons (C15-20, <0.03% aromatics)

Gadovist®-doped water

Gadovist®-doped water was numerically investigated using temperature dependencies obtained from the literature (dynamic viscosity of water [155]) and experiments determining relaxation times (T_i) of water [156] and relaxivities (r_i) of Gadovist® [157].

Viscosity behaviour was assumed to follow that of pure water given the low concentration of Gadovist® ($<$ 2 mmol/l). Relaxation times T_i of an aqueous Gadovist® solution are a function of Gadovist® concentration c, Gadovist® relaxivities r_i and the relaxation rate of pure water $R_{i_{H_20}}$, with r_i and $R_{i_{H_20}}$ being temperature dependent. Therefore, T_i was calculated according to Eq. 3.1 accounting for the modelled temperature dependence described by Eq. 3.4 and Eq. 3.5.

$$\frac{1}{T_i} \equiv R_i = R_{i_{H_20}} + c \times r_i, \qquad i = 1, 2. \tag{3.1}$$

3.1.2 Experimental and image acquisition protocols

In this section the experimental set-up and acquisition protocols for MR imaging, viscosity and density measurements is described.

Quantification of relaxation behaviour

MRI measurements were performed on liquids in polypropylene test tubes at four temperatures: 1.4, 8.6, 16.1 and 23.2°C (TIR) and 0.6, 8.4, 16.1, 23.2°C (MSE) according to the parameters in Table 3.2.

Table 3.2: Scan parameters for acquisition of quantitative MRI data in *in vitro* experiments

	Resolution (mm)	Slices	TR (ms)	TE (ms)	FA (°)	BW (Hz/Px)	Additional information
2D TIR	0.6 x 0.6 x 3	10	12000	9.7	–	200	TI=50, 100, 200, 350, 600, 1000, 4000, ETL = 8.
2D MSE	0.6 x 0.6 x 4.5	8	4000	10.6	–	200	32 equally spaced echoes.
2D MSE	0.6 x 0.6 x 4.5	8	4000	20	–	200	32 equally spaced echoes.

Sample temperature was controlled using a water bath and monitored via a real-time fiber optic temperature sensor (Fluoroptic®, LumaSense Technologies Inc, USA). Samples were given sufficient time to adjust between measurements performed at different temperatures. Signal intensity (SI) data from individual ROIs were fitted for each imaging slice according to Eq. 2.17 and 2.18 to determine the slice-wise longitudinal and transverse relaxation of all perfusates.

An example of the manually segmented ROIs corresponding to the investigated liquids is presented in Figure (3.1). Each ROI contained 270 pixels.

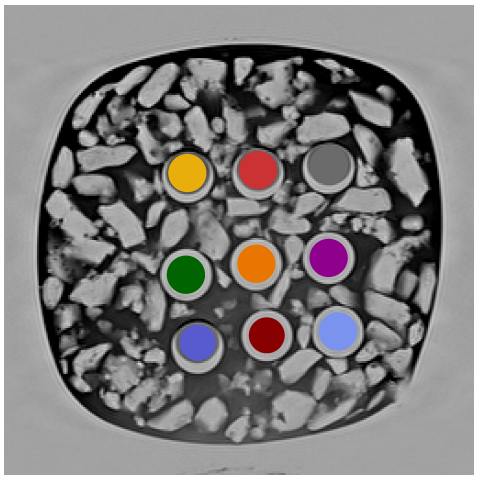

Figure 3.1: Example of ROIs for the *in vitro* characterisation of perfusates. A single slice is presented in which colours correspond to individual perfusates.

Dynamic viscosity

An Ubbelohde viscometer (Schott AG, Germany) and density meter (DMA 48, Anton Paar GmbH, Austria) were used for kinematic viscosity and density measurements. Measurements were conducted at 8, 10 and 20°C. For each perfusate, three measurements of kinematic viscosity and density were performed. Using density values, the obtained kinematic viscosities

were converted to dynamic viscosity according to Eq. 3.2 [158].

$$\mu = \nu\rho. \tag{3.2}$$

μ is the dynamic (absolute) viscosity (mPa·s), ν the kinematic viscosity (mm^2/s) and ρ the density (g/cm^3). Values obtained at 20°C were verified against supplier values. To facilitate comparison and evaluation of liquids, three viscosity categories were defined (low: <6, medium: 32-65, high: >65 mPa·s). For Gadovist®-doped water, water values for dynamic viscosity [155], were used because the low concentration of Gadovist® (2 mmol/l) was not expected to significantly influence the dynamic viscosity of water.

3.1.3 Modelling of temperature dependence

Using the temperature recorded during experimental determination T_1, T_2 and dynamic viscosities, the correlation between these properties and temperature was determined. This relationship was quadratically modelled.

Relaxation (*in vitro* experiments)

The temperature dependence of relaxation times was described by a empirical quadratic model (Eq. 3.3) for temperatures between 1-23°C.

$$T_i(\vartheta) = T_i(23°C) + A_{T_i}\Delta\vartheta + B_{T_i}\Delta\vartheta^2, \qquad i = 1, 2. \tag{3.3}$$

Relaxation times T_i at a given temperature ϑ were calculated from known relaxation times at 23°C$T_i(23°C$, the temperature difference $\Delta\vartheta = 23 - \vartheta(°C)$ and the coefficients A_{T_i} and B_{T_i}, which were determined for each potential perfusate.

Relaxation (numerical model)

The relaxation times T_i of water [156] and the relaxivities r_i of Gadovist® [157] are described as function of temperature ϑ in Eq. 3.4 and Eq. 3.5.

$$r_i(\vartheta) = r_i(0°C) + A_{r_i}\vartheta + B_{r_i}\vartheta^2. \tag{3.4}$$

$$T_i(\vartheta) = T_i(0°C) + A_{T_i}\vartheta + B_{T_i}\vartheta^2. \tag{3.5}$$

The corresponding model coefficients A_{T_i}, B_{T_i}, A_{r_i} and B_{r_i} are summarised in Table 3.3.

Table 3.3: Coefficients for the temperature dependence of water (T_1, T_2 [156]) and Gadovist® relaxivities (r_1, r_2 [157]).

Liquid	Type of rate	(0°C)	A	B
Water	T_1	1655.4	-18.86	1.3
Water	T_2	673.1	12.12	0
Gadovist®	r_1	8.55	-0.25	0.003
Gadovist®	r_2	9.82	-0.24	0.003

Dynamic viscosity

The empirical quadratic model (Eq. 3.6) was used to describe the temperature dependence of the quantified dynamic viscosities for temperatures between 8-20°C.

$$\mu(\vartheta) = \mu(20°C) + A_{visc}\Delta\vartheta + B_{visc}\Delta\vartheta^2. \tag{3.6}$$

Dynamic viscosity μ at a given temperature ϑ was calculated from the dynamic viscosity at 20°C, the difference in temperature $\Delta\vartheta = 20 - \vartheta(°C)$ and two coefficients A_{visc} and B_{visc}, which were determined for each potential perfusate.

Perfusate evaluation and statistical analysis

Optimal properties for perfusate suitability were defined as follows:

- ⇒ Medium viscosity (15-100 mPa·s over the defined temperature range) [153, 159]
- ⇒ Perfusate T_1 shorter than cadaveric tissue
- ⇒ Perfusate T_2 longer than cadaveric tissue
- ⇒ Minimal temperature dependence between 0-23°C

Relative standard deviation (RSD) of relaxation times was calculated according to Eq. 2.24 over all slices. Pearson's *R* was used to assess the correlation between the physical and MR relaxation characteristics and temperature. Residual standard error (RSE), defined in Eq. 2.25, was used to evaluate the goodness-of-fit of the established models.

3.2 Results

According to the methods described above, the relaxation times and dynamic viscosities were experimentally determined for all perfusates. Relaxation times and dynamic viscosity for Gadovist®-doped water were numerically determined for comparison purposes. Temperature dependency models for each of the perfusates were established and perfusate suitability for routine PMMRA was assessed.

3.2.1 Characterisation and temperature dependence of dynamic viscosity

Dynamic viscosities for all perfusates are listed in Table 3.4. Measurements at 20°C were in general agreement with supplier data.

Table 3.4: Dynamic viscosities (mPa·s) for all perfusates grouped into three categories: Low ($<$ 6 mPa·s), medium (32-65 mPa·s) and high (65-285 mPa·s)

Group	Perfusate	Dynamic Viscosity in mPa·s (mean ± SD)		
		8°C	10°C	20°C
Low	232H	4.221 ± 0.007	4.010 ± 0.006	2.930 ± 0.004
	240H	5.62 ± 0.01	5.28 ± 0.01	3.730 ± 0.002
	250H	5.62 ± 0.01	5.21 ± 0.01	3.730 ± 0.003
Medium	Paraffin oil	64.6 ± 0.1	57.3 ± 0.2	32.23 ± 0.04
	6% PA	65.5 ± 0.1	58.1 ± 0.2	32.52 ± 0.06
High	PEG200	138.2 ± 0.8	121.1 ± 0.7	64.5 ± 0.3
	Angiofil®	203.2 ± 0.8	179.2 ± 1.1	91.4 ± 0.2
	Silicon oil	128.9 ± 0.1	122.7 ± 0.7	97.3 ± 0.1
	PEG400	284.3 ± 1.4	237 ± 1.4	128.7 ± 0.4

The highly temperature-dependent nature of dynamic viscosity (negative correlation) was experimentally confirmed. Experimental data was modelled for all samples according to Eq. 3.6. The generated models are displayed in Figure 3.2 and the corresponding model coefficients are presented in Table 3.5.

The calculated RSE was small ($<$1.17 mPa·s) for all models indicating excellent goodness-of-fit. Polyethylene glycol and Angiofil® samples demonstrated the highest temperature dependence. Although temperature was found to influence all perfusates, temperature-related changes in dynamic viscosity of paraffin oil, 6% PA, silicon oil and 232H/240H/250H were minimal ($A_{visc} <$ -1.6, $B_{visc} <$ 0.097) over the investigated temperatures.

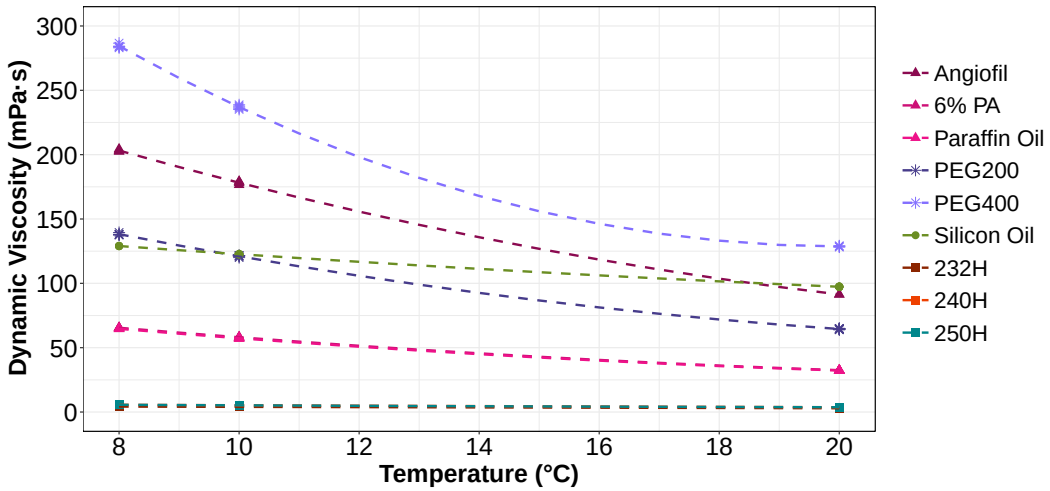

Figure 3.2: Experimentally measured dynamic viscosities (mPa·s) of potential perfusates at 8, 10 and 20°C and corresponding temperature dependence models according to Eq. 3.6.

Table 3.5: Reference dynamic viscosity (μ) at 20°C, model coefficients (A_{visc}, B_{visc}) for modelled temperature dependence of dynamic viscosity according to Eq. 3.6 and the RSE for each model.

Perfusate	μ(20°C)	A_{visc}	B_{visc}	RSE (mPa·s)
Angiofil®	91.4	-5.51	0.318	0.86
6% PA	32.5	-1.62	0.094	0.15
Paraffin oil	32.2	-1.54	0.097	0.11
PEG200	64.5	-3.22	0.243	0.54
PEG400	128.7	-0.11	1.072	1.16
Silicon oil	97.3	-2.00	0.053	0.16
232H	2.9	-0.11	-0.0003	0.0055
240H	3.7	-0.14	0.002	0.0084
250H	3.7	-0.10	0.005	0.0071

On the other hand, PEG400, PEG200 and Angiofil® demonstrated strong temperature dependence ($A_{visc} >$ -3.2, $B_{visc} >$ 0.318) evidenced by much larger temperature coefficients.

Given the defined optimal physical properties for suitable perfusates, paraffin oil and the 6% PA solution were preferred based on their medium dynamic viscosity (Figure 3.2). Furthermore, the low coefficients in the quadratic model describing the temperature dependence of these solutions (Table 3.5) indicated minimal temperature dependence, corresponding to minimal changes in viscosity over a forensically relevant temperature range.

3.2.2 Characterisation and temperature dependence of T_1 and T_2

Stability of temperature measurements

The stability of temperature measurements was verified before temperature values were used as the basis for the models proposed in this work. Sample temperature measurements were stable over the duration of each scan session with the standard deviation of measurements being less than 0.7°C for all temperatures (Table 3.6).

Table 3.6: Scan sessions and corresponding temperatures for each acquisition sequence.

	Sequence	Temperature in °C (mean ± SD)
1	TIR	1.0 ± 0.4
	MSE	0.6 ± 0.3
2	TIR	8.6 ± 0.3
	MSE	8.4 ± 0.2
3	TIR	16.1 ± 0.3
	MSE	15.9 ± 0.4
4	TIR	23.2 ± 0.6
	MSE	23.2 ± 0.4

Concentration of Gadovist

The concentration of Gadovist® was numerically investigated (Figure 3.3) to ensure a strong T_1 shortening effect in the carrier solution (water). Figure 3.3 demonstrates simulations of T_1 values for various concentrations of Gadovist® in water. The model of temperature dependence was taken from Kruisz et al [156, 157]. A concentration of 2 mmol/l was selected for comparison with experimentally investigated perfusates.

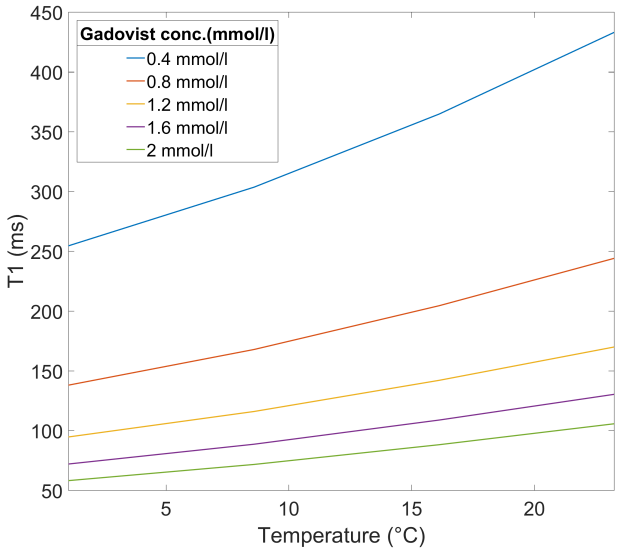

Figure 3.3: Temperature and concentration dependence of T_1 of Gadovist®-doped water based on numerical simulations. Temperature coefficients from [156, 157].

Relaxation time temperature-dependency models

The relative standard deviation of T_1 and T_2 relaxation times in the fitted data was small (RSD <3.2%). Positive correlations between temperature and relaxation times were observed for both T_1 (Pearson's $r > 0.912$) and T_2 (Pearson's $r > 0.941$). This correlation was stronger for some samples (e.g. Hydroseal®) than for others (e.g. paraffin oil, Angiofil®). The temperature dependence of T_1 and T_2 was reliably modelled according to Eq.3.3. The RSE of the resulting models was small (Table 3.7) indicating excellent goodness-of-fit.

Table 3.7: Reference relaxation times (T_1 and T_2) at 23°C with coefficients ($A_{T_{(1,2)}}$, $B_{T_{(1,2)}}$) for modelled temperature dependence of T_1 and T_2 (ms) according to Eq.3.3 and corresponding residual standard error (ms) for each model.

Perfusate	T_1				T_2			
	T_1 (23°C)	A_{T_1}	B_{T_1}	RSE	T_2 (23°C)	A_{T_2}	B_{T_2}	RSE
Angiofil®	214.8	3.5	0.08	3.5	157.7	5.4	0.10	4.8
6 % PA	205.5	4.7	0.11	2.7	144.1	4.4	0.07	2.4
Paraffin oil	206.7	4.9	0.12	2.7	144.3	4.8	0.09	2.4
PEG200	216.2	9.5	0.24	3.4	139.4	6.7	0.15	1.0
PEG400	201.9	8.1	0.20	3.2	123.5	6.8	0.15	1.6
Silicon oil	999.4	14.1	0.27	10.7	545.5	15.1	0.32	15.5
232H	729.6	24.8	0.53	7.2	233.6	2.7	-0.04	9.7
240H	597.0	20.6	0.43	4.6	223.0	4.3	0.04	6.5
250H	611.5	21.4	0.46	4.6	229.0	5.9	0.10	7.0

The acquired data and their corresponding temperature dependency models are presented in Figure 3.4 and Figure 3.5, where differences in the relaxation behaviour (T_1, T_2) of potential perfusates and cadaver tissue are identifiable.

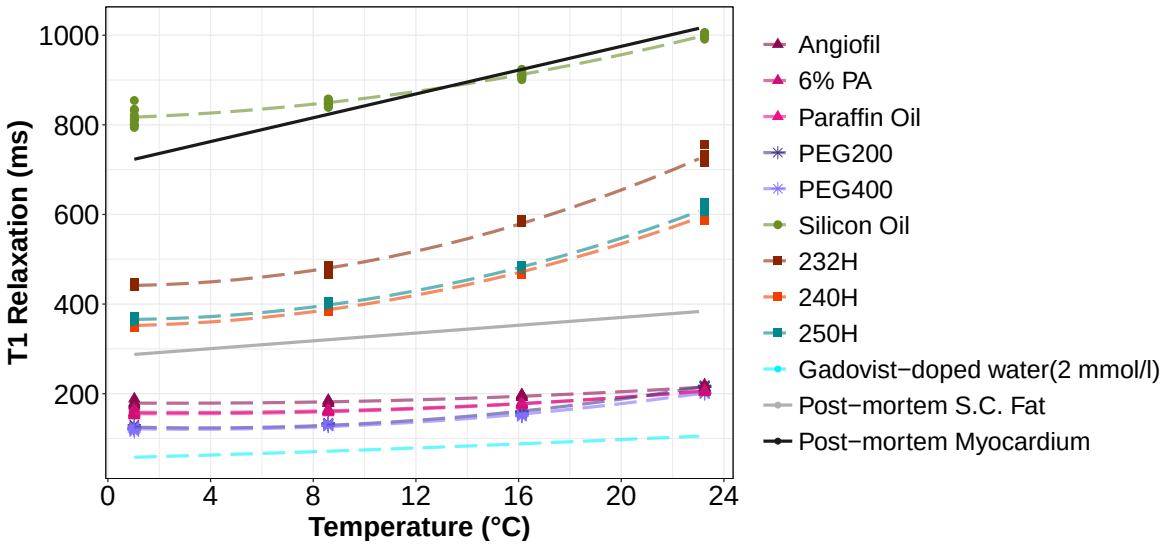

Figure 3.4: Fitted relaxation times (T_1) from experimental measurements of of potential perfusates at 1, 8.6, 16.1 and 23.2°C with their corresponding temperature dependence models according to Eq. 3.3. For comparison, numerically investigated cadaveric tissue [64] and Gadovist®-doped water (2 mmol/l) [156, 157] are also displayed.

With the exception of silicon oil, T_1 relaxation in all potential perfusates was distinctly shorter than that of cadaveric myocardium. Good positive contrast could therefore be expected between any of these perfusates and myocardium using T1-weighted imaging. A similar observation was made for cadaveric subcutaneous fat, albeit that the Hydroseal® samples (232H, 240H and 250H) would, in this case, not contrast positively against cadaveric s.c. fat due to their longer T_1.

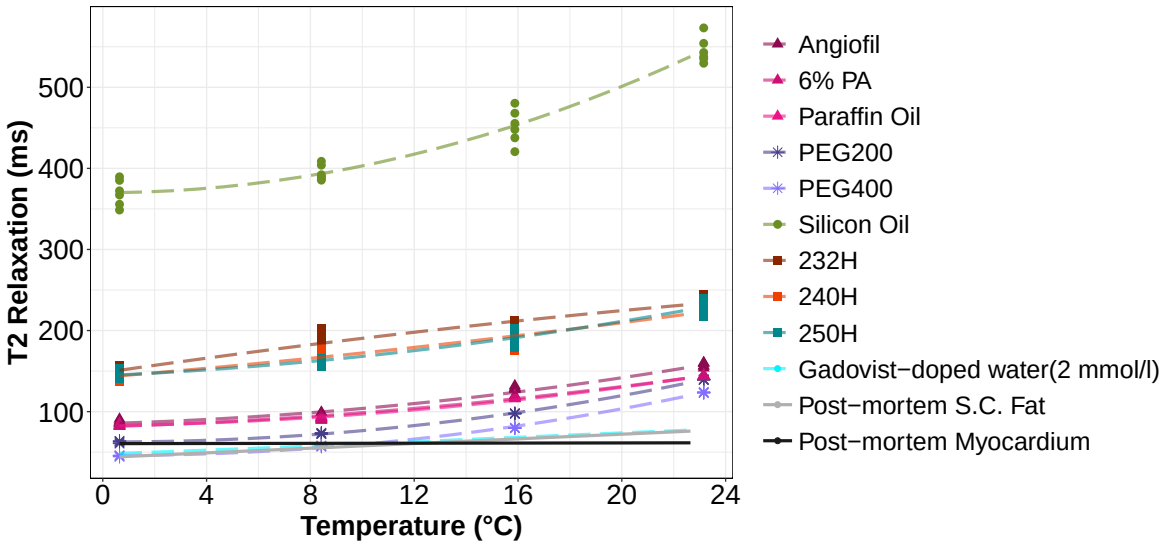

Figure 3.5: Fitted relaxation times (T_2) from experimental measurements of of potential perfusates at 0.6, 8.4, 15.9 and 23.2°C with their corresponding temperature dependence models according to Eq. 3.3. For comparison, numerically investigated cadaveric tissue [64] and Gadovist®-doped water (2 mmol/l) [156, 157] are also displayed.

T_2 relaxation times for cadaveric tissue and potential perfusates were much closer together. Nevertheless, all lipophilic perfusates demonstrated slightly longer transverse relaxation times compared to the investigated tissues, indicating positive contrast in T2-weighted images.

Overall, T_1 values for PEG, paraffin oil, Angiofil®, 6% PA and Gadovist®-doped water (2 mmol/l) lay at least 100 ms below corresponding cadaveric tissue values. For all perfusates except PEG and Gadovist®-doped water (2 mmol/l), T_2 values were longer than tissue T_2. Preferred perfusates based on relaxation properties were paraffin oil, Angiofil® as well as the 6% PA solution and Gadovist®-doped water (2 mmol/l).

4 Visualisation of vessel-like structures in an *ex vivo* porcine tissue phantom

The MRI contrast achievable is a function of both the intrinsic properties of the tissue (or substance) being examined and the scan parameters that are applied in image acquisition. Given knowledge of the intrinsic relaxation behaviour of the perfusates investigated in Chapter 3, the work presented in this chapter assesses different MR sequences and adapts scan parameters for visualisation of filled post-mortem coronary arteries. These examinations were conducted using an *ex vivo* porcine-cannula phantom representing vessel-like structures in post-mortem tissue.

4.1 Methods

A MRI protocol was established to assess selected clinically available MRI sequences and adapt said sequences for targeted PMMRA of the coronary arteries. The ultimate diagnostic objective of this protocol is to enable differentiation between small filled coronary arteries and post-mortem cardiac tissue, including both myocardium and epicardial fat.

4.1.1 Image acquisition

Images were acquired according to the parameters detailed in Table 4.1.

Table 4.1: Scan parameters for acquisition of MR images to visualise vessel-like structures in an *ex vivo* porcine tissue phantom

Sequence	Resolution (mm)	Slices	TR (ms)	TE (ms)	FA (°)	BW (Hz/Px)	TA (min:sec)
2D TIR	0.44 × 0.44 × 1.5	48	6190	12	180	225	4:38
2D T1w GRE	0.7 × 0.7 × 1.5	65	48	4.7	40	260	2:39
3D T2w SPACE	0.7 × 0.7 × 0.7	88	1600	174	140	460	7:36
2D T1w TSE	0.8 × 0.8 × 4.5	20	700	25	180	850	2:07

Inversion recovery sequences

The target optimal inversion time (TI_{null}) would result in no signal from epicardial fat in post-mortem heart, thereby maximising contrast through application of a 180° inversion pulse. To determine TI_{null}, the T_1 of epicardial fat was estimated over a forensically relevant temperature range (1 - 23°C) . Temperature-dependent models for T_1 of fat in porcine belly [157] and for human cadaveric subcutaneous fat [84], were used, resulting in estimated T_1 relaxation times for epicardial fat in the range 133-384 ms between 1-23 °C at 3T. Under the assumption that TR greatly exceeds T_1 and according to Eq. 4.1, the corresponding TI_{null} was calculated to be between 92 and 266 ms [109] . For the experimental set up at 13°C, inversion times between 100 and 220 ms were selected for experimental investigation.

$$TI_{null} = T_1 \times \ln 2 \tag{4.1}$$

4.1.2 *Ex vivo* porcine-cannula phantom

The previously mentioned clinical MRI sequences were empirically investigated using an *ex vivo* porcine-cannula phantom (Figure 4.1). The phantom consisted of 12 tubes with three different diameters (2,3,4 mm) and four liquids (silicon oil, 6% PA solution, paraffin oil and mineral oil). Mineral oil was included in these examinations due to its similarity to paraffin oil. Diameter sizes were selected based on the approximate diameter of coronary arteries [160], summarised in Table 4.2.

Table 4.2: Representative vessel diameters for coronary arteries and corresponding tube diameter to evaluate resolution requirements for MR image acquisition. Measurements in healthy male subjects (right or left dominance) according to [160].

Vessel	Lumen diameter (mm)		Tube diameter
	RCA dominant	LCA dominant	(mm)
Left main coronary artery	4.5 ± 0.5	4.6 ± 0.4	4
LAD (proximal)	3.7 ± 0.5	3.8 ± 0.3	4
LAD (distal)	1.4 ± 0.5	1.7 ± 0.4	2
LCX (proximal)	3.4 ± 0.4	4.3 ± 0.6	3 & 4
LCX (distal)	–	2.4 ± 0.5	2
RCA (proximal)	4.0 ± 0.6	2.8 ± 0.5	3 & 4
RCA (distal)	2.4 ± 0.5	–	2

Filled tubes were horizontally inserted into the phantom to represent filled vasculature in a cadaver (Figure 4.1). Images were acquired in the axial orientation. The mean temperature of the phantom over the duration of the experiment was 13°C and showed no significant change over the scan time ($<$ 1 hour).

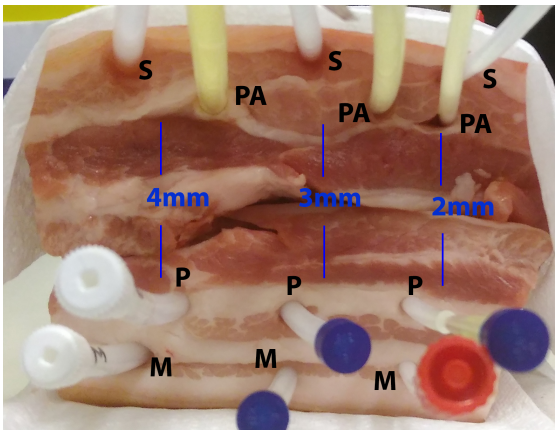

Figure 4.1: Photo of experimental set-up (porcine-cannula model). Tubes with different diameters (2, 3, 4 mm) filled with silicon oil (S), 6% PA (PA), paraffin oil (P) and mineral oil (M).

4.1.3 Image evaluation

With the exception of the perceptual blur metric (Section 2.2.1), all image evaluation was performed on a single slice for each sequence. Slices were selected to correspond to approximately the same position in all imaging volumes (Figure 4.2).

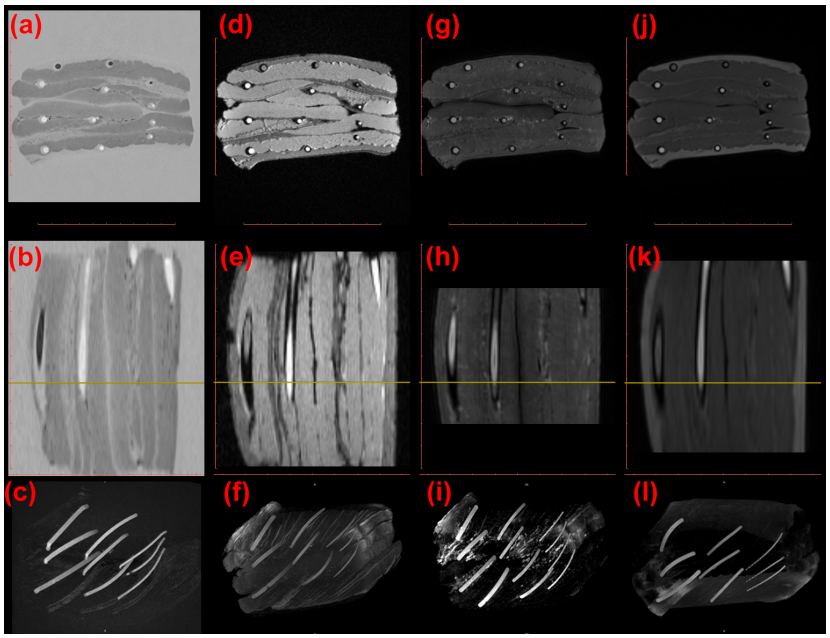

Figure 4.2: Selected slices for image evaluation in the transversal and sagittal orientations, as well as maximum intensity projections (MIP) of the imaging volume for (a-c) TIR (d-f) T1w GRE (g-i) T2w SPACE (j-l) T1w TSE.

2D image intensity profiles were generated for each tube diameter, perfusate and sequence by placing a line through vessel-like structures in the porcine tissue phantom to display intensity as a function of voxel position (Figure 4.3). 2D image intensity profiles were used to compare signal across sequences and to calculate the width of the peak corresponding to the cross-section of filled tubes. Peak widths between minima adjacent to the main peak were determined for each sequence and tube diameter. For the TIR sequence, the peak width was determined between zero intensity values adjacent to the main peak. For a selected slice, 3D image intensity profiles displaying signal intensity as function of in-plane position were generated for a neighbourhood region (Figure 4.3) surrounding each tube to evaluate spread of the peak corresponding to the filled tubes.

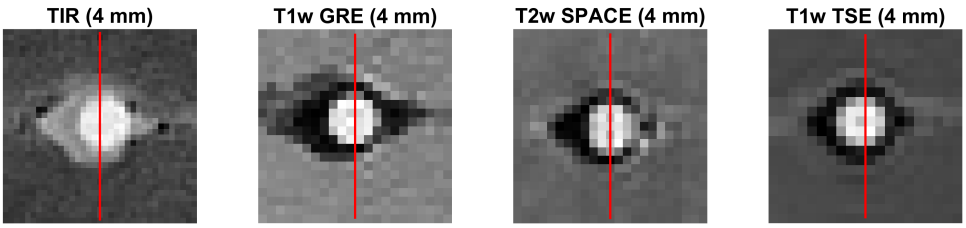

Figure 4.3: Example of neighbourhood region (paraffin oil, diameter = 4 mm) for generation of 3D intensity profiles and line coordinates for generation of 2D intensity profiles (see Figure 4.6)

CNR_{eff} was calculated according to Eq. 2.5. For each perfusate, ROIs at the centre of filled tubes (diameter = 4 mm) were manually segmented in Matlab R2016. ROIs corresponding to muscle, fat and background signal were also manually segmented (Figure 4.4).

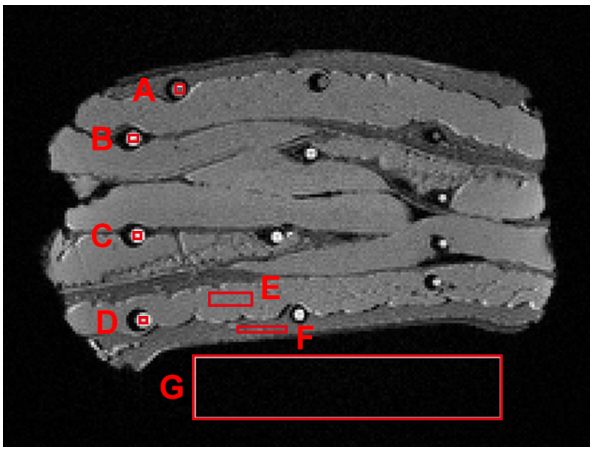

Figure 4.4: Example of ROI placement for calculation of CNR_{eff}. ROIs for each perfusate were placed in 4 mm tubes (A: Silicon oil, B: 6% PA, C: Paraffin oil, D: Mineral oil). ROIs for fat (F) and muscle (E) were placed in the corresponding tissue. The ROI used to calculate image noise (G) was placed in image background.

Image blurriness was assessed using the *perceptual blur metric* described in Section 2.2.1. This metric was applied to each slice individually, with the mean and standard deviation of the resulting blur being used to compare sequences.

4.2 Results

An optimal inversion time was experimentally determined to suppress porcine fat in TIR images. Images acquired at with this TI were compared with those obtained using three other clinically available sequences to evaluate the suitability of selected sequences for PMMRA.

4.2.1 Experimental determination of optimal inversion time

Following estimation of an appropriate range of TI for suppression of porcine fat at approximately 13°C (Eq. 4.1), the inversion time of the 180° inversion pulse was experimentally investigated to optimise suppression of porcine fat. Figure 4.5 displays the SI of voxels corresponding to the investigated perfusates, porcine fat and muscle at various TI. Under the experimental conditions (phantom temperature: 13 °C), the porcine fat signal was optimally nulled at TI = 160 ms. Therefore, TIR images acquired with TI = 160 ms were used for further comparisons with the T1w GRE, T2w SPACE and T1w TSE sequences.

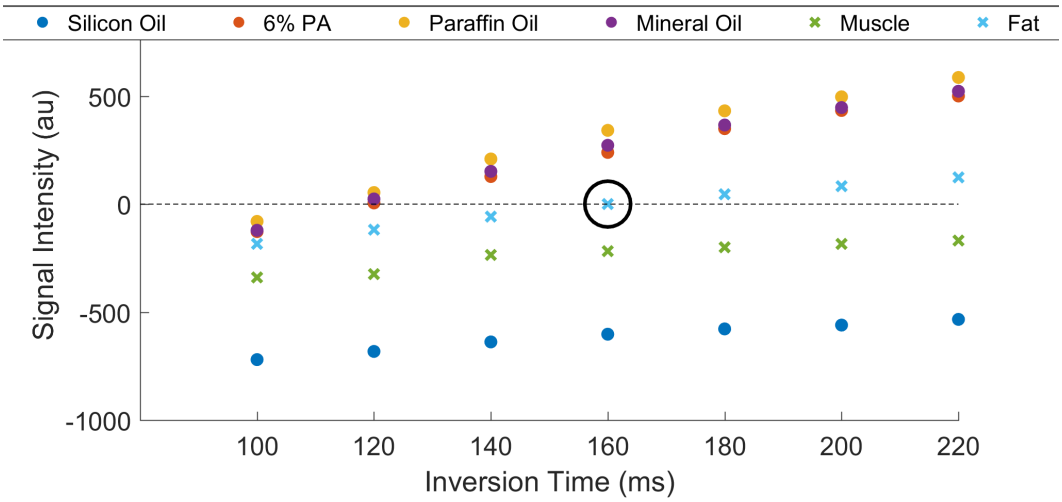

Figure 4.5: Mean signal intensity of each perfusate as well as fat and muscle in the *ex vivo* porcine tissue phantom. Images were acquired at TI = 100-220 ms. TI_{null} of *ex vivo* porcine fat at the investigated temperature (≈13 °C) is highlighted.

4.2.2 Image intensity profiles

Examination of the 2D (line) and 3D (single slice) image intensity profiles for each of the tubes across the four investigated sequences revealed differences in the contrast achieved by a given sequence, and additionally provided an indication of the influence of resolution on the clarity of point-like structures.

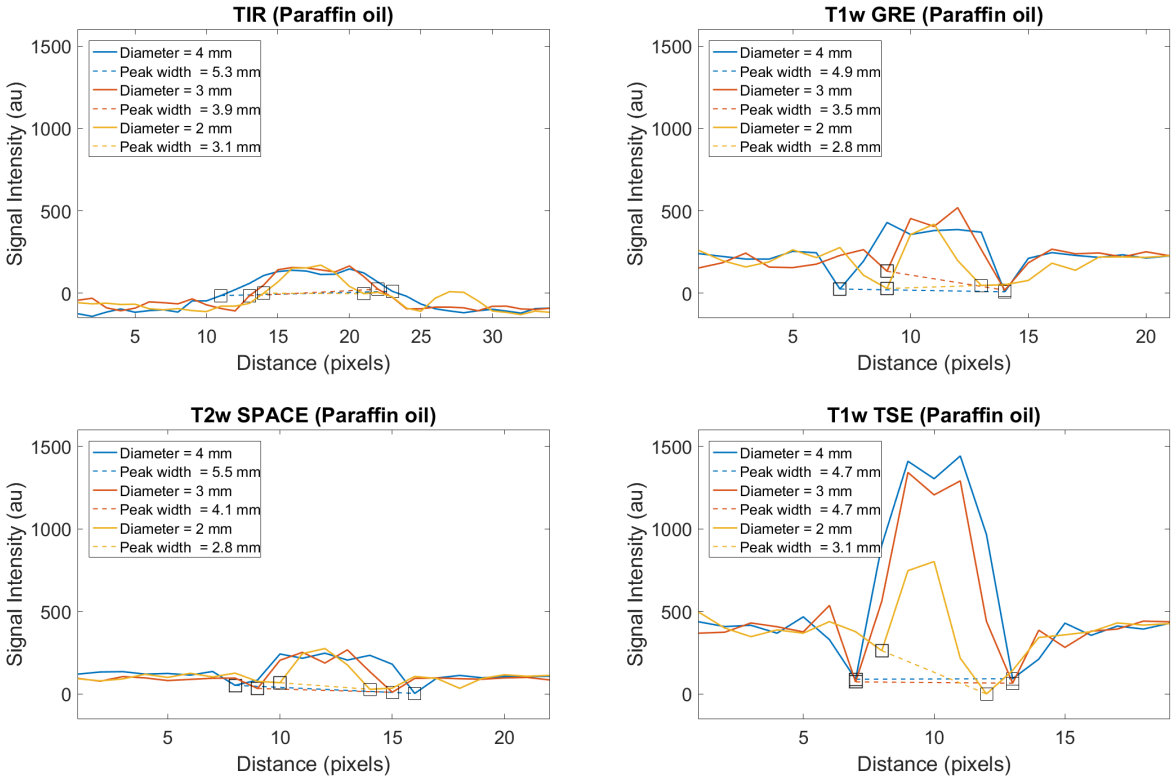

Figure 4.6: 2D image intensity profiles across a cross-sectional image of tubes filled with paraffin oil (2, 3 and 4 mm) for each sequence (TIR, T1w GRE, T2w SPACE, T1w TSE). Peak widths and tube diameters are displayed for comparison. Squares indicate the location of the minima next to the major peak.

Table 4.3: Comparison of tube diameters and the estimated peak width.

Tube diameter (mm)	Overestimation of tube diameter in mm (whole pixels)			
	TIR	T1w GRE	T2w SPACE	T1w TSE
2	1.1 (3)	0.8 (1)	1.1 (1)	1.1 (1)
3	0.9 (2)	0.5 (1)	1.1 (2)	1.7 (2)
4	1.3 (3)	0.9 (1)	1.5 (2)	0.7 (1)

Comparison of inner tube diameters (2, 3, 4 mm) with peak widths estimated at baseline (T1w GRE, T2w SPACE, T1w TSE) or zero intensity (TIR) (Figure 4.6) demonstrated that the measured peak width generally overestimated the actual tube diameter in all sequences, the extent of this effect differed according to the sequence, however all overestimations corresponded to distances of < 2 voxels for all sequences, apart from the TIR sequence. Based on peak width estimates, no sequence overestimated the vessel diameter by more than 1.7 mm. The smallest differences between peak width and the actual inner diameter of tubes were observed in T1w GRE images (Diameter = 2, 3 mm) and T1w TSE (Diameter = 4 mm) (Table 4.3).

Neighbourhood 3D intensity profiles (Figure 4.7) highlighted the differences in the rise of signal intensity towards the center of the filled tube and the total area of the high signal paraffin oil. While 3D peaks from the T1w GRE sequence rose rather steadily, those from the T1w TSE image were more tapered, becoming thinner towards the centre of tube, indicating a change in intensity over the cross-section of the tube.

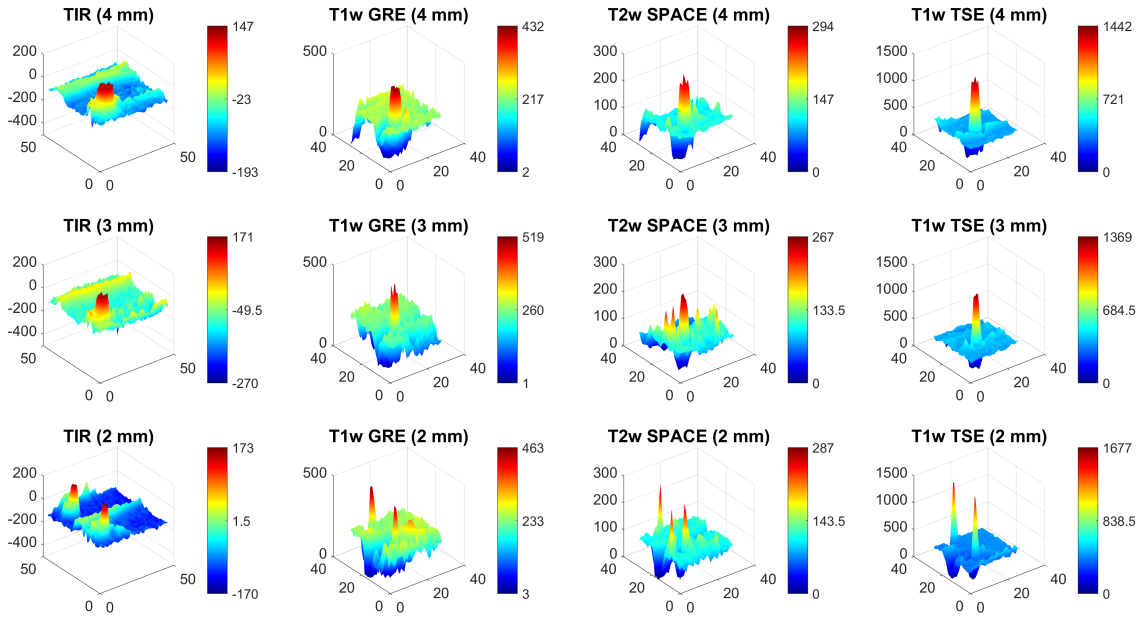

Figure 4.7: 3D image intensity profiles for neighbourhoods directly adjacent to tubes filled with paraffin oil (2, 3 and 4 mm) for each sequence (TIR, T1w GRE, T2w SPACE, T1w TSE).

4.2.3 Effective contrast to noise ratio

CNR_{eff} values for each perfusate against porcine muscle and fat are summarised in Table 4.4.

Table 4.4: CNR_{eff} for silicon oil, 6% PA, paraffin oil and mineral oil in porcine muscle (M) and fat (F) using different imaging sequences (2D TIR, 2D T1w GRE, T2w SPACE and T1w TSE). Negative values indicate negative contrast (i.e. hypointensity)

	TIR		T1w GRE		T2w SPACE		T1w TSE	
	CNR_{eff} (M)	CNR_{eff} (F)	CNR_{eff} (M)	CNR_{eff} (F)	CNR_{eff} (M)	CNR_{eff} (F)	CNR_{eff} (M)	CNR_{eff} (F)
Silicon	-0.03	-0.05	-1.1	0.9	21.9	21.3	11.2	-3.1
6% PA	0.04	0.02	5.9	7.8	23.2	22.6	52.1	37.8
Paraffin oil	0.04	0.03	7.7	9.7	23.6	23.0	49.9	35.6
Mineral oil	0.04	0.02	8.1	10.0	22.5	21.9	51.4	37.1

Silicon oil was hypointense in the TIR (contrast against porcine muscle and fat), TSE (contrast against porcine fat) and GRE acquisitions (contrast against porcine muscle). However, it appeared hyperintense in all other acquired images. All other perfusates generated positive contrast with both porcine muscle and fat. For all perfusates except silicon oil, CNR_{eff} was maximised in the TSE acquisition, followed by the SPACE sequence and GRE sequence. Poorest CNR was obtained for images acquired using the TIR sequence.

4.2.4 Perceptual blur metric

The perceptual blur metric described in Section 2.2.1 was used to assess image blurriness. According to this metric all images displayed low levels of blur. T1w GRE images were characterised as the sharpest (score = 0.196) followed by the T2w SPACE and TIR sequences. The T1w TSE performed least satisfactorily and was determined to be the blurriest of the four assessed images (Table 4.5).

Table 4.5: Perceptual blur metric score according to [129]. Mean and standard deviation over all slices. A small blur effect corresponds to a score near to 0, while large blur effects give a score closer to 1.

Sequences	Mean $\pm$ SD
TIR (TI = 160 ms)	0.228 $\pm$ 0.013
T1w GRE	0.196 $\pm$ 0.011
T2w SPACE	0.225 $\pm$ 0.003
T1w TSE	0.257 $\pm$ 0.009

5 Extravasation of perfusates in *ex situ* porcine hearts

Intravascular retention of perfusates in post-mortem vessels is an important consideration in the development of PM angiography techniques [49]. Selected perfusates (paraffin oil, Gadovist®-doped physiological solution and polyethylene glycol) were injected into the left anterior descending artery of *ex situ* porcine hearts to assess the visualisation of perfusates in MRI and their intravascular retention at different time points over a period of 12 hours. Morphological images were acquired and quantitative T_1 maps were generated. Evaluation of image quality was based on SNR and CNR analysis. Intravascular retention was assessed both visually and statistically using a volume of interest approach to analyse significant changes in signal intensity in and around the filled LAD artery, as well as changes in the longitudinal relaxation time (T_1) in adjacent myocardium. Suitability of perfusates for PMMRA was evaluated based on differences in intravascular retention of perfusates in post-mortem vessels, mainly due to the different chemical and physical properties.

This chapter summarises the methods and results published in [48].

5.1 Methods

Based on the results of *in vitro* investigations examining a range of potential perfusate for PMMRA (Chapter 3), three perfusates were selected as suitable. The MR sequence used for visualisation of cardiac vasculature was based on the examinations presented in Chapter 4. Extravasation effects were investigated using a non-pathological *ex situ* porcine heart model.

5.1.1 Samples and experimental protocol

MR examinations were performed using porcine hearts (n=9) from a local slaughterhouse were examined *ex situ* (post-mortem interval $\approx$ 12 hours, age: 120 days old). No discernible cardiac pathologies were visible. Each heart was used for a single experiment. Individually, paraffin oil, Gadovist®-doped physiological solution (2 mmol/l) and PEG 200 were injected into the LAD arteries of *ex situ* porcine hearts. For each perfusate, three repetitions (A, B, C) were performed on separate hearts. Injection was performed by the same person

in each case but the injection pressure was not measured due to the requirement that porcine hearts be kept in the same position in the scanner suite for the entire duration of the examination, meaning the pressure sensor containing metal components could not be employed. As seen in Table 5.1, injection volumes differed between samples. This can be explained by the placement of the catheter used to inject perfusates. In some cases perfusate escaped into the left ventricle, meaning more perfusate had to be injected to fill the LAD artery. The probability of leakage via this mechanism after the artery was filled was minimised by occluding the vessel at its origin in the aorta with a small plastic stopper. A fast, low resolution sequence (acquisition time: 16 seconds) was used to confirm vessel filling prior to commencing the acquisition of images used for analysis in this work.

Table 5.1: Perfusate injection volumes (ml) into the LAD artery of *ex situ* porcine hearts (A, B and C).

Perfusate	$Volume_A$(ml)	$Volume_B$(ml)	$Volume_C$(ml)
Gadovist® solution	2.8	2.8	9.0
Paraffin oil	2.8	5.0	3.0
PEG200	3.8	2.8	3.0

5.1.2 Image acquisition

Details of the scan parameters for image acquisition are found in Table 5.2. For the

Table 5.2: Scan parameters for acquisition of quantitative and morphological MRI data (perfusate extravasation in porcine hearts).

Sequence	Resolution (mm)	Slices	TR (ms)	TE (ms)	FA (°)	BW (Hz/Px)	Additional parameters	TA (min:sec)
3D GRE	0.8×0.8×0.8	192	8	3.4	15	310	–	5:34
2D TIR	0.6×0.6×3	38	10000	9.7	–	200	TI=50, 100, 200, 600, 1300, 2000ms, ETL=8.	14:00

visualisation of filled vessels, isotropic *morphological images* of the entire *ex situ* heart were acquired using a 3D GRE sequence. MR data for quantitative T_1 mapping were acquired using a 2D TIR sequences. Image acquisition timing was according to Figure 5.1. Measurements were performed at room temperature and the temperature of the porcine hearts was monitored during examinations using a real-time fiber optic temperature sensor (Fluoroptic®, LumaSense Technologies Inc, USA). The temperature remained between 23°C and 25°C for each scan session. Between scan sessions, hearts were stored at approximately 22°C.

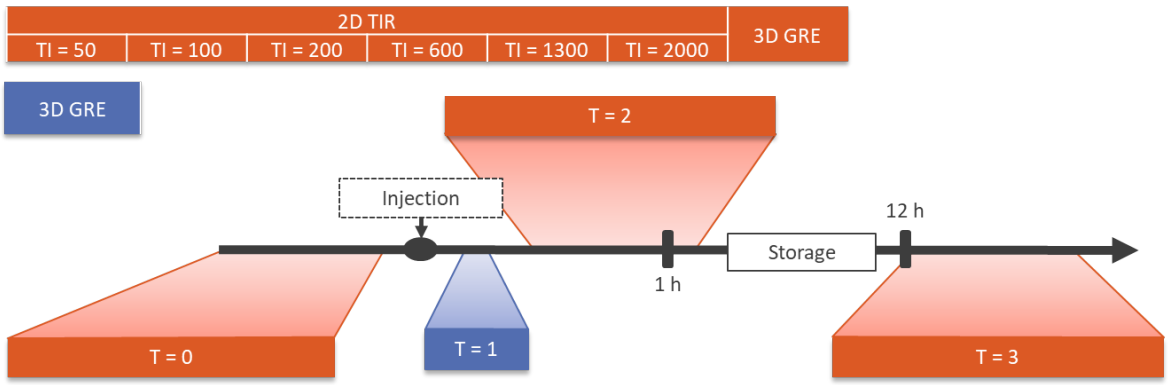

Figure 5.1: Scheme detailing perfusate injection and image acquisition. At T=0, T=2 and T=3 the full image acquisition protocol was completed (orange, acquisition time ≈ 20 min). At T=1 only the reduced acquisition protocol (3D GRE) was completed (blue, acquisition time ≈ 5 min).

5.1.3 Image evaluation

SNR and CNR were used to compare different perfusates in images acquired under the same acquisition conditions. For determination of SNR and CNR according to Eq. 2.1 and Eq. 2.4 post-injection (T=1) morphological images were used. This enabled assessment of image quality and provided a basis for comparison of the investigated perfusates. Morphological images at T=1 ensured a reliable assessment of SNR and CNR prior to the influence of time and the comparison of perfusates under ideal (i.e. immediately following injection) conditions. Selection of a later time point may have negatively biased results due to the fast extravasation of certain perfusates. An example of the placement of ROIs for determination of SNR and CNR is displayed in Figure 5.2.

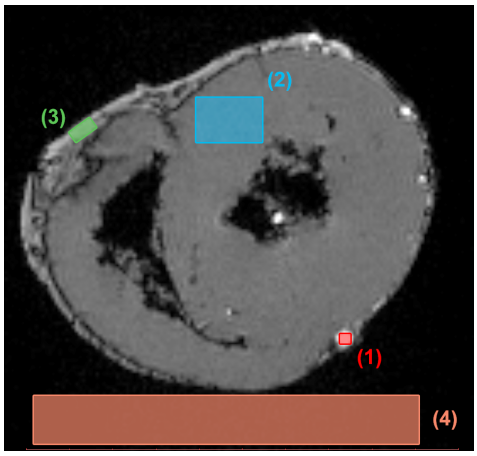

Figure 5.2: Morphological image (3D GRE) displaying ROIs for the calculation of SNR and CNR. 1: perfusate, 2: myocardium, 3: epicardial fat, 4: noise. For orientation the anterior wall of the heart is at the bottom of the image.

5.1.4 Image processing

No image processing or registration was performed on morphological images as there was no change to the field of view (FOV) or movement of the sample between the time points (T=1, T=2) used in the evaluation of SI. T_1 fitting was implemented in Matlab R2016 according to Eq. 2.17. Quantitative T_1 parameter maps at T=3 ($\approx$ 12 hours post-injection) were used to investigate the effects of an extended amount of time. Due to removal from the scanner during this time T_1 maps at T=3 ($\approx$ 12 hours post-injection) were registered to T_1 maps at T=2 ($\approx$ 1 hour post-injection). Image registration performed in Matlab R2016 (*imregister*) was intensity-based.The metric used for registration was based on mattes mutual information which computed the mutual information between the fixed and moving images to be registered [161]. A one-plus-one evolutionary optimizer with a maximum of 500 iterations was used. For more information regarding the applied optimizer, the reader is referred to [162].

5.1.5 Image analysis

VOIs used for image analysis were manually segmented in ITK-SNAP [141] and all further image analysis was implemented in Python [128].

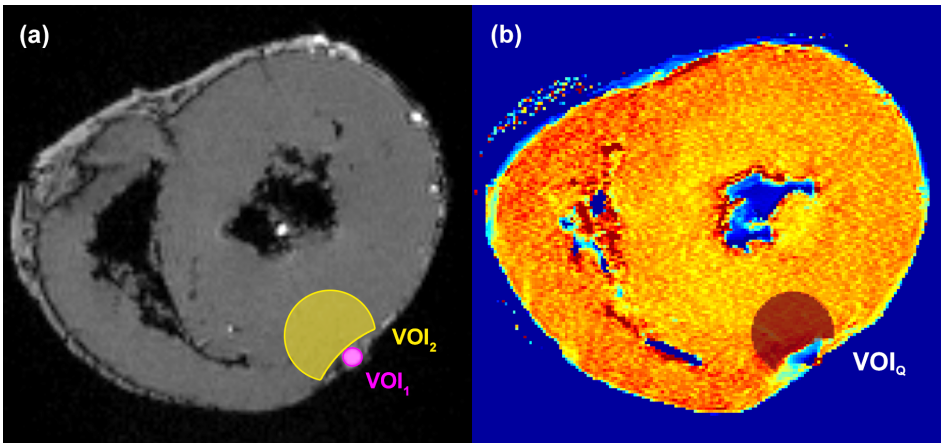

Figure 5.3: (a) Morphological image (3D GRE) displaying VOI for the calculation of signal intensity in the LAD artery (VOI_1) and surrounding myocardium (VOI_2). (b) T_1 map displaying VOI_Q to quantify changes in T_1 in myocardium over 12 hours following injection of perfusate.For orientation the anterior wall of the heart is at the bottom of the image

Analysis of morphological images was based on SI in the defined VOIs. VOIs were placed in a segment of the filled LAD artery (VOI_1) and in adjacent myocardium (VOI_2) in the same slices (Figure 5.3). VOIs were defined in images acquired immediately following injection ($VOI_{1,2,T=1}$) and transferred to images acquired one hour later ($VOI_{1,2,T=2}$). SI values correspond to the brightness of each voxel in an image and are determined by a combination

of tissue-specific properties and the selected MRI sequence parameters. SI values were extracted from VOIs were analysed to identify time-related changes in the LAD artery (VOI_1) and in adjacent myocardium (VOI_2). $VOI_{1,2}$ were not applied to images acquired at T=3, because certain perfusates (e.g. PEG200) extravasated very quickly, preventing reliable visual assessment of the vessels, which may have led to uncertainty or error in the manual segmentation of these VOIs. Therefore, changes in SI ($VOI_{1,2}$) were not assessment between T=2 and T=3. For analysis of T_1 maps the VOI (VOI_Q) was placed in myocardium adjacent to the filled vessel, excluding epicardial fat and the vessel itself. An example of VOI placement is given in Figure 5.3. VOI_Q was defined in native T_1 maps (T=0) and applied to maps at T=2 and T=3.

T_1 values in the VOI were extracted to analyse changes over time. Changes in myocardium were quantified using these values. Histograms of the T_1 relaxation times in VOI_Q at each time point ($VOI_{Q,\ T=0}$, $VOI_{Q,\ T=2}$ and $VOI_{Q,\ T=3}$) were used to assess bulk changes in the T_1 of voxels between these time points.

5.1.6 Statistical analysis

Observed differences in SI (morphological images) and T_1 (quantitative parameter maps) were statistically analysed in more detail. One-way Analysis of Variance (ANOVA) was used to test the hypothesis that no change in the mean SI (or mean T_1) of a given VOI was observed between time points. Analysis comprised entire VOI (multiple slices) and was performed in Python [128]. The null hypothesis, that sample means were equal, was rejected for p-values < 0.05.

5.2 Results

The results corresponding to the visualisation of vascular structures and comparison of CNR of different perfusates are presented in this section. Additionally, intravascular retention was statistically assessed based on changes in signal intensity and T_1 relaxation times in the LAD artery and adjacent myocardium over 12 hours.

5.2.1 Visualisation of vascular structure: SNR and CNR

The distribution of noise in the 3D GRE images was approximated by a Gaussian distribution (Figure 5.4).

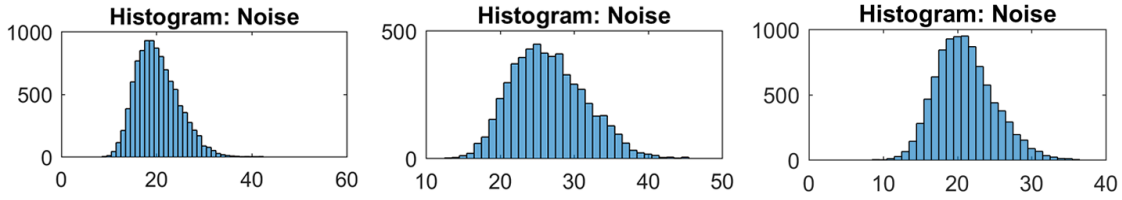

Figure 5.4: Examples of noise distribution in 3D GRE images (morphological images).

In morphological images, all perfusates appeared hyperintense. In a given image, maximal signal intensity was observed in voxels corresponding to the injected perfusate (calculated at T=1). All perfusates demonstrated excellent contrast with surrounding tissue (Figure 5.5). SNR in myocardium (mean ± SD) was 56 ± 4. In epicardial fat, SNR was slightly higher, 73 ± 11. Mean values (± SD) for SNR for each perfusates are displayed in Table 5.3. Of the three investigated perfusates, the Gadovist® solution delivered the highest CNR against both myocardium (183±63) and epicardial fat (161±60) (Table 5.3).

Table 5.3: Mean SNR (± SD) and CNR (± SD) for each set of porcine hearts (A, B, C) at T=1.

Perfusate/Tissue	SNR (mean±SD)	CNR (Myocardium)	CNR (Epicardial fat)
Paraffin Oil	155 ± 34	99 ± 35	86 ± 41
PEG200	109 ± 26	52 ± 19	35 ± 20
Gadovist® solution	237 ± 63	183 ± 63	161 ± 60
Ex vivo myocardium (all samples)	56 ± 4	–	–
Ex vivo epicardial fat (all samples)	73 ±11	–	–

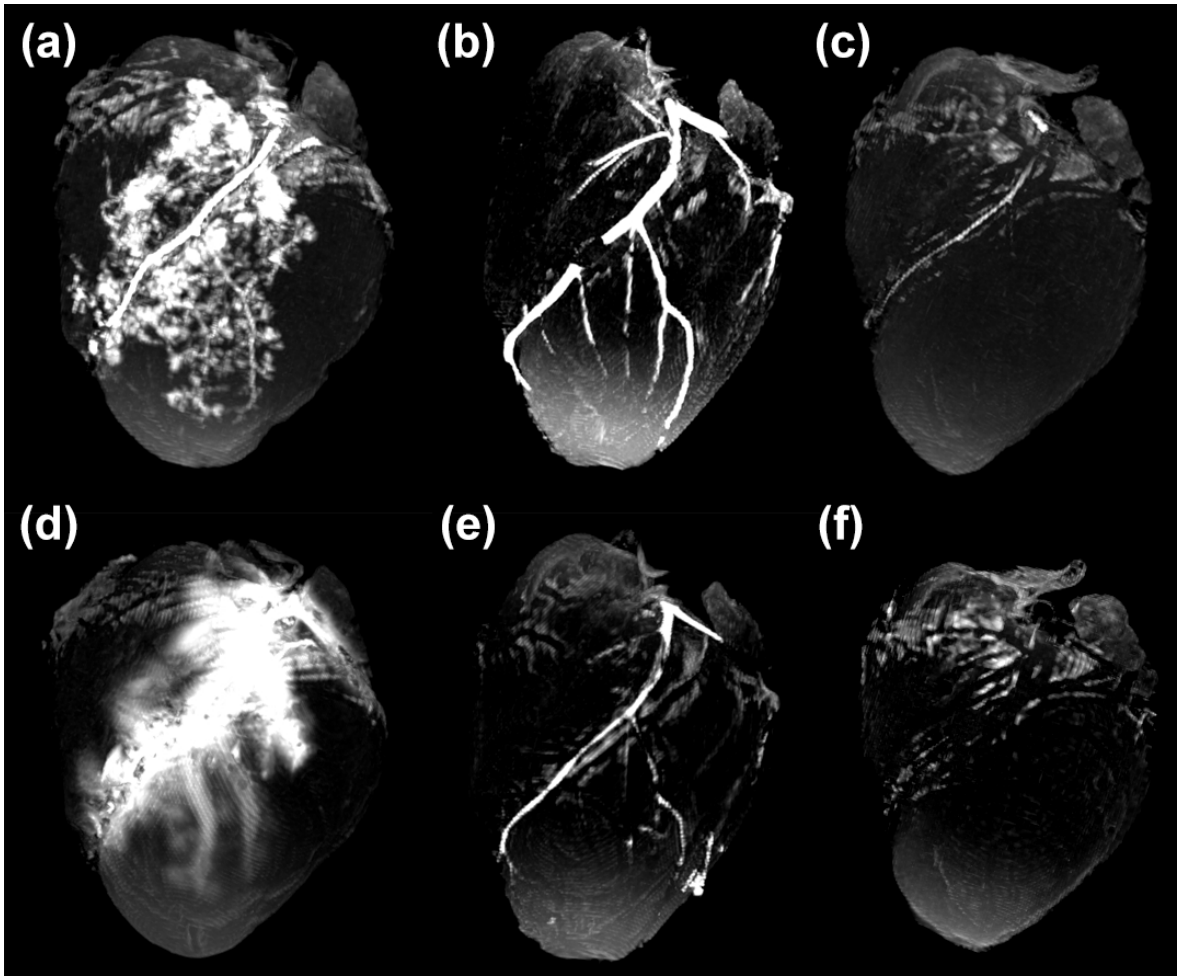

Figure 5.5: Example maximum intensity projections (MIP) of 3D GRE images: Immediately after injection of (a) Gadovist® solution (b) paraffin oil (c) PEG200 and 12 hours after injection of (d) Gadovist® solution (e) paraffin oil (f) PEG200.

5.2.2 Intravascular retention of perfusates in the LAD artery and effect on adjacent myocardium

The time dependent intravascular retention of the investigated perfusates was evident upon visual inspection of the morphological images. This dependence was quantitatively assessed by analysing the SI in morphological images and changes in T_1 values in myocardial tissue adjacent to the filled vessel. The statistical significance of the observed changes in SI and T_1 over 12 hours is summarised by the ANOVA results in Table 5.4.

Table 5.4: P-values from the one-way ANOVA for changes in mean SI in VOI_1 and VOI_2 as well as for changes in mean T_1 values in VOI_Q

Perfusate	VOI_1 (T=1 vs. T=2)	VOI_2 (T=1 vs. T=2)	VOI_Q (T=0 vs. T=2)	VOI_Q (T=2 vs. T=3)
Paraffin oil_A	0.067	0.724	0.056	0.227
Paraffin oil_B	0.016	0.066	0.765	0.763
Paraffin oil_C	0.116	0.070	0.637	0.780
$PEG200_A$	$\ll$0.001	$\ll$0.001	0.568	0.826
$PEG200_B$	$\ll$0.001	0.040	0.812	0.001
$PEG200_C$	$\ll$0.001	$\ll$0.001	0.333	0.008
Gadovist® $solution_A$	0.297	$\ll$0.001	$\ll$0.001	$\ll$0.001
Gadovist® $solution_B$	0.036	$\ll$0.001	$\ll$0.001	$\ll$0.001
Gadovist® $solution_C$	$\ll$0.001	$\ll$0.001	$\ll$0.001	$\ll$0.001

Changes in signal intensity in the LAD artery and adjacent myocardium during the first hour after injection

Figure 5.6 demonstrates that the SI of paraffin oil in the LAD artery only minimally decreased within the first hour after injection. ANOVA of VOI_1 (Figure 5.4) indicated that this change was only statistically significant in one case (paraffin oil_B). In porcine hearts injected with PEG200 a decrease in SI was observed for all samples. This corresponded to visual observations, which indicated the disappearance of PEG200 within the first hour. Changes in SI in these samples were all found to be statistically significant. For Gadovist® filled arteries, statistically significant increases and decreases in SI were observed during the first hour.

The same analysis was also performed for VOI_2, placed in adjacent myocardium. Following ANOVA no evidence of statistically different mean SI values was observed for paraffin oil within the first hour after injection. In PEG200 samples minimal differences over time were seen in all samples. ANOVA additionally found all these differences to be statistically significant. All Gadovist® samples demonstrated an increase in SI within the first hour following injection. The statistical significance of these observations is also supported by the results in Table 5.4.

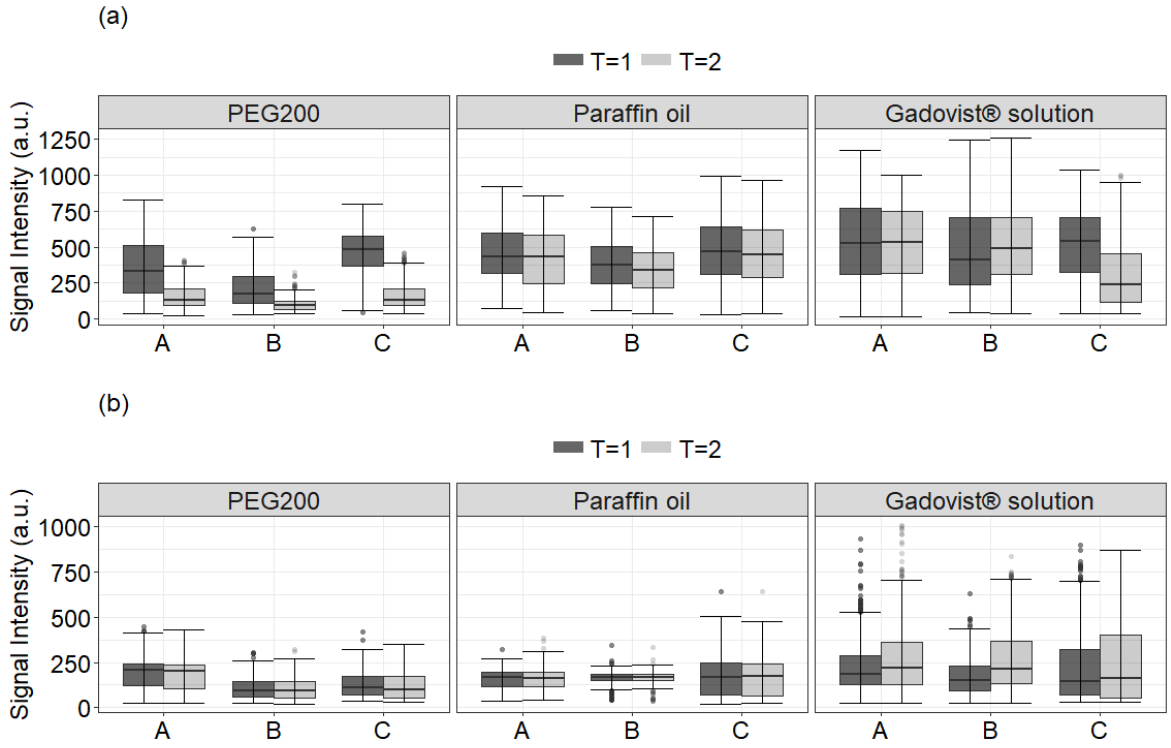

Figure 5.6: Boxplots representing signal intensity (SI) in (a) left anterior descending (LAD) artery (VOI_1) immediately following injection (T=1) and one hour after injection (T=2) and in (b) myocardium adjacent to the filled LAD (VOI_2) immediately following injection (T=1) and one hour after injection (T=2). A, B and C represent the three repetitions.

Changes in T_1 of adjacent myocardium during the first 12 hours after injection

To characterise changes in myocardium adjacent to filled vessels in more detail, T_1 maps were analysed at three time points. Figure 5.7 shows the distribution of T_1 values corresponding to VOI_Q at each of the measured time points. While T_1 remained constant for most voxels where paraffin oil or PEG200 were injected, the distribution of T_1 values distinctly moved to the left following injection of the Gadovist® solution, indicating a shortening of myocardial T_1. ANOVA between T_1 values at T=0 (prior to injection) and T=2 ($\approx$ 1 hour post-injection) indicated no evidence of statistically significant changes in mean T_1 values in myocardium for samples where paraffin oil and PEG200 were injected. Within the same timeframe, all samples containing the Gadovist® solution displayed statistically significant changes in T_1. Between data acquired at T=2 and T=3 ($\approx$ 12 hours post-injection), samples with Gadovist® solution as well as two additional PEG200 samples revealed statistically significant changes in the T_1 values in myocardium adjacent to the filled LAD artery.

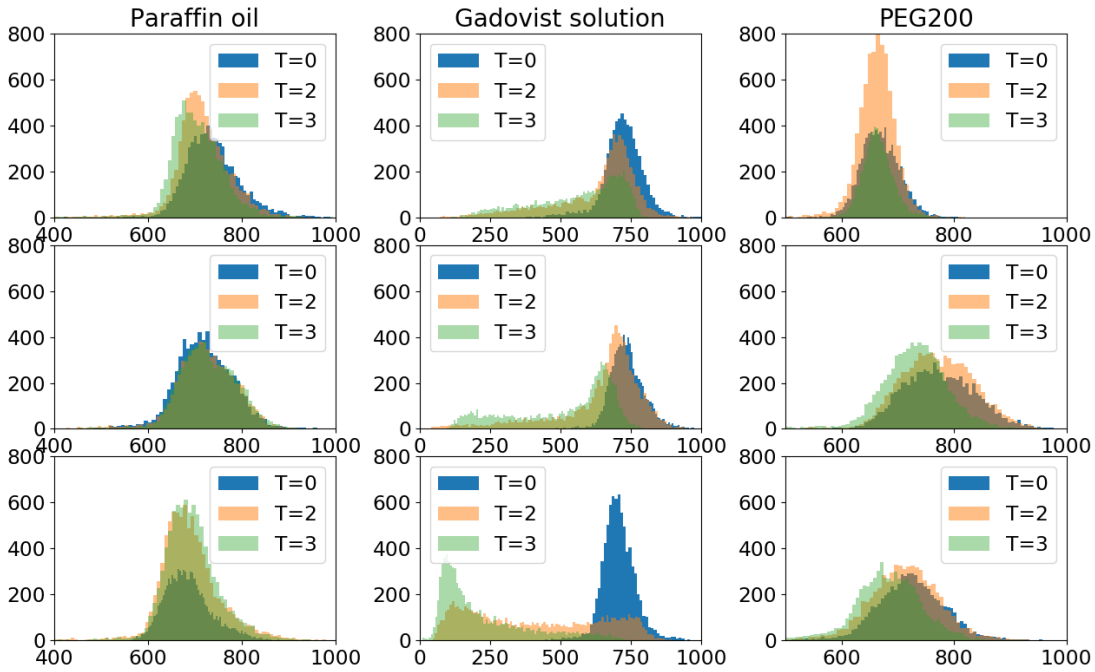

Figure 5.7: Histogram (bins = 100) of T_1 values (A,B,C) in myocardium adjacent to the left anterior descending artery (LAD) prior to perfusate injection (T=0), one (T=2) and 12 hours (T=3) later. The vertical axis corresponds to samples A, B, C.

6 Detection of myocardial infarction in *ex situ* porcine hearts using MRI at 3T

Contrary to the investigations related to the development of PMMRA which have been described so far in this work, this chapter presents the examination of a broader range of MR contrast and quantification mechanisms. In particular quantitative parametric mapping approaches including relaxometry and diffusion tensor imaging were applied in cardiac post-mortem MRI examinations. Using an animal model, this pilot study characterised alterations in post-mortem myocardium due to induced MI using a VOI-based analysis approach. Evaluation of different quantitative MRI parameters potentially relevant in the detection of early acute MI was supported by statistical analysis of the corresponding values from both the suspected infarct region and a remote region of the myocardium.

6.1 Methods

The section describes the methods applied for MRI tissue characterisation of *ex vivo* porcine hearts following induced myocardial infarct with very short survival times ($<$ 30 minutes) to detect possible changes in the relaxation and diffusion properties of post-mortem porcine myocardium.

6.1.1 Ethical considerations

Animal experiments were conducted in cooperation with the Department of Cardiology (Medical University of Graz) under BMWFW-66.010/0100-WF/V/3b/2016, approved by the Austrian Federal Ministry of Education, Science and Research. Swine were placed under anaesthesia using a combination of ketamine, dormicum, pancuronium and fentanyl. Experimental procedures prior to the induction of myocardial infarction included electrophysiology catheter examinations in the endocardium and endocardial multi-electrode array measurements, which were performed for a duration of approximately 8-10 hours.

6.1.2 Samples and experimental protocol

Myocardial infarction was induced in swine (n=11, *Suus domesticus*) by injection of ethanol (10-20 ml) into the proximal segment of the LAD artery by means of coronary catheterisation via the right femoral artery. Coronary occlusion led to acute cardiogenic shock in the animals which resulted in cardiac arrest after approximately 10-30 minutes. Hearts were then excised and prepared for examination in MRI.

In three animals anomalies with the potential to influence experimental results were observed. These animals were therefore excluded from the statistical analyses performed in this study.

1. Iatrogenic infarct (without injection of ethanol, survival time = 60 minutes)
2. Ethanol injected into Left Circumflex (LCX) coronary artery (MI, posterior)
3. Injection of potassium chloride to induce euthanasia

MRI examinations on *ex situ* porcine hearts were commenced within two hours of death. This time delay was necessary to enable heart explantation, transport to the scanner and completion of the experimental set-up, including allowing hearts to equilibrate to room temperature. The experimental set-up consisted of a glass vase filled with flour. The *ex situ* porcine heart was wrapped in plastic and placed in the vase. Hearts were surrounded by flour up to approximately the aorta level to further stabilise the set-up. An example of the experimental set-up can be found in Figure 6.1.

Figure 6.1: Example of experimental setup for MRI examination of *ex situ* porcine hearts. Flour was used to stabilise hearts for the duration of the examination.

6.1.3 Image acquisition

All MRI examinations were performed at room temperature (23-25°C). Hearts were allowed to equilibrate to this temperature prior to measurement. The temperature of hearts was measured using a real-time fiber optic temperature sensor (Fluoroptic®, LumaSense Technologies Inc, USA). The temperature remained between 23°C and 25°C for the duration of each scan session. Imaging parameters for the acquisition of quantitative MR data are detailed in Table 6.1. For the acquisition of DTI data, two 2D EPI sequences were used (Table 6.1).

Table 6.1: Scan parameters for acquisition of quantitative MRI data in *ex vivo* porcine hearts following induced MI.

Sequence	Resolution (mm)	Slices	TR (ms)	TE (ms)	FA (°)	BW (Hz/Px)	Additional parameters
2D TIR	0.6×0.6×3	40	10000	9.7	–	200	TI = 50, 100, 200, 600, 1300, 2000 ms
2D MSE	0.6×0.6×3	40	7050	10.6	–	200	16 equally spaced echoes
2D EPI_A	1.5×1.5×3.6	40	7800	105	90	1500	b=0, 500, 1000, dir=20, EPI factor = 63
2D EPI_B	1.5×1.5×1.5	69	3500	111	78	1540	b=0, 500, 1000, 2000, dir=64, EPI factor = 53, multi-band factor = 3

6.1.4 Evaluation of acquired data

Signal and noise masks was generated via automatic masking of each *ex situ* porcine heart using median filter smoothing based on an automatic histogram thresholding technique (Otsu) [131] as described in Chapter 2. An example of segmented signal and noise masks is given in Figure 6.2. These masks were then used to determine SNR according to Eq. 2.1. SNR was determined for each inversion time (TIR) and echo time (MSE), as well as for DTI data using the images acquired with b=0. Histograms corresponding to the extracted image background were used to examine the distribution of image noise. The two 2D EPI sequences applied for DTI were compared in terms of SNR and distribution of the fitted FA and MD values.

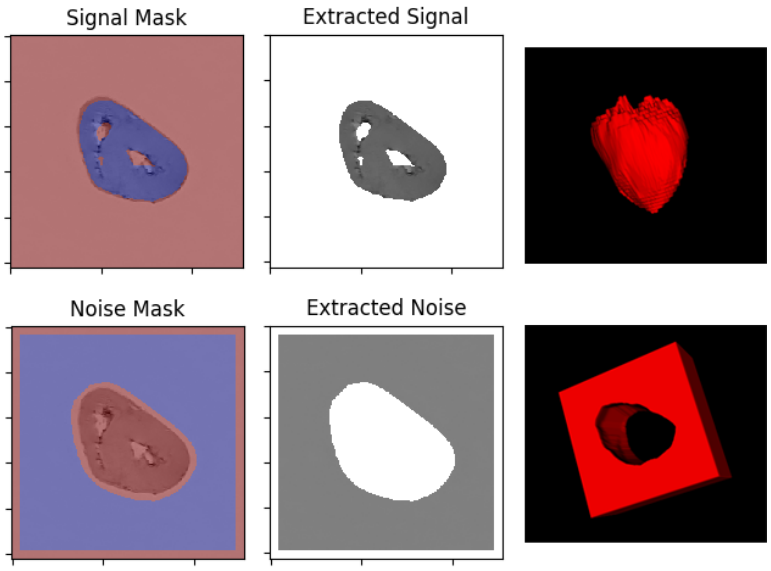

Figure 6.2: Signal and noise masks with corresponding extracted data volumes (slice-wise (left, middle) and as a segmented 3D volume (right)) for a single porcine heart. Segmentation based on 2D TIR data (TI = 100 ms).

6.1.5 Image processing

Blockwise NLM denoising was applied to acquired data as described in Section 2.3. For diffusion weighted images denoising was performed in the diffusion weighted space to improve SNR prior to tensor reconstruction. The patch radius (PR) and block radius (BR), which determine the patch and block size for blockwise NLM denoising were varied to determine appropriate values each sequence type prior denoising. Results were visually assessed by comparison of original, denoised and difference images, general examples of which can be found along with the description of the NLM denoising algorithm in Section 2.3 (Figure 2.2 and 2.2). Following denoising, data were extracted using the aforementioned signal mask (Figure 6.2). Parameter fitting of T_1, T_2, fractional anisotropy (FA) and mean diffusivity (MD) was performed according to Section 2.3. Representative parameter fits for T_1 and T_2 are displayed in Figure 6.3. The effect of denoising on the resulting T_1 and T_2 parameter fits was examined by comparison of the mean and standard deviation of values in VOIs for original and denoised data.

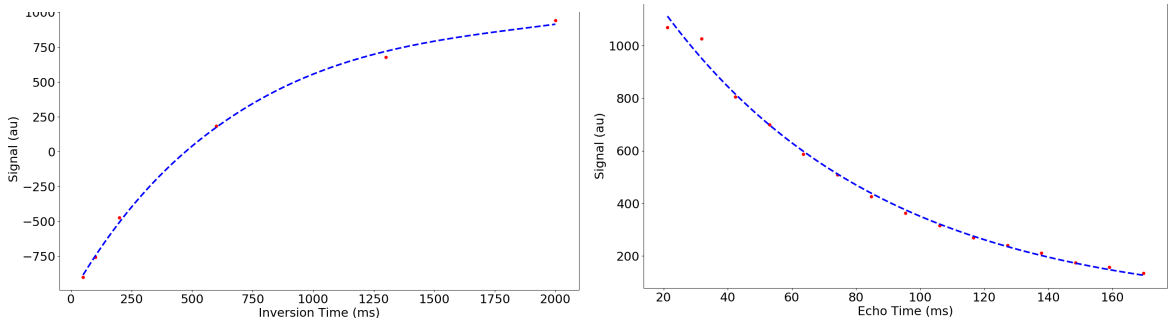

(a) T_1 fit (*ex vivo* myocardium) (b) T_2 fit (*ex vivo* myocardium)

Figure 6.3: Examples of parameter fitting

Due to the *ex vivo* circumstances and the fact that the porcine hearts were not moved within a single scan session, no registration was performed for TIR and MSE data as these were acquired with the same spatial resolution, slice thickness and number of slices. 2D EPI data used for DTI was acquired with a different acquisition matrix. Therefore, the resulting parameter maps (FA, MD) were registered to 2D TIR (TI = 1300 ms) images to enable the reliable VOI-based analysis. Image registration was achieved with SimpleElastix [152]. SimpleElastix is a multi-lingual library for registration of medical images which offers Python implementation of elastix algorithms [152]. Elastix is an open-source collection of robust algorithms, which enables intensity-based registration with numerous applications in image registration literature [163]. These algorithms permit the spatial alignment of a *moving image* $I_m(x)$ into the coordinate space of a *fixed image* $I_F(x)$ by finding the coordinate transformation $T(x)$ which spatially aligns $I_M(T(x))$ with $I_F(x)$ [163]. Viewed as an optimisation problem, the cost function $C(T_\mu; I_F, I_M)$ is minimised with respect to the defined parameters μ (Eq. 6.1, [163]).

$$\hat{\mu} = \arg\min_{\mu} C(T_\mu; I_F, I_M) \tag{6.1}$$

Using adaptive step sizes and the advanced mattes mutual information metric, FA and MD maps were registered to the image space of T_1 parameter maps.

6.1.6 Image and statistical analysis

To quantify differences between infarcted and non-pathological tissue, quantitative parameter maps were analysed using a VOI-based approach. Two voxels-of-interest were defined for analysis of imaging data. Each VOI covered 3 slices, contained 507 voxels and was drawn based on T_1 maps. $VOI_{infarct}$ was positioned to correspond to the suspected infarct region and VOI_{remote} to a remote region of myocardium. The $VOI_{infarct}$ was defined based on the expected position of the infarct due to occlusion of the LAD, visual appearance of the

heart directly after vessel occlusion and the T_1 map used for VOI definition. The remote VOI corresponded to a section of the posterior wall of the heart. Based on the standard allocation of myocardial segments to coronary arteries, this region was expected to be only minimally or not affected by the occluded LAD. Voxel values corresponding to each VOI were extracted for statistical analysis.

Data values were classified as outliers if they were more than 1.5*IQR larger than the 3rd quartile or more than 1.5*IQR smaller than 1st quartile. Outliers were removed prior to statistical analysis. Exploratory statistical analysis of the data extracted from parameter maps was undertaken in a sample-wise manner to probe data and visualise inter-sample (i.e. between hearts) variation for each of the VOIs. Thereafter, values corresponding to the mean value in each VOI/heart were use for further comparison and statistical analysis. For each parameter (T_1, T_2, FA, MD), the assumption of normality was separately tested for each VOI by applying the Shapiro-Wilk test for normality ($\alpha = 0.05$). The equality of sample variance was tested for using Bartlett's sample homogeneity test ($\alpha = 0.05$). Finally, the Student's t-test was applied to test the hypothesis (H_0) that mean parameter values (T_1, T_2, FA and MD) in $VOI_{infarct}$ and VOI_{remote} were equal against the hypothesis (H_1) that these values were not equal ($\alpha = 0.05$).

6.1.7 Macroscopic and histological analysis

Macroscopic examination of the porcine hearts was performed in a non-blinded manner within 48 hours of the MRI examination. During the examination, performed by a board-certified forensic pathologist, all findings were photographically and descriptively documented. Hearts were sliced along the short axis to correspond to images obtained in MRI. Slice thickness was approximately 10 mm. Commencing at the apex, between 8-11 slices were obtained for each sample (Figure 6.4).

Following macroscopic examination and documentation, hearts were fixed in 10 % neutral-buffered formalin solution. Sampling for histological analysis was undertaken by a clinical pathologist together with the board-certified forensic pathologist who performed the macroscopic examination. The sampling strategy was based on the expected location of the infarct due to complete occlusion of the LAD, macroscopic observations directly prior to explantation of the heart and findings during post-mortem macroscopic examinations.

There is significant overlap in anatomical features between porcine and human hearts [164]. Therefore, remote histology samples were obtained based on the allocation of myocardial segments to coronary arteries in human hearts. According to the American Heart Association as well as recent literature, occlusion of the LAD is least likely to affect the posterior wall of

the heart (Segments 4 and 5 [165]). Therefore, remote histology samples were taken from this region. Infarct and remote samples were taken from the dissected slice at the upper mid-cavity level (Figure 6.4). Hematoxylin and eosin staining (H&E) was performed for all samples by the internal laboratory of the Institute of Pathology (Medical University of Graz). Interpretation of the stained samples was completed by a clinical pathologist. Examples were photo documented and findings were descriptively reported.

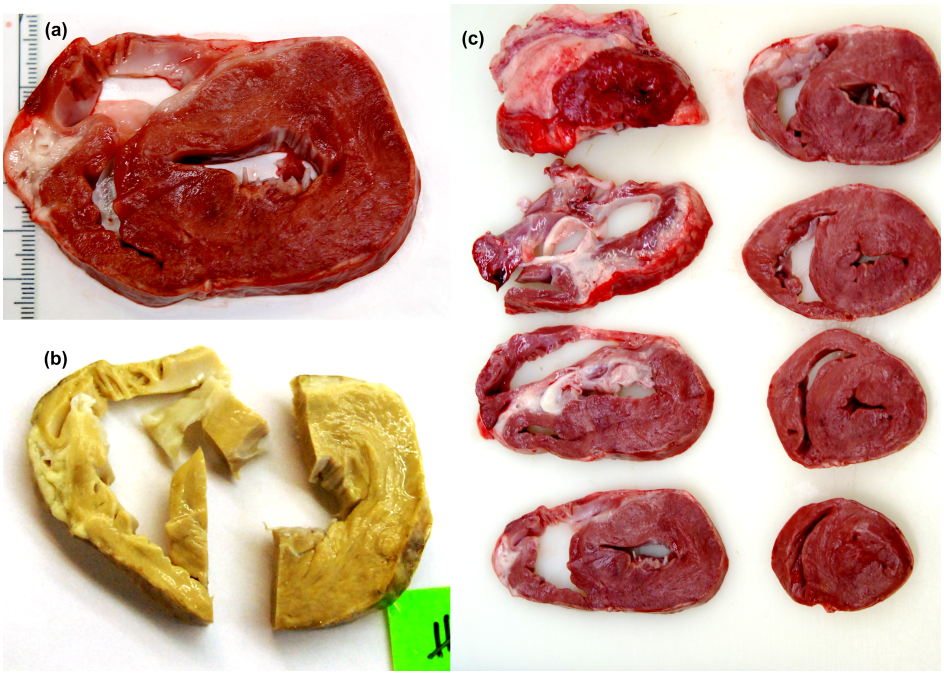

Figure 6.4: (a) Individual short axis slice (prior to formalin fixation) (b) Same short axis slice (post formalin fixation) (c) Overview photo of all short axis slices from one porcine heart.

6.2 Results

Through analysis of quantitative parameters maps, *ex vivo* porcine myocardium the longitudinal and transverse relaxation as well as fractional anisotropy and mean diffusivity the tissue was characterised at a known temperature. VOI-based analysis enabled the determination of these parameters in both myocardium in a region of induced early acute myocardial infarct as well as in a remote region. Statistical image analysis quantified significance of differences in mean values of each parameter between these regions in *ex vivo* porcine myocardium.

6.2.1 Image evaluation and processing

Signal-to-noise ratio

Image noise was approximately Gaussian for the (real) TIR images and approximately Rician for the MSE images (Figure 6.5).

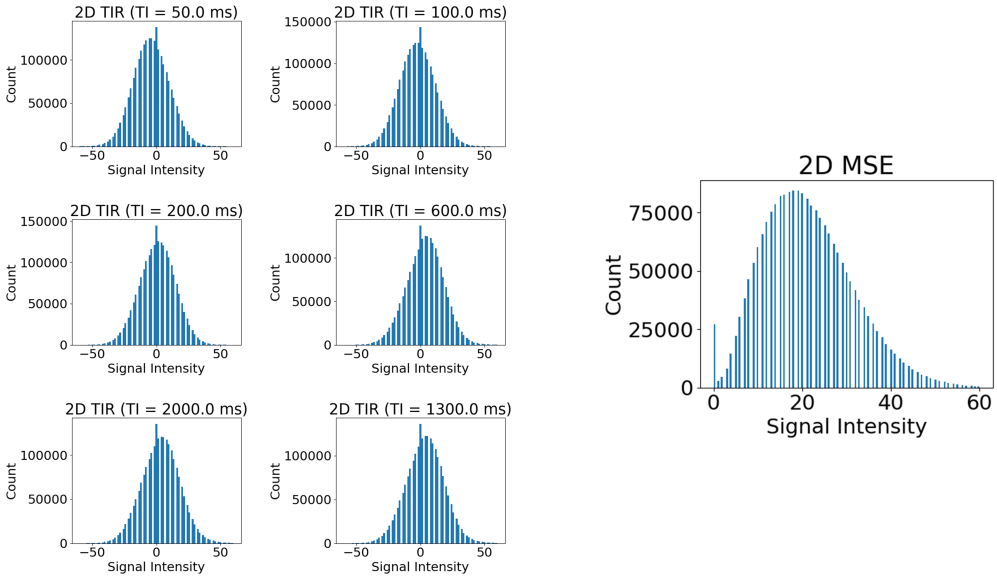

Figure 6.5: Examples of noise distribution in 2D TIR images (TI = 50 to 2000 ms) (left) and in a 2D MSE images (right).

2D TIR images displayed SNR between 10-455 over all inversion times and all samples (Figure 6.6). In 2D MSE images SNR ranged between 38-286 across all echo times and all samples (Figure 6.6). SNR was acceptable for parameter fitting purposes. The SNR in EPI_A images (b=0) was 53 $\pm$ 9 and in images acquired with EPI_B 133 $\pm$ 22. This level of SNR was acceptable for the derivation of measures of parameters such as FA and MD [166].

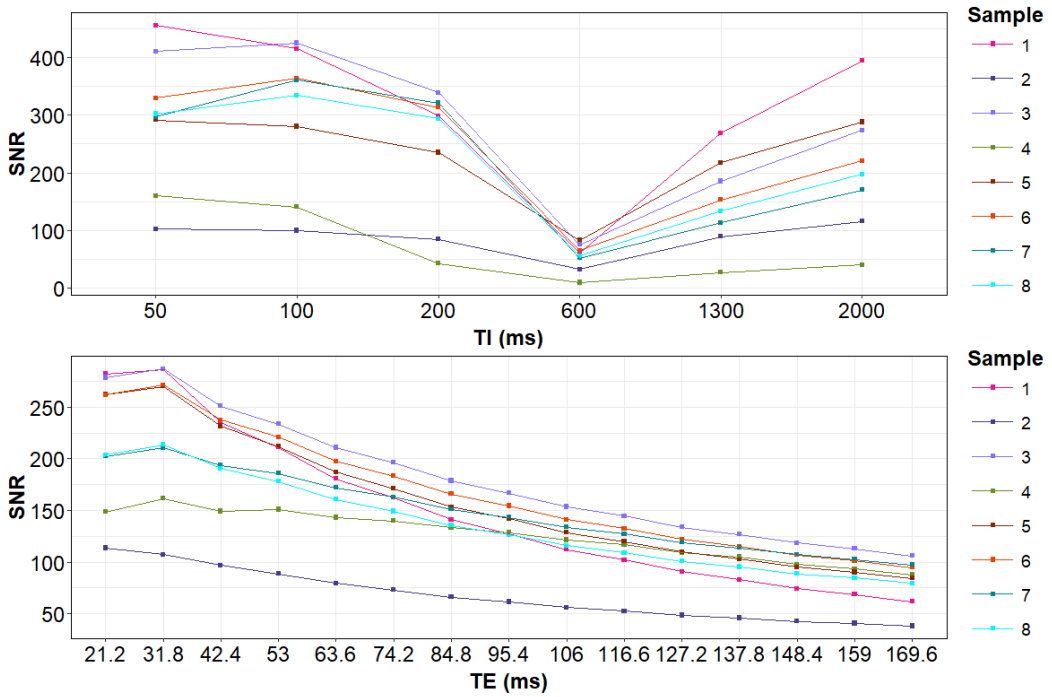

Figure 6.6: SNR in *ex vivo* porcine hearts for 2D TIR data (top) at each inversion time and 2D MSE data (bottom) at each echo time.

Denoising

NL means denoising was applied to TIR and MSE data prior to other image processing steps as described in Section 2.3. Mean T_1 and T_2 did not differ between parameter maps generated with or without NLM denoising, indicating it did not effect the accuracy of the maps. Conversely, the standard deviation of T_1 and T_2 in VOIs was reduced by approximately 40% in parameter maps generated from NLM denoised. The visual effect of denoising is demonstrated for a T_1 map in Figure 6.7.

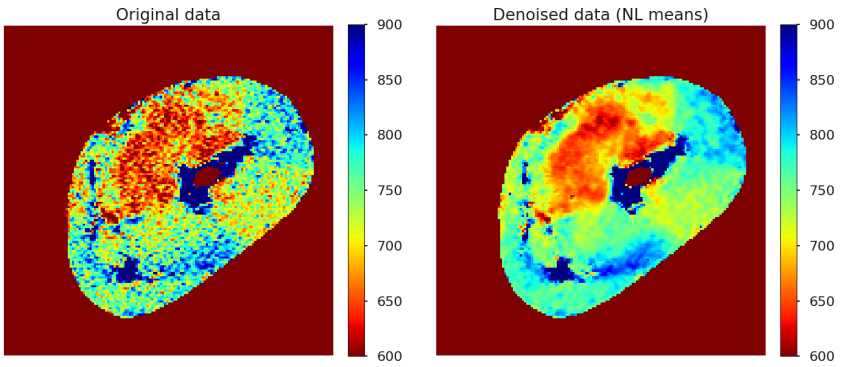

Figure 6.7: Effects of blockwise NLM denoising on T_1 mapping. Original image (left) and denoised image (right).

Figure 6.8 demonstrates an example of the effects of patch (PR) and block radius (BR) on EPI_A for a single porcine heart. From the second row in Figure 6.8 it can be seen that the combination of larger PR and BR led to significant smoothing in the image (last column, Figure 6.8), potentially causing an undesired loss of structural detail. Selected parameters for blockwise NLM denoising in this case were PR=0.5 and BR = 1. The plotted intensity profile (last row, Figure 6.8) demonstrates that the mean amount of noise removed using these parameters was approximately constant and close to zero across the entire image. Furthermore, visual oversmoothing was not observed in the denoised image (PR:0.5, BR: 1).

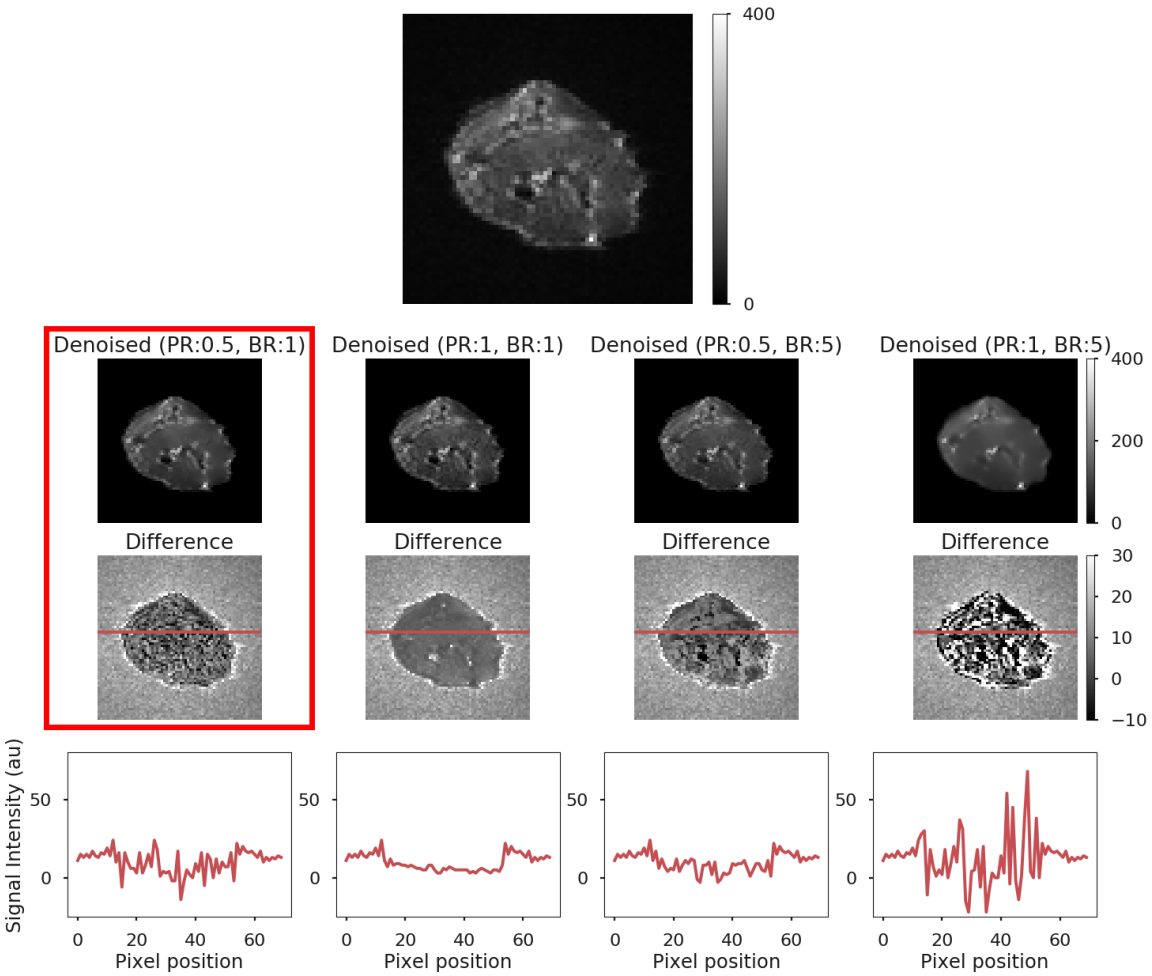

Figure 6.8: Original (left) and denoised 2D EPI data. Denoised images (top row), difference images (middle row) and intensity profiles (bottom row) are shown to demonstrate the effects of varying patch and block radius. Intensity profiles correspond to the red line marked on the difference images.

6.2.2 Exploratory sample-wise analysis

Exploratory sample-wise analysis of quantitative parameter maps revealed differences between the $VOI_{infarct}$ and VOI_{remote} in individual porcine hearts. For example boxplots of the T_1 values (Figure 6.9) demonstrate in many samples a decreased in T_1 was observed in the infarcted region compared to the remote region.

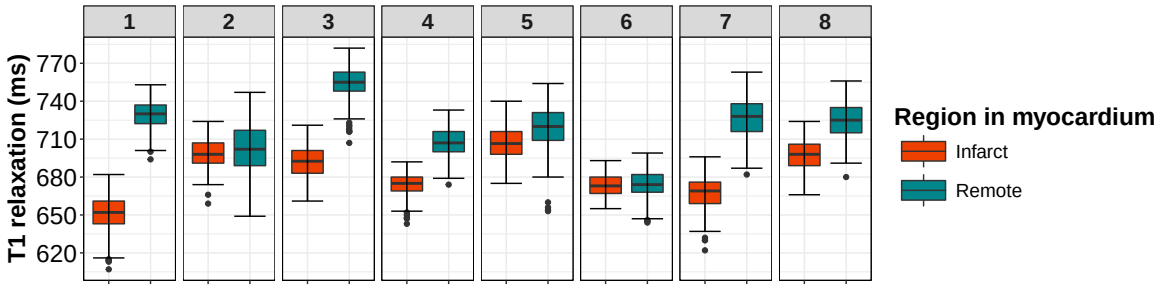

Figure 6.9: Exploratory analysis showing boxplots of the T_1 relaxation times in $VOI_{infarct}$ and VOI_{remote} of individual porcine hearts.

These differences are visible in the parameter maps presented in Figure 6.10, where decreased T_1 and T_2 in the myocardial tissue adjacent to the occluded LAD is visualised.

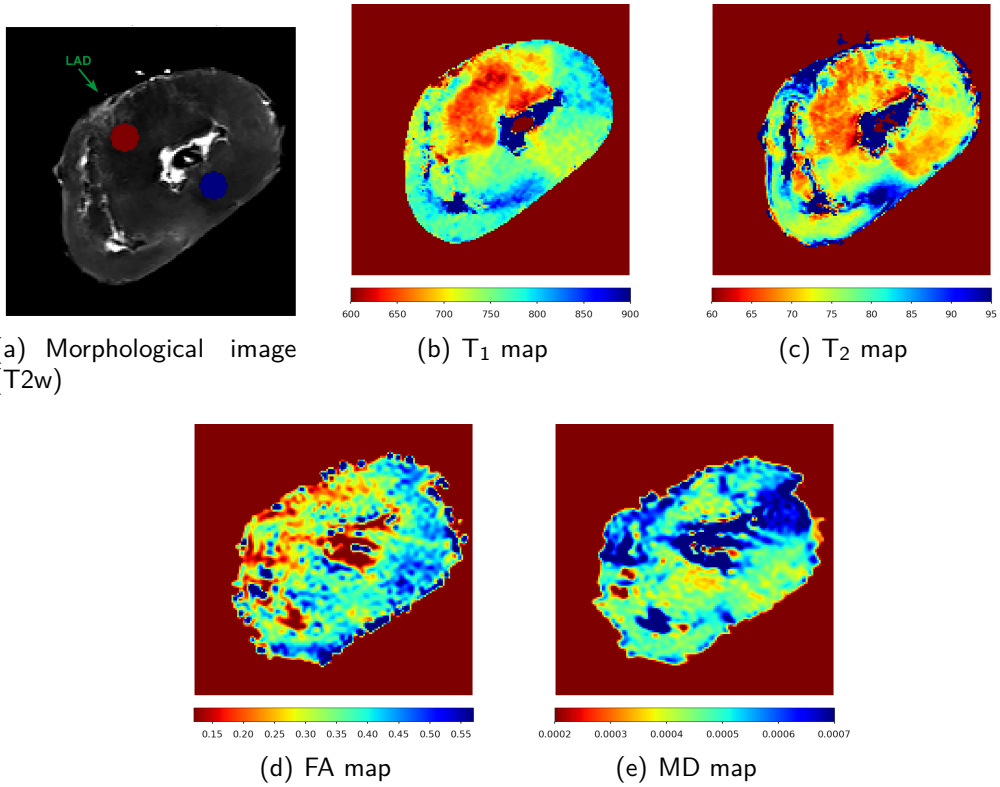

(a) Morphological image (T2w)

(b) T_1 map

(c) T_2 map

(d) FA map

(e) MD map

Figure 6.10: Quantitative parameter maps. Segmentations displayed in a morphological image (T2w, TE=137.2 ms) (a) correspond to $VOI_{infarct}$ (red) and VOI_{remote} (blue). The displayed FA and MD maps (d-e) were generated from data acquired with EPI_A.

6.2.3 Comparison of 2D EPI sequences

The FA and MD values obtained with each 2D EPI sequence were comparable. Histograms of the voxel values across all samples, separated by VOI, indicated that EPI_B led to a broader distribution of FA and MD values. This visual observation was also supported by the standard deviation of the data (Table 6.2). Visual comparison of the acquired data indicated that both sets of images suffered from the typical artifacts of the EPI sequence. Images acquired with EPI_B appeared to suffer less distortion in the presence of high-signal voxels compared to those acquired with EPI_A. Regarding the FA and MD parameter maps, both maps displayed better visual image quality when EPI_A data was used for tensor estimation.

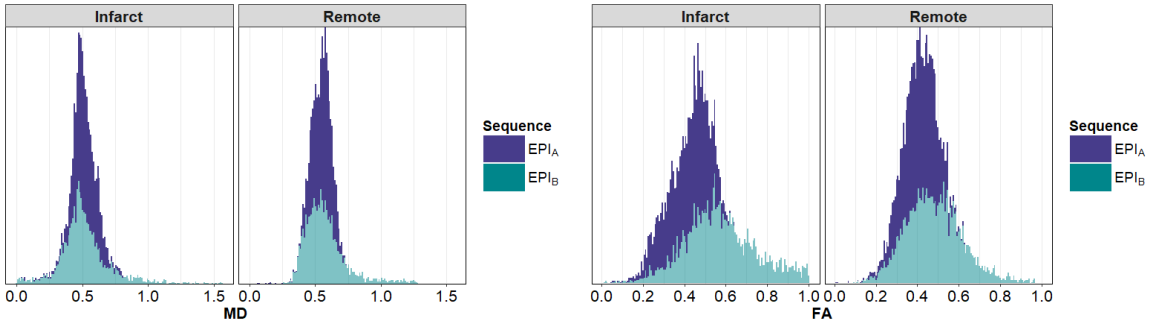

Figure 6.11: FA and MD values from $VOI_{infarct}$ and VOI_{remote} across all samples. 2D EPI data acquired with two different sequences (EPI_A and EPI_B).

6.2.4 Statistical analysis

Analysis across all samples confirmed the trends observed in individual porcine hearts, namely that a decrease in T_1 and T_2 values occured in the infarcted region in *ex vivo* porcine myocardium. Slight differences in the FA and MD were observed between $VOI_{infarct}$ and VOI_{remote}. Fractional anisotropy increased slightly in the infarcted region and mean diffusivity values also decreased. These observations are presented in Figure 6.12. Corresponding mean values and standard deviations for all parameters for all hearts are found in Table 6.2.

The assumption of a normal distribution of data tested individually in each VOI and for each parameter using the Shapiro-Wilk test. H_0 corresponded to the assumption of normality. The p-values obtained were > 0.05 except MD ($VOI_{infarct}$). This indicated there was no evidence to reject H_0 for the majority of parameters. Therefore, the assumption of normally distributed data was considered fulfilled for all parameters except MD ($VOI_{infarct}$). The results of the Shapiro-Wilk statistical tests are shown in Table 6.3.

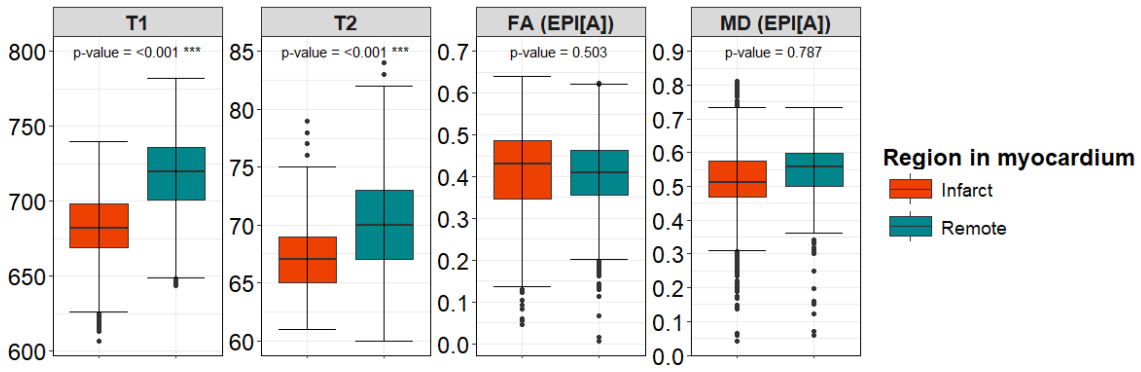

Figure 6.12: Boxplots of parameter voxel values (T_1, T_2, FA_{EPI_A}, MD_{EPI_A}) in porcine hearts (n=8) in the region of suspected myocardial infarct ($VOI_{infarct}$) and the remote region (VOI_{remote}).

Table 6.2: Mean and standard deviation of T_1, T_2, FA and MD values in $VOI_{infarct}$ and VOI_{remote}. T_1 and T_2 values are given in ms and mean diffusivity in 10^{-3} $mm^2.s^{-1}$.

Parameter	$VOI_{infarct}$ (Denoised)	VOI_{remote} (Denoised)
T_1	683 ± 21	718 ± 26
T_2	67 ± 3	70 ± 4
FA_{EPI_A}	0.42 ± 0.10	0.41 ±0.08
FA_{EPI_B}	0.58 ± 0.20	0.48 ± 0.14
MD_{EPI_A}	0.52 ± 0.09	0.55 ± 0.07
MD_{EPI_B}	0.52± 0.19	0.58± 0.16

Table 6.3: Results of Shapiro-Wilk statistical test to determine if sample originated from a normal distribution. $\alpha = 0.05$ and H_0 was rejected for p-values $< \alpha$.

Parameter	VOI	Shapiro-Wilk p-value	Interpretation
T_1	Infarct	0.636	H_0 (normality) cannot be rejected
	Remote	0.818	H_0 (normality) cannot be rejected
T_2	Infarct	0.941	H_0 (normality) cannot be rejected
	Remote	0.347	H_0 (normality) cannot be rejected
FA	Infarct	0.181	H_0 (normality) cannot be rejected
	Remote	0.444	H_0 (normality) cannot be rejected
MD	Infarct	0.022	H_0 (normality) can be rejected
	Remote	0.962	H_0 (normality) cannot be rejected

For a given parameter, Barlett's test of sample homogeneity tested the equality of sample variances for two VOIs. P-values $\ll 0.0001$ were obtained, indicating evidence against H_0. The assumption of equal sample variances was therefore not fulfilled. The results of the Bartlett statistical tests are displayed in Table 6.4. The Student's t-test which accounted for lack of sample variance equality (Welch estimation of degrees of freedom) was applied for each parameter separately to test the equality of sample means between $VOI_{infarct}$ and

VOI_{remote}. Significant evidence of inequality of mean T_1, T_2, while for MD and FA values between the VOIs no evidence supporting rejection of H_0 was observed. Results are displayed in Table 6.5.

Table 6.4: Results of Bartlett's statistical test to determine sample variance equality. $VOI_{infarct}$ compared with VOI_{remote}. $\alpha = 0.05$ and H_0 was rejected for p-values $< \alpha$.

Parameter	Bartlett p-value	Interpretation
T_1	$\ll 0.0001$	H_0 (equal variance) can be rejected
T_2	$\ll 0.0001$	H_0 (equal variance) can be rejected
FA	$\ll 0.0001$	H_0 (equal variance) can be rejected
MD	$\ll 0.0001$	H_0 (equal variance) can be rejected

Table 6.5: Results of Student's t-test (Welch) testing equality of parameter value means in $VOI_{infarct}$ and VOI_{remote}. $\alpha = 0.05$ and H_0 was rejected for p-values $< \alpha$.

Parameter	Student's t-test (Welch) p-value	Interpretation
T_1	$\ll 0.0001$	H_0 (equal mean values) can be rejected
T_2	$\ll 0.0001$	H_0 (equal mean values) can be rejected
FA	0.503	H_0 (equal mean values) cannot be rejected
MD	0.787	H_0 (equal mean values) cannot be rejected

6.2.5 Macroscopic and histology analysis

The comprehensive non-blinded macroscopic examination of porcine hearts, did not identify any findings specific to or indicative of acute ischaemia or infarct. In one single heart (7) subepicardial bleeding and small signs of localised haemorrhage in the apex and valve regions of the septum were observed. Findings are summarised in Table 6.6. H&E staining of the histology samples obtained from the suspected infarct region and a remote region did not yield any findings specific to acute myocardial ischaemia or infarct. Initial signs of cardiac myocyte damage and localised infiltration of inflammatory and neutrophil granulocytes, primarily in epicardium or along the transition epicardium-myocardium were observed. All findings are summarised in Table 6.7. Unless specifically noted, findings were observed in both the suspected infarct region and the remote region. Example images of these findings are presented in Figure 6.13.

Table 6.6: Summary of macroscopic findings.

	Macroscopic findings
1	No localised, focal changes in myocardium. No pallor, haemorrhage or yellow-tan discolouration.
2	No localised, focal changes in myocardium. No pallor, haemorrhage or yellow-tan discolouration.
3	No localised, focal changes in myocardium. No pallor, haemorrhage or yellow-tan discolouration.
4	No localised, focal changes in myocardium. No pallor, haemorrhage or yellow-tan discolouration.
5	No localised, focal changes in myocardium. No pallor, haemorrhage or yellow-tan discolouration.
6	No localised, focal changes in myocardium. No pallor, haemorrhage or yellow-tan discolouration.
7	Bleeding under epicardium in the anterior wall/septum region towards the RV. Small signs of haemorrhage (septum/apex and septum/valves).
8	No localised, focal changes in myocardium. No pallor, haemorrhage or yellow-tan discolouration.

Table 6.7: Summary of histology findings

	Inhomogeneity/ altered staining	Cell infiltration	Contraction bands	Cardiac myocyte damage
1	–	–	–	–
2	Yes	–	No, loosened fibers (remote)	–
3	–	–	–	–
4	–	–	–	–
5	–	–	–	–
6	–	Yes, inflammatory & neutrophil granulocytes	–	–
7	–	–	–	Initial (infarct, remote (less))
8	–	Yes, inflammatory & neutrophil granulocytes	–	Initial (infarct, remote (less))

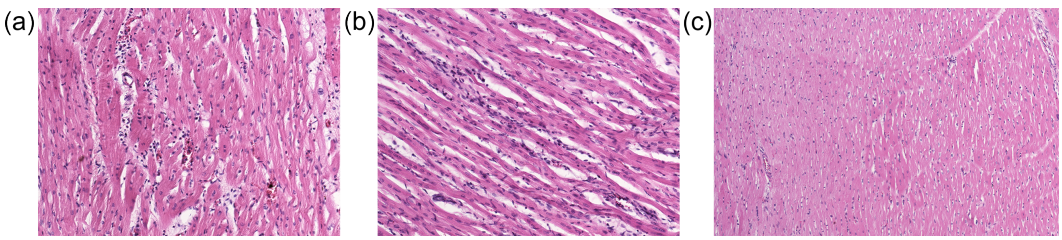

Figure 6.13: Examples of histological findings. (a) Inflammatory infiltration / neutrophil granuocytes (b) Beginning inflammation (c) Commencing myocyte damage.

7 Post-mortem MR angiography: Feasibility and imaging approaches in a forensic cohort

In a final phase, PMMRA as described in the developmental procedure of this thesis was applied in forensic cadavers. PMMRA was performed following MPMCTA [9] in cases of suspected sudden cardiac death to evaluate various imaging applications for the visualisation of the coronary arteries. These examinations enabled an initial investigation of the feasibility of PMMRA with paraffin oil and Angiofil® (6% PA) and provided insight into the diagnostic potential of PMMRA.

7.1 Methods

This section describes the methods employed in the feasibility study undertaken on forensic cadavers (n=8). Aspects associated with the technical feasibility of PMMRA were examined. SNR was quantified to identity differences between two 3D isotropic MRI sequences as well as to investigate the influence of temperature and explore myocardial enhancement in detectable in PMMRA. Due to the developmental nature of the study, optimisation of the data acquisition strategy sometimes led to data related to a specific technique only being acquired for some cases. For each image analysis presented, the number of cases analysed is specified.

7.1.1 Study population

All examinations on forensic cadavers were performed at the University Center of Legal Medicine (Lausanne-Geneva) (CURML) in Switzerland. Cadavers included in this study were forensic cases in which an autopsy (including post-mortem imaging) was commissioned by the local prosecuting authority. Post-mortem MRI was performed prior to and following MPMCTA in cases of suspected sudden cardiac death. For the selection of cases from the routine case work at CURML, the defined inclusion criteria for this feasibility study were: adults ($>$ 18 years of age), M/F, suspected sudden cardiac death, mandated full autopsy. Exclusion criteria were the presence of artifact inducing implants/prosthetics (e.g. pacemaker, metallic intubation materials/tubes, metallic clips/markers, metal dental fillings),

thorax trauma caused by external forces (e.g. gunshot/knife wound to thorax) and extreme putrefaction.

7.1.2 Experimental protocol and image acquisition

Rectal temperature measurements were taken before and after native PMMR as well as before and after PMMRA. Mean temperatures calculated from the measurements before and after each acquisition are found in Table 7.1.

Table 7.1: Mean rectal temperature (°C) for each phase (native, filled) of MRI acquisition.

Case	$Temp_{Native}$	$Temp_{Filled}$
1	38.5	37.5
2	33.6	31.6
3	18.1	19.2
4	20.7	19.9
5	27.5	27.8
6	33.2	31.1
7	18.1	18.2
8	7.9	8

Native PMMR images were acquired following native PMCT and prior to vascular filling with 6% PA [9]. Scan parameters for the relevant native and filled vessel protocols are detailed in Table 7.2.

Table 7.2: Scan parameters for acquisition of native and angiographic MRI data (forensic cadavers).

Sequence	Resolution (mm)	Slices	TR (ms)	TE (ms)	FA (°)	BW (Hz/Px)	TA (min:sec)
3D GRE	$0.8 \times 0.8 \times 2$	60-70	13.8	5.5	13	431	3:30
3D T1w GRE	$0.8 \times 0.8 \times 0.8$	140-160	10	4.6	40	180	9:00
3D T1w Dixon	$0.9 \times 0.9 \times 0.9$	180-200	6.44	2.37/4.75	15	805	10:00

Vascular filling was not additionally evaluated in this feasibility study. PMMRA was performed directly after MPMCTA using a standardised protocol for which the challenges and typical filling defects are known [45]. The mean time between completion of MPMCTA and commencement of PMMRA was 21 minutes (max. delay 1 hour).

7.1.3 Feasibility of PMMRA following MPMCTA

As proposed in [167] the technical feasibility of PMMRA was assessed in terms of recruitment capability and resulting sample characteristics, data collection and the acceptability of study procedures. Recruitment capability was evaluated via the study enrolment rate over the time period June 2017 to March 2018. Sample characteristics including age, gender, temperature and distribution of coronary and other pathologies were summarised. The need to refine data collection was assessed by examining changes to the MRI protocol and the completeness of MRI and temperature data. Finally, the acceptability of study procedures was subjectively determined through personal communication with forensic and radiological specialists at the CURML.

7.1.4 Signal-to-noise ratio

All SNR calculations in this section were performed according to Eq. 2.1. The correlation between SNR and the measured rectal temperature was determined based on Pearson's correlation coefficient. Significance of correlation results was determined based on $\alpha = 0.05$.

Myocardial enhancement in PMMRA

Myocardial enhancement was evaluated for four cadavers (n=4) in which the same imaging sequences and parameters were applied in the native and filled phases (Table 7.2, 3D GRE). Calculation of the mean signal intensity was performed in two regions of interest (ROI_{signal}), which were placed in myocardium at the mid-cavity level in approximately anterior and inferior regions. A ROI_{noise} was defined in the image background. All ROIs were manually defined five times and SNR was calculated for each repetition. SNR values are presented as average values over all repetitions.

Comparison of 3D imaging sequences

All cases (n=8) were analysed for the comparison of 3D imaging sequences. For 3D T1w GRE and 3D T1w Dixon (fat) images a ROI_{signal} was defined in the filled right ventricle and a ROI_{noise} in the image background. SNR values were compared against the rectal temperature measurement to determine if there was any correlation. Pearson's r was calculated for each sequence.

7.1.5 Visualisation of coronary arteries

Filling of the vascular system, improved contrast between the coronary arteries and surrounding tissue, compare with native PMMR. Additionally reperfusion of the post-mortem vascular system counteracted a known challenge in of post-mortem MRI, the assessment of collapsed vessels. To demonstrate this effect, examples are presented of images from the native and filled phases. Additional examples of acquired images exploiting the high signal intensity of the perfusate and 3D isotropic nature of the acquired data demonstrate the versatility and visualisation possibilities in selected cases (n=3). All visualisations were performed with the open-source software RadiAnt DICOM Viewer.

7.2 Results

This section outlines the results related to the feasibility assessment of PMMRA, which highlighted challenges associated with performing PMMRA in routine forensic practice. A comparison between two 3D MR imaging techniques for vascular visualisation, the correlation between cadaver temperature and SNR as well as the extent of myocardial enhancement are described in this section.

7.2.1 Feasibility of PMMRA following MPMCTA

Eight cases were included in this feasibility study over the time period of 10 months. In this time, approximately 401 PMCT examinations and 123 PMMR examinations were performed (Figure 7.1) at CURML. Under the assumption that almost all cases examined at the institute undergo native CT, the largest possible recruitment pool was 401 cases. Although not all these met the strict inclusion criteria and despite the motivated efforts of the forensic imaging unit, the recruitment capacity for PMMRA in cases of sudden cardiac death was nevertheless assessed as low. Sample characteristics (Table 7.3) demonstrated an similar distribution of coronary and other pathologies, the age range corresponded to expectations, given the pathology of interest and both genders were represented. Data collection was refined through minor technical changes to the MRI protocol (e.g. TE of the four 3D GRE sequence in the native and filled phase) and adaptation of the temperature measurement protocol (e.g. no measurement of the temperature if MPMCTA and PMMRA were less than 3 hours apart). Temperature and MRI data were reliably collected and transferred for analysis. The acceptability of the study was strongly influenced by time and personal resources (e.g. requirement to perform all imaging procedures prior to same day autopsy).

Table 7.3: Summary of sample characteristics.

Enrolled cases	n=8
Age (years)	54.2 ± 11.8 [range: 40.1 - 78.2]
Gender	Female (n=2); Male (n=6)
Pathology	Coronary (n=5); Other (n=3)

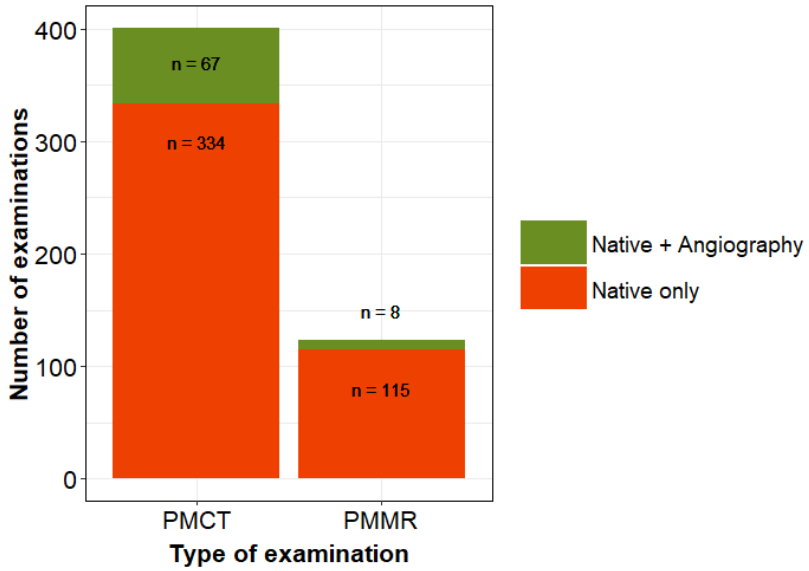

Figure 7.1: Number of post-mortem imaging examinations over a period of 10 months. In total 401 PMCT examinations were performed, 67 of which also underwent PMCTA. A total of 123 PMMR examinations were performed, 8 of which underwent PMMRA.

7.2.2 Myocardial enhancement in PMMRA

Intra-sample comparison of SNR indicated that in 6/8 ROI_{Signal}, SNR_{Filled} was greater than SNR_{Native}. However, examination of SNR in all samples revealed that mean differences in SNR were within a single standard deviation for each phase (Table 7.4). Due to the small sample size and preliminary nature of this study, additional statistical analysis was not performed to determine if mean values were statistically different.

Table 7.4: Mean SNR (± SD) for ROIs positioned at the mid-cavity level in anterior and inferior myocardial regions.

Case	Position	SNR_{Native} (mean±SD)	SNR_{Filled} (mean±SD)
5	Anterior	1514±391	7316±4321
5	Inferior	1195±284	3942±1646
6	Anterior	3106±2112	1003±426
6	Inferior	2614±3029	3359±1660
7	Anterior	1801±810	2254±1618
7	Inferior	1421±302	1749±165
8	Anterior	1943±223	1853±236
8	Inferior	1859±83	2294±427
All	–	**1932±638**	**2971±1984**

7.2.3 Comparison of 3D imaging sequences

Visually, both 3D MRI sequences delivered excellent contrast and suitable resolution. From the Dixon sequence, four separate images were reconstructed (fat, water, in-phase, opposed-phase). While fat images are primarily of interest for vascular visualisation, due to the lipophilic nature of the perfusate, the other images obtained may offer additional diagnostic value. SNR values and the corresponding rectal temperature measurements are displayed in Figure 7.2.

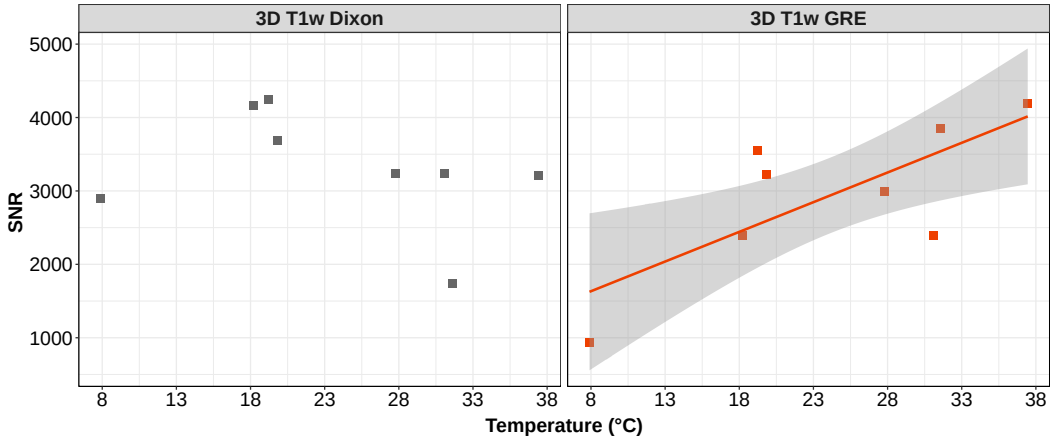

Figure 7.2: SNR of 6% PA in the right ventricle (n=8) for 3D T1w GRE and 3D T1w Dixon images. Correlation between SNR and temperature was 0.74 and -0.34 for these acquisitions respectively. A linear model demonstrating the significant correlation between the SNR(3D T1w GRE) and temperature is displayed. Shaded area corresponds to standard error. No model is shown for 3D T1w Dixon data as the correlation was not statistically significant.

Similar SNR values were observed for both sequences. The calculated Pearson's r was 0.74 for 3D T1w GRE images and -0.35 for 3D T1w Dixon images, indicating a positive correlation for the former and weak negative correlation for the latter. However, linear modelling only found a significant linear correlation between SNR and temperature for the 3D T1w GRE sequence (p-value = 0.03).

7.2.4 Visualisation of the coronary arteries

The filled coronary arteries were well visualised in PMMRA using the isotropic 3D T1w GRE and 3D T1w Dixon sequences. Multi-planar reformatting of data enabled arbitrary positioning of the imaging planes post-acquisition (Figure 7.3), which introduced increased flexibility for post-mortem MR radiological examinations.

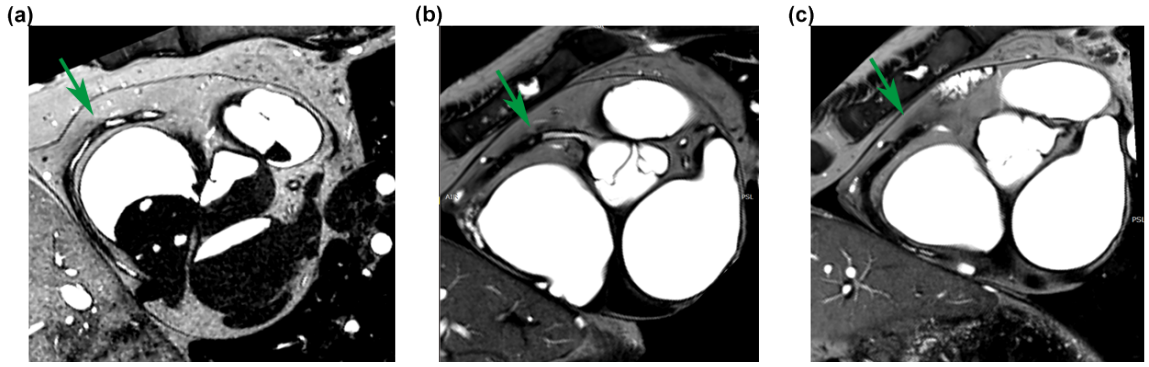

Figure 7.3: Examples of multi-planar reformatting of 3D isotropic data using open-source software. The abrupt stop (arrows) of the perfusate indicates occlusion of the artery, which was later confirmed at autopsy.

8 Discussion

In this section, the results of the previously described examinations are discussed in more detail. Aspects of the interpretation and discussion of the results (Chapter 3 and 5) may appear similarly in published work [48, 92].

8.1 Fundamental characterisation and evaluation of candidate perfusates

A successful approach to post-mortem MR angiography requires the careful selection of an appropriate perfusate. The liquid chosen to perfuse the post-mortem vascular system provides the fundamental basis for the quality and stability of vascular filling. Furthermore, it delivers the intrinsic foundation for image contrast and the subsequent visualisation of post-mortem vessels. In the current work, candidates were evaluated based on properties related to vascular filling (e.g. viscosity and chemical nature) as well as intravascular retention in *ex vivo* porcine arteries. Based on these properties, in combination with the MR relaxation behaviour of these fluids, preferred perfusates for the performance of PMMRA were determined.

8.1.1 Vascular filling and intravascular retention

The development of post-mortem CT angiography techniques has demonstrated the diagnostic value and limitations of these techniques compared with native post-mortem CT examinations and conventional autopsy techniques [3, 41, 45]. Methodological developments and routine implementation of PMCTA in numerous forensic institutes have collectively demonstrated the fundamental elements for successful performance of post-mortem angiography-based imaging [168], where reliable radiological assessment of the reperfused vascular system is based on the underlying assumption that vascular filling is complete and artifact-free. While in practice this may not always be the case, artifacts can be minimised by reproducible, complete vessel filling which exhibits temporal stability for the duration of foreseen imaging examinations.

Due to the delicate state and increased permeability of the post-mortem vascular wall, viscosity and the nature of a liquid (hydrophilic, lipophilic or hygroscopic) play an important role in controlling intravascular retention and the extent to which small vessels, arterioles or even capillaries are filled [153, 168]. Furthermore, the temperature-dependent behaviour of

a perfusate needs to be predictable because, unlike in clinical examinations, where subject (patient) temperature is assumed to be constant (mean: 36.6°C [95% range 35.7-37.3°C]) [169], the temperature range of post-mortem examinations is much larger [64].

Factors influencing extravasation have previously been investigated using animal models [7, 8] and during the development of a standardised protocol for multi-phase PMCTA [9], confirming that properties such as lipophilicity and viscosity, which affect the behaviour of perfusates in the post-mortem vascular system [168], influence the reliability and stability of post-mortem vascular filling and consequently, the interpretation of post-mortem angiography results.

Determination of perfusate viscosity

Reduced viscosity allows more distal vascular filling [7], which may additionally reduce intravascular retention as the perfusate enters the smaller, more permeable vessels. Increased viscosity can counteract these effects by preventing distribution of perfusate into the capillary bed [153]. A balance between these factors is considered to deliver optimal results in post-mortem angiography applications. Given the temperature-dependent nature of dynamic viscosity, the systematic evaluation of proposed perfusates commenced with the characterisation of viscosity in candidate perfusates. To date, the majority of forensic studies which have examined this important physical property did so for temperatures of 20°C [50] or 25°C [153]. As shown by investigation of perfusate temperature changes in cadavers, the in-cadaver perfusate temperature can extend beyond this range [92] during post-mortem examinations, necessitating knowledge of viscosity behaviour across this temperature range.

Combining information gained from the determined quadratic temperature models of perfusate viscosity (Table 3.5, Figure 3.2) with the established relationship between dynamic viscosity and vessel filling [50, 153], liquids which would reliably perfuse all vessels of interest over a forensically relevant temperature range were defined. An in-cadaver dynamic viscosity range between 15-100 mPa·s was deemed appropriate. Viscosities above 15 mPa·s have been shown to prevent capillary distribution of the perfusate [153], while higher viscosities ($\sim$ 55 mPa·s) have indicated a longer intravascular retention [50]. However, once the viscosity becomes too high, the perfusate can no longer pass through the small arteriovenous shunts, potentially preventing the reliable filling of vasculature essential for radiological examinations [159].

Minimal temperature dependence of viscosity was an additional preferred characteristic of potential perfusates for PMMRA. Minimal temperature dependence improves the pre-

dictability of perfusate behaviour and minimises changes in vessel filling due to differences in cadaver temperature. Suitably low temperature dependence was defined by examination of the coefficients of the quadratic models explaining changes in dynamic viscosity due to temperature. Perfusates with $A_{visc} <$ -2.00 and $B_{visc} <$ 1.00 (Table 3.5) demonstrated sufficiently low temperature dependencies.

Based on the desired dynamic viscosity range and minimal temperature dependence between 8 and 20 °C, paraffin oil and 6% paraffin oil & Angiofil® were categorised as preferred perfusates. Dynamic viscosities of these perfusates remained in the range 32.5-65.5 mPa·s over the investigated temperatures.

Investigation of intravascular retention

The extent to which a given perfusate remains intravascular significantly influences the stability of vascular filling, the importance of which has been highlighted in research regarding PMCTA [49]. This is especially relevant as the duration of imaging examinations increases, for example in post-mortem MR angiography where sequence parameters can be adapted to take advantage of post-mortem circumstances (e.g. lack of motion and flow) to achieve very high spatial resolution. PMMR examinations can, as a result, become quite time intensive, especially when compared to CT procedures. In this context, minimising extravasation of PMMRA perfusates is essential.

To investigate this effect in more detail, intravascular retention of paraffin oil, PEG200 and a Gadovist®-doped physiological solution in porcine LAD artery was examined. The rate at which extravasation occured varied depending on the perfusate. Various models exist which attempt to describe the regulation of vascular permeability and the transport of molecules across the vascular barrier, with the exact mechanism describing transport out of the lumen and into surrounding tissue depending on vessel type, organ, kinetics of transport and the nature of the substance being transported [170]. These mechanisms have primarily been investigated in living systems, nevertheless some aspects may be transferable to a post-mortem context.

Extravasation of perfusates out of the vessel into which they were injected, may be described by passive transport mechanisms which can occur at at least two different locations in the vascular system. Firstly, passive transport of small molecules across the vessel wall would be possible. Even in living systems suitable molecules can extravasate spontaneously via this mechanism [170]. In this case, both molecular (e.g. size, polarity, hydrophilicity and viscosity) and vascular properties play an important role in determining which substances permeate the vascular wall. Since vessel integrity is assumed to decrease post-mortem compared to *in vivo*

conditions [7], the physiological solution containing Gadovist® may have quickly diffused directly through the vessel walls into adjacent myocardium. The same mechanism may also explain the disappearance of PEG200 from the LAD artery within the first hour after injection. Similarities in the molecular properties influencing passive transport across the vessel wall can be found between PEG200 and Gadovist® molecules. For example, both molecules can be classified as polar and are highly soluble in aqueous environments. Conversely, paraffin oil is non-polar and virtually insoluble in aqueous environments, indicating that the passive transport of these molecules may have been inherently positioned to fail.

The second location at which extravasation could have occured is across the much more permeable single-layer epithelium of the capillaries. This relies on an assumed penetration of the capillary network by the perfusate. Extravasation of PEG200 and Gadovist® into surrounding tissue via this mechanism is also very plausible. Regarding paraffin oil, a study by Grabherr et al. [8] described the viscosity of a lipophilic contrast agent as a trigger of embolisation in post-mortem capillaries, thus directly determining the calibre of vessels able to be filled. Work in the current thesis supports the hypothesis that paraffin oil remained intravascular due to its inability to penetrate the microcapillaries, therefore being unable to take advantage of the increased permeability of these vessels.

8.1.2 Intrinsic MR relaxation behaviour of perfusates

The intrinsic properties of a substance or tissue provide the basis for signal generation in MRI, thereby directly influencing both signal intensity and image contrast. Characterisation and evaluation of these properties in liquids being considered for post-mortem MR angiography was therefore an essential step in the development process. The relaxation behaviour of liquids was characterised in test tubes at four temperatures between 1 and 23°C. A positive correlation between relaxation times (T_1, T_2) and temperature was confirmed and modelled. The quadratic models used to fit the data displayed small residual standard error, indicating their suitability for this purpose. Achieving positive contrast between a perfused liquid and surrounding tissue requires liquids to have a shorter longitudinal relaxation time (hyperintense on T1-weighted images) and/or a longer transverse relaxation time (hyperintense on T2-weighted images), than surrounding tissue.

T_1 relaxation times in PEG200, PEG400, paraffin oil, Angiofil®, 6% PA and Gadovist®-doped water (2 mmol/l) [156, 157] were shorter than values for cadaveric tissue [85], meaning these liquids would appear brighter than tissue on T1-weighted images at a given temperature between 1-23°C. Regarding the experimentally obtained T_2 relaxation times, for all perfusates except both PEG solutions, these were longer than in cadaveric tissue [85]. Therefore, these

liquids would appear brighter than tissue on T2-weighted images.

While it is undisputable that Gadovist®-doped water delivers excellent T1-weighted contrast, the physical characteristics described above pose specific challenges in terms of post-mortem intravascular retention over a longer period of time. Therefore, considering the physical characteristics as well as the relaxation behaviour of perfusates, preferred perfusates were: paraffin oil and 6% PA. Both displayed very similar behaviour in all aspects and the presence of Angiofil® did not present any ascertainable advantages or disadvantages. These fluids were considered equally suitable for post-mortem MR angiography.

8.2 MR imaging techniques for the post-mortem assessment of cardiac pathologies

Subsequent to the determination of fundamental physical and MR properties of perfusate candiates and with the objective of addressing current weaknesses in the forensic radiological assessment of sudden cardiac death, different imaging strategies for PMMRA were evaluated. The added value of PMMRA lies not in its ability to closely mimic images acquirable in PMCTA, but rather in its potential to provide complementary information regarding the nature of a suspected vascular occlusion or the pathological consequences of an occlusion, such as signs of myocardial ischaemia in the region ordinarily perfused by the occluded vessel. Through its superior ability to distinguish subtle differences in soft tissue, MRI offers advantages for the characterisation of occlusions and and post-mortem myocardium. Therefore, the focus of the evaluation of MR imaging techniques presented in this section is two-fold. Firstly, a strategy for optimal imaging of the reperfused cardiovascular system in terms of spatial and contrast resolution was investigated. Secondly, infarcted and remote regions in post-mortem myocardium were characterised terms of relaxation and diffusion properties using a preclinical porcine model.

8.2.1 Visualisation of the post-mortem vascular system in MRI

Spatial and contrast resolution of images are key elements in the visualisation of vessel-like structures in post-mortem tissue. Sequences capable of achieving high spatial resolution were evaluated. As demonstrated by the *in vitro* characterisation of potential perfusates, the largest intrinsic differences between perfusates and post-mortem myocardium or fat, based on experimental results and models [64] were between the longitudinal relaxation times. Therefore, T1-weighted imaging sequences were particularly well suited to optimise

contrast between perfusates and surrounding post-mortem tissue. This finding is supported by previous work by Bruguier et al. [91], where various sequences (2D/3D, T1w/T2w, with/without fat saturation) were applied to visualise coronary arteries filled with paraffin oil and Angiofil®. Here, the imaging protocol was based on requirements such as maximal examination time of 1 hour, high spatial resolution, contrast between filled vessels and surrounding tissue (T1w), as well as within the myocardium (T2w) and the desire for 3D data for MIP and multi-planar reconstructions [91]. An extensive evaluation of individual acquisition sequences was not presented in [91], which motivated the phantom experiments undertaken in the current thesis.

Evaluation of selected clinically-available sequences in a porcine tissue phantom

In an *ex vivo* porcine tissue phantom, four MR sequences were quantitatively evaluated in terms of the accurate depiction of vessel-like cross-sections, CNR_{eff} and perceived image blur. Visually, all sequences delivered good contrast and acceptable resolution for all tube sizes. Comparison of intensity profile peak widths with the known inner diameter of tubes (2, 3, 4 mm), indicated that overestimation relative to the true inner diameter was largest for the smallest diameter (2 mm). Peak widths were estimated between discrete peak minima (i.e. at the first voxel next to perfusate signal where signal was minimised). This was assumed to represent the position of the tube wall. Combined with the partial volume effect, this assumption explains the general overestimation (1-2 pixels) of the diameter using peak width measurements. Inter-sequence differences within this range were therefore not considered meaningful. Minima were not observed in the TIR images, leading to greater uncertainty in these measurements of peak width due to the assumption that the position of the tube wall corresponded to zero signal. The spatial resolution in all sequences was evaluated as being sufficient for the identification and assessment of coronary occlusions, especially given that occlusions leading to STEMI in a clinical context are generally clustered in the proximal third of each coronary artery [20], where vessel diameters are in the range 3-4.5 mm [160].

Contrast was compared between sequences using CNR_{eff}. For the previously identified preferred perfusates (i.e. paraffin oil and 6% PA), the 2D T1w TSE sequence delivered the highest CNR_{eff}. CNR_{eff} determines the contrast-to-noise ratio in relation to acquisition time, making it a valuable tool in the comparison and evaluation of different sequences [126]. The T2w SPACE sequence also performed well and presents certain advantages in the post-mortem examination of myocardial infarction due to its T2-weighting (e.g. for detection of oedema in myocardium) and 3D isotropic acquisition (e.g. for multi-planar reformatting). The T1w GRE sequence performed satisfactorily and could also be adapted in the future to obtain 3D imaging data with strong T1-weighting, however SNR and CNR

would need to be reassessed in this case.

Quantification of image blurring using the previously described blur metric and indicated that the blurriest images were those acquired with the T1w TSE sequence. The accelerated (turbo) nature of this sequence, where multiple 180° rephasing pulses are applied in an echo train to reduce acquisition time, may have contributed to this blurriness. The applied echo train length was nine, meaning echoes used to fill the periphery regions of k-space contain influences of T_2 decay. Reducing this factor may lead to improvements in image quality. The T1w GRE sequence performed best in terms of blurriness, which demonstrated the suitability of this imaging approach for the sharp depiction of small, vessel-like structures.

Evaluation of perfusates using a 3D GRE sequence

A 3D GRE sequence was selected for MR imaging of porcine hearts into which one of three potential perfusates was injected. 3D isotropic data acquisition is particularly well-suited for angiography applications since it enables post-acquisition reformatting of the data into the desired orientation.The nature of spoiled gradient echo sequences enables T1 weighting with short acquisition times, due to the short TR achievable. Although temporal resolution in post-mortem MR angiography is not comparably important as in clinical contrast-enhanced MRA, where the effects of contrast agent in the blood pool need to be captured in a short amount of time, the overall acquisition time nevertheless plays a role in the routine implementation of the technique. Furthermore, time can in such cases be better invested to improve additional aspects related to overall image quality (e.g. spatial resolution).

In the examinations undertaken on porcine hearts, SNR and CNR calculations were used to provide an indication of image quality. For these examinations all morphological images were acquired using the same sequence and SNR in remote myocardium and epicardial fat remained constant across all samples (Table 5.3). Therefore, using the CNR was a valid approach for comparison of the contrast generated by each perfusate. Due to the T1 weighting of the 3D GRE sequence used to acquire the morphological images, it was expected that the shorter the T_1 relaxation of a given perfusate, the brighter the vessels would appear. This behaviour was experimentally confirmed, with the Gadovist® solution (T_1[23°C]: 100 ms) [157] displaying the highest CNR, followed by paraffin oil (T_1[23°C]: 207 ms) [92] and PEG200 (T_1[23°C]: 216 ms) [92]. Although differences were observed between the perfusates in terms of CNR, all perfusates displayed excellent CNR immediately following injection and filled vessels were easily distinguishable from surrounding myocardium and epicardial fat.

Potential imaging and diagnostic consequences of extravasation

In addition to the temporal differences in the extravasation of perfusates, differences in the visibility of perfusate displacement in MR images could influence the diagnostic possibilities offered by MR images.

Excellent CNR against both remote myocardium and epicardial fat was observed for the Gadovist® solution, which quickly diffused into small vessels and adjacent myocardium. Immediately following injection, many small, filled vessels were observed in detail in the T1w images (Figure 5.5). After the first hour contrast between the LAD artery and adjacent myocardium began to diminish due to the propagation of the solution further into surrounding tissue which presented as blurring at the vessel interface, compared with earlier images. This had the effect of reducing discrimination between vessels and myocardium, an effect which intensified with time and which can be prominently seen in images acquired 12 hours after injection. In Figure 5.5 the LAD artery seemed to have entirely disappeared at this time point. One could argue that an enhancement effect, as seen in clinical late gadolinium enhancement, may be beneficial in the post-mortem detection of myocardial infarction. However, this study demonstrated that even in non-pathological porcine hearts, distribution of the Gadovist® solution was fast and unpredictable. Nevertheless, a Gadovist® solution as perfusate may contribute to additional enhancement effects in regions corresponding to specific pathologies. Unfortunately, this intriguing aspect fell outside the scope of this work.

Paraffin oil, which primarily remained intravascular, provided consistent visualisation of vascular morphology. Analogue to PMCTA, which visualises vascular occlusions and morphology, T1w imaging, visualised paraffin oil filled vessels without confounding signal from epicardial fat or myocardium.

PEG200 offered neither extended intravascular retention nor tissue enhancement effects such as those observed immediately following injection of the Gadovist® solution. PEG200 appeared hyperintense in the filled LAD arteries in morphological images acquired immediately after injection, however within an hour the solution was no longer visible. The slight increase in the T_1 values in adjacent myocardium in two samples between the last two measurement time points (i.e. one and 12 hours) supports the hypothesis that PEG200 exravasated into surrounding myocardium during this time. Unlike the Gadovist® solution, which strongly shortens the longitudinal relaxation times of protons in surrounding water molecules, the slightly shortened T_1 relaxation times observed in the case of PEG200 likely reflect a direct measurement of the protons within the -CH_2 bonds [171] of the PEG molecule, thereby explaining the much milder effect. Since the effects of PEG200 extravasation do not present

an improvement for diagnostic purposes, this solution cannot be recommended as a reliable perfusate for PMMRA, where extended examination times may significantly reduce its visibility in the vascular system.

8.2.2 Preclinical trial: *Ex vivo* characterisation of myocardial infarction in MRI

Since the diagnostic potential of PMMR relies not only on the visualisation of the post-mortem vascular system, but can also take advantage of quantitative tissue characterisation techniques, the significance and potential diagnostic value of these methods was also investigated. In recent years, the quantitative characterisation of post-mortem myocardium in MRI has been investigated for the differentiation of stages of myocardial infarction. Characterisation of T_1, T_2 and proton density has been performed in forensic cohorts at 1.5 T [30] and 3T [65, 84] using commercially available software (SyntheticMR [89, 90]). Additionally, differentiation between healthy and infarcted myocardium using post-mortem cardiac DTI has been investigated in a forensic cohort at 3T [86]. Despite their heterogenous nature (subject age, post-mortem interval, exact pathology and temperature (corrected for in [30, 65])), these studies demonstrate the feasibility of quantitative post-mortem cardiac MRI. Taking a step back, our preclinical trial performed together with the Department of Cardiology at the Medical University of Graz provided an excellent opportunity to investigate the consequences of lethal myocardial infarction, in which the survival time was extremely short ($<$ 30 minutes), on quantitative MR parameters. These examinations were performed with a short, consistent post-mortem interval ($\sim$ 2 hours), at a constant temperature (23-25°C) and systematically induced, known myocardial pathology. Documentation of macroscopic and conventional histological findings was also performed.

Comparison of T_1 and T_2 relaxation times for remote myocardium

Across all samples examined in the current work, the mean T_1 for non-pathological myocardium at room temperature (23-25°C) was 718 $\pm$ 26 ms.

Clinical and *ex vivo* cardiac research generally implements clinically relevant (non gold-standard) acquisition sequences suitable for application in the presence of *in vivo* conditions, such as cardiac motion, for quantification of MR relaxation parameters in myocardium. For example, myocardial T_1 is primarily quantified using inversion recovery-based techniques such as the widely accepted MOLLI with high precision and spatial resolution, but a systematic underestimation of myocardial T_1 values [172] resulting from the calculation of the 'apparent

T_1' and its correction to estimate T_1 [173]. Saturation-recovery techniques, such as SASHA [174] which have demonstrated higher accuracy than Look-Locker techniques have also been implemented, with the disadvantage of lower precision due to lower, spatially varying SNR [173, 175].

A general comparison of results obtained in this work with *ex vivo* porcine T_1 and T_2 values in unfixated myocardium proved challenging. One study at 1.5T was found in which the LAD in swine was ligated for 30 minutes. T_1 values of 833 ms in the *ex vivo* porcine hearts at approximately 20-24°C were obtained at 1.5 T with a Look-Locker sequence [176]. A simple, generalised comparison between T_1 values in this and the current work was challenging due to differences in field strength and measurement sequence. Nevertheless, myocardium T_1 values of were expected to be lower at 1.5 T than at 3 T, as demonstrated in [177], where *in vivo* (37°C) differences of approximately 100 ms (1.5T: 950 $\pm$ 21, 3T: 1052 $\pm$ 23 ms [MOLLI]) were observed.

Given the sparcity of *ex vivo* porcine experiments investigating relaxation times in post-mortem myocardium, we compared our results with two recent studies in which relaxation times in post-mortem human myocardium were acquired using SyntheticMR (QRAPMASTER) [90] at 3T. Comparison with non-temperature corrected non-pathological human myocardium, indicated that T_1 values ($T_{1\ [65]} = 889.7 \pm 97.9$ ms; $T_{1\ [85]} = 938.9 \pm 129.1$ ms) were higher than those determined in the current work ($T_1 = 718 \pm 26$). Comparison of T_1 relaxation times with non-temperature corrected values was deliberate because a comparison with directly measured values was desired. Additionally, very little detail is given in the work by Persson et al. as to the establishment of the presented temperature models, their standard error or range of validity. In the study by Zech et al. the mean uncorrected T_1 value may approximately correspond to the mean recorded temperature (16.8°C). However, this is merely an assumption as this information is unfortunately not discernible from the data presented [85]. A brief comparison of the skeletal muscle temperature model in [85] with an alternative temperature model in porcine muscle [156] demonstrated important differences between linear models (temperature coefficients: 8.66 [85] vs. 13.1 [156]), indicating uncertainty remains regarding the exact temperature dependence of muscular tissue.

Nevertheless, the apparent underestimation of T_1 values in our work is concerning and may represent systematic error in the absolute measured T_1 values. The turbo inversion recovery sequence applied for data acquisition is understood to induce magnetization transfer (MT) effects due to the RF refocusing pulses it employs [178]. These pulses can contribute to signal loss compared with conventional spin echo acquisitions [178]. A systematic underestimation of absolute T_1 values obtained using TIR sequences in the brain was previously reported by Turner et al. as most probably being due to MT effects [179]. The severity of these

effects is influenced by the acquisition of multiple 2D slices, in which case MT effects also accumulate from slice to slice due to the slice selective pulses applied and the associated off-resonance excitation in adjacent slices [179]. On the other hand, a recent study examining MR relaxation times in the post-mortem brain at 3T, which was performed using similar relevant acquisition parameters to those in the current thesis (e.g. turbo factor and slice thickness), argued that after comparison with literature values, the severity of MT effects on T_1 relaxation times under their experimental conditions seemed to be minimal [63]. However, given that the severity of MT effects has been hypothesised to be a function of the magnetization rate constant and density of molecules which are effective in magnetization transfer [179], the exact influence of MT on the T_1 values in post-mortem myocardium under our experimental conditions needs to be investigated in further detail in future work. Despite the aforementioned limitations of the data acquisition strategy employed in this work, there are many advantages in applying TIR sequences for the measurement of T_1 relaxation times, as additionally highlighted by Birkl et al. [63]. TIR data acquisition reduces acquisition time compared with conventional IR-SE sequences, thereby enabling acquisition within a short PMI ($\sim$ 2 hours) and tissue temperature stability (23-25°C) in our work.

Mean T_2 for remote myocardium at room temperature (23-25°C) was 70 $\pm$ 4 ms. Temperature models for T_2 of post-mortem myocardium found in the literature indicate that the temperature dependence of T_2 in muscle tissue is minimal. In linear models at 3T, the temperature coefficients were determined to be between 0.04 [85] - 0.13 [65] for myocardium and -0.35 [85] and 0.1 [156] for human and porcine muscle respectively. With a temperature difference of 13°C (ΔT = 37-24°C), this would equate to absolute differences in T_2 of between 0.5 and 2.2 ms, depending on the model used. Such values are smaller than the standard deviation of measured values in this and other studies. Therefore, to facilitate discussion of the obtained results, the influence of temperature will be regarded as negligible. Direct comparison with *in vivo* values nevertheless presents additional challenges due to measurement technique differences, cardiac and respiratory motion, oxygenation state of haemoglobin, and these should not be lightly disregarded in the comparison of *in vivo* and *ex vivo* quantitative T_2 values.

Comparison with *in vivo* T_2 relaxation times measured with a MSE sequence (TE_1 = 12 ms, ΔTE = 5.8 ms, 9 echoes) at 3T revealed these were shorter (52.0 $\pm$ 3.6 ms [180]) than our results in *ex vivo* porcine myocardium. An additional study at 3T using three variations of the MSE sequence (2, 4 and 8 images used for parameter mapping) yielded values between 57.6-61.6 ms for healthy myocardium [181]. *In vivo* transverse relaxation times found in the literature were observed to be systematically lower than those obtained in the current work. In addition to the abovementionned possible explanations for such discrepancies, additional factors may include decomposition processes which lead to a general increase in the water

content and mobilty [182]. However, these effects are considered to have been minimal given the small time PMI prior to MRI acquisitions ($\sim$2 hours). T_2 relaxation times obtained in forensic cadaveric myocardium measured according to Warntjes et al. [90] were also lower ($T_{2\ [65]} = 52.4 \pm 5.8$ ms, $T_{2\ [85]} = 59.5 \pm 6.4$ ms) than relaxation times observed in our preclinical study. Additional factors such as tissue oxygen levels may also influence relaxation times, as suggested in [183] and the influence of post-mortem tissue oxygenation levels on relaxation times should be investigated in detail in future work.

The variation in normal myocardial relaxation times is known to vary depending on the vendor, data acquisition and mapping method selected for data analysis [173]. Unfortunately, no mention of data corresponding to gold standard measurement techniques for T_1 or T_2 was found in the two aforementioned forensic cohorts [65, 85], nor elsewhere in the literature for estimation of relaxation times in post-mortem cardiac tissue. A direct comparison of relaxation times using the method proposed in [90] and standard measurement techniques was additionally problematic, because the sequence is only available under commercial license [89]. Therefore, a comprehensive comparison between T_1 and T_2 measured according to standard methods in the current work with literature values under similar circumstances was not possible.

Differences between infarcted and remote regions in *ex vivo* porcine myocardium

Regarding the relaxation times in infarcted *ex vivo* porcine myocardium (T_1: 683 $\pm$ 21 ms, T_2: 67 $\pm$ 3 ms) and remote regions (T_1: 718 $\pm$ 26 ms, T_2: 70 $\pm$ 4 ms) , a decrease in both T_1 and T_2 was observed in infarcted porcine myocardium.

Comparison with 'early acute MI' values presented in the aforementioned study in forensic cadavers [65], revealed that increased T_1 was observed in tissue histological confirmed to correspond to early acute MI. However, in the same publication 'early acute' was defined as corresponding to MI which had been survived for between 6 - 24 hours [65]. Therefore, these are only marginally comparable with our findings in the controlled preclinical study presented here. Combining findings in [65] with those observed in infarcted regions known to exist due to survival times of less than 30 minutes, it may be hypothesised, that initial biological processes following the onset of ischaemia, shorten T_1 relaxation, while continuation of these processes leads to a prolongation of T_1 relaxation times. This hypothesis is further supported by the observed decrease in T_1 (958 ms [IQR: 945-988]) in ischaemic myocardium compared with infarcted myocardium ($T_1 = 1053$ ms [IQR: 989-1088]) [184]. Therefore, a comparison with observations in ischaemic tissue rather than infarcted tissue may be more valid to understand the underlying mechanisms of T_1 changes in the myocardium following complete acute vessel occlusion leading to sudden cardiac death.

A possible underlying mechanism for the observed decrease in T_1 may be an aggregation of erythrocytes in the coronary arteries or myocardium. T_1 has been shown to linearly decrease with increased hematocrit fraction (Hct), with differences of 0.08 in the Hct leading to shortening of T_1 in arterial ($\downarrow$ 125 ms) and in venous blood ($\downarrow$ 160 ms) [185]. Hct describes the erythrocyte volume fraction in blood and aggregation has been signalled as a useful marker in the detection of inflammatory response [186]. In the presence of normal blood flow, erythrocytes are easily dispersed, however as demonstrated by a recent study, local aggregation can occur in the coronary arteries adjacent to myocardial infarction survived for between 3-6 hours (determined at autopsy) [187]. This aggregation may provide a possible explanation for the decrease in T_1 observed in the infarcted region in the current work, however the presence of extracelluar erythrocytes should have been visible in the H&E stained histology samples taken, which somewhat contradicts this explanation.

Statistically significant differences in T_2 were also observed between the remote and infarcted regions of post-mortem porcine myocardium. Clinical research advocates for the evaluation of T_2 relaxation in cases of acute myocardial infarction and has already demonstrated its application in cases of focal oedema [116, 188, 189]. However, the assumption of inflammatory signs such as hyperintense oedema in post-mortem T2w images in the context of early acute myocardial infarction should be carefully considered prior to acceptance. Observations in our work indicate a slight decrease in T_2 immediately following the onset of fatal myocardial ischaemia. This is concordant with findings of decreased T_2 during the early stages of focal cerebral ischaemia in rats [190] and the observation of a hypointense region in T2w images which, according to [191], indicated a extremely early stage of myocardial infarction (0-6 hours) in the absence macroscopic findings during dissection of the heart [191]. Possible causes for the shortening of T_2 were briefly hypothesised in [64] and include decreased intracellular pH (i.e. acidosis) and decreased interstitial water content in the ischaemic region.

An increase in free protons (H^+) directly results from anaerobic metabolism which occurs following myocardial hypoxia [22]. Work investigating the effect of pH on transverse relaxation *in vitro* and in preclinical animals models using an MR spectrometer (24 MHz) indicated that changes in T_2 depend on the initial pH, due to the parabolic shape of the fitted model [192]. Cyanide-induced acidosis (max. Δ pH = 0.31) was found to decrease T_2 by up to 5% in rats [192]. However, examination of the effect of pH on transverse relaxation in skeletal muscle found that a reduction in intracellular pH resulted in prolongation of T_2 times [193]. The influence of pH on transverse relaxation therefore requires further investigation, which was outside the scope of this thesis.

Under normal conditions, myocardial fluid filtration, the process by which fluid leaves the

microvascular exchange vessel and enters the cardiac interstitium, is balanced with fluid removal from the cardiac interstitium via lymphatic vessels [194]. Since this process is governed by physical factors such as hydrostatic and oncotic forces, in the presence of a physical barrier (e.g. arterial obstruction), it may be hypothesised that the interstitial water content could be at least partially depleted due to continued lymphatic draining of the myocardial interstitium. This would result in the observation of decreased T_2 due the strong correlation between T_2 and water content [195].

The complex processes associated with interstitial water content, the influence of an increased concentration of free protons in ischaemic or infarcted tissue as well as the effects of local vs. global ischaemia on MR relaxation require additional research to enable definitive conclusions related to the underlying mechanisms responsible for the results obtained in our preclinical study.

Diffusion Tensor Imaging

Historically, the primary application for DTI was in the brain and central nervous system, however as recent advances demonstrate this technique is now finding application in the musculoskeletal [196], peripherical nerve systems [196] and heart [120]. Fractional anisotropy and the molecular diffusion rate (mean diffusivity (MD), apparent diffusion coefficient (ADC)) are commonly used measures to describe diffusion. Learning from changes in diffusion parameters in the setting of acute ischaemic stroke, the examination of these parameters in *ex vivo* porcine hearts was hypothesised to support identification of alterations in the molecular diffusion rate in infarcted myocardium. According to work in the field of acute ischaemic injury in the brain, MD was expected to decrease in the early hours of ischaemia [197, 198]. This decrease has also been shown to occur parallel to the depletion of ATP [199], a known metabolic occurence during ischaemia. While change in FA over this time period not yet been fully evaluated, evidence exists that it tends to increase in the ischaemic lesion [198].

In the current work, two 2D EPI sequences were compared. Two key observations were made regarding these data. Firstly, lower FA values were generated from the EPI_A data. This difference may be partially explained by differences in the acquisition parameters. For example, the different b-values applied in each sequence or the different number of gradient directions. EPI_A used b=0, 500, 1000 while the EPI_B contained an additional b-value at 2000 s/mm^2. The number of gradient directions was also different ($EPI_A = 20$, $EPI_B = 64$). Average FA has been found to decrease with an increased number of gradient directions, which may explain the difference in mean FA values between data acquired with different sequences [200]. Furthermore, an increased number of imaging directions has been shown

to correlate with increased accuracy of FA [200], indicating FA from EPI_B may in fact be more accurate. The second observation was a difference in the standard deviation of the FA and MD maps, based on VOI analysis. The standard deviation was approximately halved in data acquired with the EPI_A compared to EPI_B. The opposite effect was actually expected, since SNR in b-value images acquired with EPI_A were much lower than those obtained for EPI_B images. Observed differences may be due to the effects of eddy currents which were unfortunately not additionally corrected for prior to tensor estimation. On the other hand the distance between slices in the EPI_B which incorporated simultaneous multi-slice acceleration may have been too small, leading to inter-slice (signal) leakage. However, spacing between slices (1.65 mm) was larger than slice thickness (1.5 mm), which should have been sufficient to counteract this effect.

Our DTI results for remote regions in *ex vivo* porcine myocardium corresponded excellently with work by Mazumder et al. [201] who examined the impact of fomalin fixation on healthy and infarcted porcine hearts. In their work, pre-fixation values for FA (0.42 ± 0.028) in healthy myocardial tissue were concordant with our values ($FA_{EPI_A} = 0.41 \pm 0.08$), a statement which was also valid for $MD_{[201]} = 0.52 \pm 0.026$ x 10^{-3} $mm^2.s^{-1}$. In our work mean MD_{EPI_A} in the remote region was 0.55 ± 0.07 x 10^{-3} $mm^2.s^{-1}$. A cross-comparsion between our values in the infarcted region and those in [201] was not relevant, since Mazumder et al. focused on fibrosis and remodelling in the infarcted region related to chronic myocardial infarction. However, a discernible difference between the FA and MD values in [201] and those in our work was the standard deviation, which was three times larger in our data. In addition to the influences discussed above, our large standard deviation may also be explained by the absence of additional eddy current correction, leading to a slight mismatch of distorted voxels prior to tensor estimation. DTI examinations have also been performed in a moderately sized forensic cohort to assess post-mortem FA and MD values in cases of acute and chronic myocardial infarction [86], where FA values were lower than ours and MD higher. An increase in the ADC values of the liver with increasing post-mortem interval [69] with differences between of up to 0.2 x 10^{-3} $mm^2.s^{-1}$ was previously observed over the first 5 hours following death. The PMI in [86] was 19 ± 11 hours, this extended PMI may account for the slightly higher MD observed ($\Delta MD = 0.09$ x 10^{-3} $mm^2.s^{-1}$) compared to our values, obtained after a PMI of approximately two hours.

Differences in the FA and MD were not found to be statistically significant between regions of the myocardium. It would nevertheless be interesting to perform additional diffusion-related calculations to determine if for example alternative denoising or distortion correction algorithms play a role in reducing the variation in FA and MD values, potentially leading to the identification of statistically significant differences between the infarcted and remote regions.

Image acquisition and analysis limitations

The results obtained in the evaluation of quantitative parameters can be considered reliable due to the data acquisition and fitting strategies employed. Nevertheless, the sensitivity of T_1 measurements to imperfect inversion pulses [202] and, specifically in the context of 2D imaging, non-ideal slice profile [145] represent potential sources of error in the results obtained. Despite its gold standard status, IR-based T_1 measurement may contain inaccuracies, for example due to RF pulse amplitude errors [145]. Such errors may arise from the application of imperfect inversion pulses, whose angle then deviates from the assumed 180° [145, 202]. To help correct for variations in the inversion pulse flip angle, a three parameter fit was used to determine T_1 as described in Eq. 2.17. Additionally, and as is particularly relevant in 2D multi-slice applications, slice-selective pulses cannot be assumed to deliver square slice profiles, which additionally influences the effective flip angle across the slice [145]. These effects, combined with the previously discussed aspects related to MT may have influenced the accuracy of the T_1 values obtained.

For parameter fitting, a voxel-wise approach was chosen to generate the relevant parameter maps. Although this approach may present disadvantages in that noise can have a stronger influence on fitting results, here this drawback was outweighed by the benefits of voxel-wise fitting, namely facilitated interpretation and the visualisation of parameteric values over the entire image space. Additionally, more complex models such as those based on bloch equation simulations [203] or generating functions [204] exist for the estimation of T_2 relaxation. Unfortunately, investigation of these models and their applicability for post-mortem quantitative MR data was outside the scope of this thesis, however these are interesting approaches which should be investigated in future work.

Further limitations of the image acquisition, processing and analysis procedures applied in this study include tthe absence of additional correction for eddy currents in diffusion weighted data. As mentioned above, this may have contributed to an increased standard deviation in the resulting FA and MD maps. The systematic evaluation of multiple denoising approaches and optimisation of their application may further decrease the variance in FA and MD maps as was demonstrated for T_1 values in [130]. Finally, the VOIs used for comparison of the suspected infarction region and corresponding remote region in porcine myocardium were not defined by a radiologist and this definition was not blinded. Nevertheless, the preclinical nature of the study, knowledge of the occluded vessel and image appearance are considered to have minimised potential error introduced due to the non-radiological definition of VOIs.

Experimental limitations

A potential experimental limitation was the *ex situ* set-up selected for examination of *ex vivo* porcine hearts. This set-up did not enable elimination of air-related influences. However, given the foreseen *ex vivo* application of the MR imaging techniques presented in this thesis, and the general presence of air in cadavers, this set-up is expected to at least partially represent the intended end application. While initial investigations may benefit from a more uniform environment, final method optimisation will need to focus minimising the effects of air, especially for the acquisition of diffusion weighted data, rather than on its removal.

The development and especially validation of new cardiac MRI techniques can benefit from preclinical examinations prior to their translation into routine application [205]. Especially for the observation of cardiovascular pathology and derivation of MR parameters, experimental isolated porcine models can provide reproducible information [205]. Nevertheless such models make assumptions, which need to be critically reviewed for the particular application. Firstly, acute myocardial infarction was induced by injection of ethanol into the LAD artery [206]. This approach was not expected to replicate the development of chronic cardiac pathologies, for example coronary luminal stenosis, but rather an acute coronary occlusion. Although this represents a very specific event, it was important to keep the variables in this clinical study as controlled and homogeneous as possible, due to the small sample size. Furthermore, a correlation between the injected volume of ethanol and infarct size has been demonstrated by Li et al. [207]. Since the injected volume is known only to be between 10-20 ml, the infarct size was not assessed in this study due to the uncertainty regarding the exact injection volume. Finally, the exact survival time of swine was not recorded. It is only known that this time was between 10 and 30 minutes. For future studies, it may be possible to improve the interpretation of quantitative MR parameters by correcting for the interval between ethanol injection and death.

8.3 Investigation of post-mortem MR angiography in a forensic cohort

The small feasibility study undertaken during this thesis generated data for initial analysis of the myocardial enhancement in PMMRA. The data obtained in the current work further enabled determination of the temperature dependence of signal-to-noise ratio in two imaging sequences, which were found to be suitable for application in PMMRA. Additionally, this study examined the practical, technical and operational aspects related to the feasibility of PMMRA in routine forensic practice.

8.3.1 Imaging approaches

The systematic investigation of perfusates and image sequences was approached from many angles in this thesis. Progressing from *in vitro* experiments towards a porcine phantom, preclinical model and finally forensic cohort enabled detailed examination of various influential factors which have collectively contributed to the presented approach to post-mortem MR angiography. Due to the intrinsically fast T_1 relaxation of paraffin oil (with or without the addition of Angiofil®), PMMRA using T1-weighted MRI sequences was particularly attractive. T1-weighted imaging has the additional advantage of been time efficient if gradient echo sequences are selected. Such sequences allow acquisition of 3D isotropic T1-weighted image volumes which cover the entire thorax (spatial resolution: 0.78x0.78x0.78 mm^3, acquisition time: 8-9 minutes). Examination of the temperature dependence of SNR indicated a positive correlation with the 3D GRE sequence, however this factor did not considerably influence the visual quality of images acquired using the developed approach to PMMRA. This is likely due to the stability of T_1 relaxation (6% PA) across a forensically relevant temperature range as demonstrated by its small temperature coefficient in the models presented in Table 3.7.

Due to the lipophilic nature of the perfusate, an additional direction was also explored for visualising the cardiovascular system. The application of fat/water separation techniques not only produces fat images with excellent perfusate contrast and comparable resolution (0.9x0.9x0.9 mm^3, acquisition time: 11 minutes), but also offers additional diagnostic value via in and out-of-phase images as well as water images.

Unfortunately, the sample size in this feasibility study was too small to robustly evaluate myocardial enhancement in PMMRA. The interpretation of tissue enhancement results in post-mortem imaging needs to be carefully examined and statistically analysed in a larger cohort to determine the influence of confounding factors such as PMI, temperature and state of decomposition.

8.3.2 Feasibility of PMMRA in a forensic cohort

The study protocol was specifically designed to evaluate the feasibility of PMMRA in cases of suspected sudden cardiac death, a potential indication for PMMRA. The recruitment capacity of the study may have been influenced by the strict inclusion (and exclusion) criteria for PMMR examination in general and PMMRA specifically. However, this does and should not represent a unique situation. Given the financial and personnel effort associated with performing additional PMMR examinations, as well as potential delays in autopsy procedures,

a specific hypothesis and indication for PMMRA should be defined through future scientific investigation of the diagnostic value of the technique.

Discussion with specialists at CURML strongly indicated that the duration of a PMMRA protocol was extremely relevant for routine implementation. The duration of our scientific study protocol does not necessarily represent a routine protocol, which for example if only a single 3D isotropic T1w GRE (or Dixon) sequence were to be acquired, would last less than 20 minutes including cadaver positioning and temperature measurements. The requirement for both native and filled vessel scans for comparative purposes also influenced the duration and effort associated with PMMRA examinations in this feasibility study. Depending on the indication, it may be necessary to decide upon a single modality (native PMMR or PMMRA), however there are many factors which will contribute to this decision in the future. For example, the effects of perfusate on the quantitative MR parameter mapping need to be investigated in more detail. Initial examinations in a very small sample indicate that paraffin oil does not significantly alter T_1 in myocardium directly adjacent to a reperfused coronary artery (Chapter 5) [48]. However, to date quantitative MR examination of cadavers completely perfused with paraffin oil (or other perfusates) has not been undertaken.

9 Summary and future direction

This thesis presented and evaluated various quantitative and angiography-based post-mortem MRI techniques for the assessment of sudden cardiac death. The results of these investigations are summarised below. Additionally, the future direction of research to improve and optimise the minimally-invasive assessment of sudden cardiac death using MRI is also discussed.

9.1 Post-mortem MR imaging techniques for the assessment of sudden cardiac death

To evaluate MR imaging approaches which can be applied in the assessment of sudden cardiac death, an angiography-based technique focussing on the visualisation and morphological assessment of vessels, in particular the coronary arteries, was systematically developed and applied in a small forensic cohort. Furthermore, quantitative MR imaging approaches, the application of which is increasingly being recommended in the context of clinical cardiovascular MRI, were investigated in a preclinical model.

9.1.1 Angiography-based imaging approaches

Selection of an appropriate perfusate for post-mortem MR angiography provides the fundamental physical basis for stable, reliable filling of the post-mortem vascular system and the intrinsic foundation for image contrast and the visualisation of post-mortem vessels. Candidate perfusates included lipophilic (e.g. paraffin oil, Angiofil®, silicon oil, mineral oil), hydrophilic (e.g. Gadovist®-doped water) and hygroscopic (e.g. polyethylene glycol) liquids. For temperatures between 8 and 20 °C, the dynamic viscosities of these perfusates were below 203 mPa·s. Across a similar temperature range (1-23°C), characterisation of the longitudinal and transverse relaxation behaviour of candidate perfusates at 3T indicated that all liquids had short to medium T_1 and T_2 relaxation times. Preferred perfusates were defined as those with short T_1 and longer T_2 relaxation times, relative to post-mortem myocardium and fat. Additionally, preference was given to perfusates which displayed stability in both viscosity and MR relaxation over the entire temperature range (i.e. low temperature dependence). Overall, T_1 relaxation times for PEG, paraffin oil, 6% paraffin oil & Angiofil® and Gadovist®-doped water (2 mmol/l) were at least 100 ms below corresponding cadaveric tissue values from [64]. For these same substances, lipophilic liquids (i.e. paraffin oil, 6%

paraffin oil & Angiofil®) displayed T_2 relaxation times longer than post-mortem myocardium and fat, according to [64].

Following, an evaluation of clinically available sequences for the visualisation of vessel-like structures in *ex vivo* porcine tissue, which indicated that both T1-weighted and T2-weighted sequences would be suitable for PMMRA imaging applications, further examinations were performed using *ex vivo* porcine hearts at a constant temperature (23-25 °C). Visualisation of porcine coronary arteries filled with one of three preferred perfusates (PEG200, Gadovist®-doped physiological solution and paraffin oil) using a 3D GRE sequence was assessed. Sufficient CNR was achieved for all perfusates. CNR was maximal for vessels filled with the Gadovist®-doped physiological solution (183 ± 63 (myocardium); 161 ± 60 (epicardial fat)). Simultaneously, the intravascular retention of the potential perfusates was evaluated over 12 hours. Changes in the signal intensity in the filled artery (left anterior descending artery) within the first hour were statistically significant (p-value $\ll 0.001$) for all samples injected with PEG200. In the same time frame, changes in the signal intensity of myocardial tissue adjacent to the filled LAD artery were statistically significant (p-value $\ll 0.001$) for all samples injected with the Gadovist®-doped physiological solution. Quantitative changes in the T_1 of myocardium in the same region confirmed these observations and also indicated that additional T_1 changes in samples injected with Gadovist®-doped physiological solution occurred between this time point and final data acquisition, 12 hours later. The visual stability of paraffin oil was statistically confirmed by the absence of significant changes in signal intensity or T_1 relaxation times in myocardium adjacent to the filled LAD at any time point.

The feasibility study performed in this work (n=8) provided data for initial analysis of the myocardial enhancement in PMMRA and indicated temperature dependence of SNR in one of the applied MR imaging sequences. Although pathological enhancement of the myocardium at post-mortem CT angiography using the same perfusate as applied in our approach to PMMRA has been recently associated with increased levels of cardiac troponins [105], this was not able to be confirmed in our small sample. A positive correlation between signal-to-noise ratio (3D T1w GRE) and temperature was observed, however this did not influence visual image quality. The feasibility of PMMRA following MPMCTA was examined and although found to be technically feasible, financial and personnel resources will require the definition of specific indications for the routine performance of PMMRA. Such indications will need to be determined and investigated in future research to more precisely elucidate the diagnostic value of post-mortem mortem MR angiography in the assessment of sudden cardiac death.

9.1.2 Quantitative imaging approaches

To further exploit the diagnostic potential of post-mortem MR for the assessment of sudden cardiac death, techniques for quantitative tissue characterisation were investigated in a preclinical trial examining relaxation behaviour of infarcted (ischaemic) and non-pathological post-mortem myocardium at 3T. Survival time following induced myocardial infarction was extremely short ($<$ 30 minutes), after which MR examinations were performed with a short, consistent post-mortem interval ($\sim$ 2 hours), at a constant temperature (23-25°C). The measured absolute relaxation times for non-pathological myocardium were consistently shorter than those found in the literature, however a direct comparison in terms of temperature, field strength and other experimental conditions was not possible. T_1 and T_2 relaxation times were shortened in the infarcted (ischaemic) regions (T_1: 683 $\pm$ 21 ms, T_2: 67 $\pm$ 3 ms) compared with remote regions of the *ex vivo* porcine myocardium (T_1: 718 $\pm$ 26 ms, T_2: 70 $\pm$ 4 ms). These differences were statistically significant (p-value $<$ 0.05). The observed decrease was not in agreement with existing studies in forensic cohorts [65, 84], however differences may be plausibly attributed to the unknown and inconsistent survival time of deaths determined to be due to (early) acute myocardial infarction (0-24 hours) as defined in the aforementioned studies. Alternatively, we observed a concordance between our results and those presented by Assen et al. [184] (T_1 quantification), where a decrease in T_1 was also seen in the early phase of myocardial ischaemia. Regarding T_2 relaxation, our results also appeared concordant with non-quantitative observations of hypointensity in T2-weighted images (assumed ischaemic myocardium) in cases of early acute MI without macroscopic findings at autopsy [107]. Diffusion parameters were also estimated in post-mortem porcine hearts, where the fractional anisotropy and mean diffusivity values obtained for non-pathological myocardium (FA: 0.41 $\pm$ 0.08, MD: 0.55 $\pm$ 0.07) were in excellent agreement with literature values [201]. Despite agreement with literature trends for diffusion parameters in infarcted tissue (e.g. decreased MD and increased FA in early acute ischemic stroke [198]), no statistically significant difference was observed between regions of interest in our work.

9.2 Future research

Expanding on published literature detailing the general feasibility of post-mortem MR angiography and quantitative post-mortem MRI for the minimally-invasive imaging assessment of sudden cardiac death as well as the results presented in this thesis, this section advocates potential future directions for research in this field.

9.2.1 Visualisation of the post-mortem vascular system in MRI

The implementation of fat water separation techniques, represent an interesting expansion or imaging approaches dedicated to the morphological assessment coronary arteries and post-mortem myocardium. As demonstrated in this work, techniques such as 3D isotropic T1w Dixon imaging can deliver multiple images with different contrast from a single acquisition. The derived fat images are particularly suitable for the visualisation of the post-mortem vascular system while water images may contain important diagnostic information relevant for the differentiation between acute and chronic myocardial infarction, or for the suppression of vessel lumen and consequential enhancement of vessel walls. The simultaneous visualisation of vasculature may prove to be advantageous in the evaluation of vessel occlusions and potentially the differentiation between post-mortem clots and ante-mortem thrombi.

Aspects briefly addressed in the small feasibility study performed during this thesis deserve comprehensive examination in a larger cohort. As demonstrated by recent work in the field of PMCTA [105, 106], contrast enhancement effects in histologically confirmed regions of myocardial infarction have been observed in PMCTA. Examination of these effects, their quantification and significance may present an interesting future application for PMMRA. Furthermore, the correlation of SNR and temperature as well as the diagnostic consequences of any correlation should be examined over a larger number of samples. Finally, the diagnostic value of PMMRA in the assessment of sudden cardiac death and its specific contribution to decisions regarding cause of death needs to be evaluated and compared with existing imaging (e.g. PMCTA, PMMR) and autopsy techniques.

Generally accepted advantages of reperfusion of the post-mortem vascular system include greater resemblance to near *in vivo* conditions, facilitating morphological assessment of not only vascular pathologies but also anatomical anomalies [42, 168]. Specific indirect advantages of filled vessels in the context of PMMR may include reduced susceptibility artifacts through the reduction of air bubbles, for example in vessels due to lack of circulation and other post-mortem phenomena.

9.2.2 Tissue characterisation of post-mortem myocardium

A multitude of technical, circumstantial and biological factors have the potential to influence quantitative characterisation of relaxation and diffusion properties in post-mortem tissue. Recently multi-parameteric approaches have been suggested for the characterisation of ischaemic post-mortem myocardium [84]. However, prior to commencement of large cohort studies with multiple quantitative parameters, a number of factors potentially influential

in the estimation of tissue properties need to be systematically assessed under controlled conditions. For example, the effects of pre-processing algorithms such as those applied for denoising and registration of acquired data prior to parameter fitting need to be evaluated to ensure robust data processing. Furthermore, optimisation and correction diffusion weighted imaging data processing as well as exploration of more complex diffusion models could be investigated. Additionally, alternative parameter fitting procedures and modelling of temperature and post-mortem interval influences could be examined to reduce and correct for measurement and circumstance related variation between samples. Finally, strategies to effectively combine quantitative parameters should be comprehensively assessed to maximise diagnostic value.

In future steps for example towards multi-centre studies using quantitative MR imaging, additional site-specific factors related to data acquisition as well as calibration or correction requirements will also need to be addressed to ensure robust, comparable data which improves the assessment of sudden cardiac death using MRI.

9.3 Conclusion

In conclusion it can be stated that during this study a systematically developed approach to PMMRA was evaluated and the feasibility of same demonstrated in a forensic cohort. Additionally, quantitative MR techniques potentially valuable in the diagnosis of sudden cardiac death were found to quantify differences in infarcted and non-pathological post-mortem myocardium in a preclinical model. With this work the foundation has been laid for the further investigation und development of post-mortem applications of MR imaging in the context of sudden cardiac death.

Bibliography

[1] S. L. Saunders et al. "Targeted post-mortem computed tomography cardiac angiography: Proof of concept". In: *International Journal of Legal Medicine* 125 (2011), pp. 609–616. DOI: 10.1007/s00414-011-0559-4 (cit. on pp. 2, 14).

[2] C. Robinson et al. "Pump injector system applied to targeted post-mortem coronary artery angiography". In: *International Journal of Legal Medicine* 127 (2013), pp. 661–666. DOI: 10.1007/s00414-012-0802-7 (cit. on pp. 2, 14).

[3] G. N. Rutty et al. "Diagnostic accuracy of post-mortem CT with targeted coronary angiography versus autopsy for coroner-requested post-mortem investigations: a prospective, masked, comparison study". In: *The Lancet* 390.10090 (2017), pp. 145–154. DOI: 10.1016/s0140-6736(17)30333-1 (cit. on pp. 2, 14, 16, 20–22, 99).

[4] S. Ross et al. "Postmortem whole-body CT angiography: Evaluation of two contrast media solutions". In: *American Journal of Roentgenology* 190 (2008), pp. 1380–1389. DOI: 10.2214/ajr.07.3082 (cit. on pp. 2, 14, 45).

[5] C. Jackowski et al. "Postmortem imaging of blood and its characteristics using MSCT and MRI". In: *International Journal of Legal Medicine* 120 (2006), pp. 233–240. DOI: 10.1007/s00414-005-0023-4 (cit. on pp. 2, 14, 22, 24).

[6] W. Schweitzer et al. "Very economical immersion pump feasibility for post mortem CT angiography". In: *Journal of Forensic Radiology and Imaging* 5 (2015), pp. 8–14. DOI: 10.1016/j.jofri.2015.11.009 (cit. on pp. 2, 14).

[7] S. Grabherr et al. "Postmortem angiography after vascular perfusion with diesel oil and a lipophilic contrast agent." In: *American Journal of Roentgenology* 187 (2006), W515–23. DOI: 10.2214/ajr.05.1394 (cit. on pp. 2, 14, 100, 102).

[8] S. Grabherr et al. "Angiofil: a novel radio-contrast agent for post-mortem microangiography". In: vol. 7078. 2008, p. 707810. DOI: 10.1117/12.792077 (cit. on pp. 2, 100, 102).

[9] S. Grabherr et al. "Multi-phase post-mortem CT angiography: Development of a standardized protocol." In: *International Journal of Legal Medicine* 125 (2011), pp. 791–802. DOI: 10.1007/s00414-010-0526-5 (cit. on pp. 2, 14, 18, 21, 22, 45, 91, 92, 100).

[10] D. R. Messroghli et al. "Clinical recommendations for cardiovascular magnetic resonance mapping of T1, T2, T2* and extracellular volume: A consensus statement by the Society for Cardiovascular Magnetic Resonance (SCMR) endorsed by the European Association for Cardiovascular Imaging (EACVI)". In: *Journal of Cardiovascular Magnetic Resonance* 19.1 (2017), p. 75. DOI: 10.1186/s12968-017-0389-8 (cit. on pp. 2, 26, 27).

[11] R. B. Kotabagi, S. C. Charati, and D. Jayachandar. "Clinical Autopsy vs Medicolegal Autopsy". In: *Medical Journal, Armed Forces India* 61.3 (2005), pp. 258–263. DOI: 10.1016/s0377-1237(05)80169-8 (cit. on p. 4).

[12] A. Eriksson. *Forensic epidemiology*. Ed. by M. D. Freeman and M. P. Zeegers. Amsterdam: Academic Press, 2016. Chap. 6 (Forensic Pathology), pp. 151–177 (cit. on p. 4).

[13] C. Basso et al. "Guidelines for autopsy investigation of sudden cardiac death: 2017 Update from the Association for European Cardiovascular Pathology". In: *Virchows Archiv* 471.6 (2017), pp. 691–705. DOI: 10.1007/s00428-017-2221-0 (cit. on pp. 4, 5, 10, 11).

[14] B. Levy. "The need for informatics to support forensic pathology and death investigation". In: *Journal of Pathology Informatics* 6 (Apr. 2015), p. 32. DOI: 10.4103/2153-3539.158907 (cit. on p. 4).

[15] E.-L. Stattin et al. "Genetic screening in sudden cardiac death in the young can save future lives". In: *International Journal of Legal Medicine* 130 (2015), pp. 59–66. DOI: 10.1007/s00414-015-1237-8 (cit. on p. 4).

[16] B. Madea, ed. *Rechtsmedizin: Befunderhebung, Rekonstruktion, Begutachtung*. 3rd. Springer-Verlag Berlin Heidelberg, 2015 (cit. on pp. 4, 5, 7, 13).

[17] A. Maseri, S. Chierchia, and G. Davies. "Pathophysiology of coronary occlusion in acute infarction." In: *Circulation* 73.2 (1986), pp. 233–239. DOI: 10.1161/01.CIR.73.2.233 (cit. on pp. 5, 7).

[18] K. Michaud et al. "Pathomorphological and CT angiographical characteristics of coronary atherosclerotic plaques in cases of sudden cardiac death". In: *International Journal of Legal Medicine* 129.5 (2015), pp. 1067–77. DOI: 10.1007/s00414-015-1191-5 (cit. on pp. 6, 9, 10).

[19] R. Virmani et al. "Lessons from sudden coronary death: a comprehensive morphological classification scheme for atherosclerotic lesions". In: *Arterioscler Thromb Vasc Biol* 20 (2000), p. 1262. DOI: 10.1161/01.atv.20.5.1262 (cit. on p. 6).

[20] J. C. Wang et al. "Coronary Artery Spatial Distribution of Acute Myocardial Infarction Occlusions". In: *Circulation* 110.3 (2004), pp. 278–284. DOI: 10.1161/01.CIR.0000135468.67850.F4 (cit. on pp. 6, 104).

[21] J. Silvain et al. "Composition of Coronary Thrombus in Acute Myocardial Infarction". In: *Journal of the American College of Cardiology* 57.12 (2011), pp. 1359–1367. DOI: 10.1016/j.jacc.2010.09.077 (cit. on p. 6).

[22] L. S. L. June-Wha Rhee Marc S. Sabatine. *Pathophysiology of Heart Disease. Acute Coronary Syndromes*. Ed. by L. S. Lilly. 5th. Philadelphia, PA: Lippincott Williams and Wilkins, 2011. Chap. 7, pp. 161–189 (cit. on pp. 6–9, 111).

[23] K. Thygesen et al. "Third Universal Definition of Myocardial Infarction". In: *Circulation* 126.16 (2012), pp. 2020–2035. DOI: 10.1161/CIR.0b013e31826e1058 (cit. on p. 7).

[24] D. J. Hearse. "Myocardial ischaemia: can we agree on a definition for the 21st century?" In: *Cardiovascular Research* 28.12 (1994), pp. 1737–1744. DOI: 10.1093/cvr/28.12.1737 (cit. on p. 7).

[25] V. Fineschi, M. Silver, and G. Baroldi. *Pathology of the Heart and Sudden Death in Forensic Medicine*. Boca Raton: CRC Press, 2006 (cit. on p. 7).

[26] R. B. Dettmeyer. *Forensic Histopathology*. Heidelberg: Springer-Verlag, 2011 (cit. on pp. 8, 9, 11).

[27] A. Farb, A. L. Tang, and A. P. Burke. "Sudden coronary death: frequency of active coronary lesions, inactive coronary lesions, and myocardial infarction". In: *Circulation* 92 (1995), p. 1701. DOI: 10.1161/01.cir.92.7.1701 (cit. on p. 10).

[28] T. Ayoub and J. Chow. "The conventional autopsy in modern medicine". In: *J R Soc Med* 101.4 (2008), pp. 177–81. DOI: 10.1258/jrsm.2008.070479 (cit. on p. 10).

[29] C. Mondello, L. Cardia, and E. Ventura-Spagnolo. "Immunohistochemical detection of early myocardial infarction: a systematic review". In: *International Journal of Legal Medicine* 131.2 (2017), pp. 411–421. DOI: 10.1007/s00414-016-1494-1 (cit. on p. 11).

[30] N. Schwendener et al. "Detection and differentiation of early acute and following age stages of myocardial infarction with quantitative post-mortem cardiac 1.5 T MR". In: *Forensic Science International* 270.270 (2017), pp. 248–254. DOI: 10.1016/j.forsciint.2016.10.014 (cit. on pp. 11, 17, 20, 21, 23, 24, 42, 107).

[31] W. Casscells et al. "Immunohistochemical study of fibronectin in experimental myocardial infarction". In: *Am J Pathol* 137.4 (1990), pp. 801–10 (cit. on p. 11).

[32] B. Brinkmann, M. A. Sepulchre, and G. Fechner. "The application of selected histochemical and immunohistochemical markers and procedures to the diagnosis of early myocardial damage". In: *International Journal of Legal Medicine* 106.3 (1993), pp. 135–141. DOI: 10.1007/BF01225234 (cit. on p. 11).

[33] H. Thomsen and H. Held. "Immunohistochemical detection of C5b-9(m) in myocardium: an aid in distinguishing infarction-induced ischemic heart muscle necrosis from other forms of lethal myocardial injury". In: *Forensic Science International* 71.2 (1995), pp. 87–95. DOI: 10.1016/0379-0738(94)01640-Q (cit. on p. 11).

[34] S. Sabatasso et al. "Early markers for myocardial ischemia and sudden cardiac death". In: *International Journal of Legal Medicine* 130.5 (2016), pp. 1265–1280. DOI: 10.1007/s00414-016-1401-9 (cit. on p. 11).

[35] S. Sabatasso et al. "Early markers of myocardial ischemia: from the experimental model to forensic pathology cases of sudden cardiac death". In: *International Journal of Legal Medicine* 132.1 (2018), pp. 197–203. DOI: 10.1007/s00414-017-1605-7 (cit. on p. 11).

[36] O. Kawamoto et al. "Immunohistochemistry of connexin43 and zonula occludens-1 in the myocardium as markers of early ischemia in autopsy material". In: *Histology and Histopathology* 29.6 (2014). cited By 6, pp. 767–775. DOI: 10.14670/HH-29.767 (cit. on p. 11).

[37] A. Aljakna, T. Fracasso, and S. Sabatasso. "Molecular tissue changes in early myocardial ischemia: from pathophysiology to the identification of new diagnostic markers". In: *International Journal of Legal Medicine* 132.2 (2018), pp. 425–438. DOI: 10.1007/s00414-017-1750-z (cit. on p. 11).

[38] T. D. Ruder. "What are the key objectives of the ISFRI? Evaluation of the ISFRI member survey". In: *Journal of Forensic Radiology and Imaging* 1.3 (2013), pp. 142–145. DOI: 10.1016/j.jofri.2013.05.001 (cit. on pp. 12, 16).

[39] R. Dirnhofer et al. "VIRTOPSY: Minimally Invasive, Imaging-guided Virtual Autopsy". In: *RadioGraphics* 26.5 (2006), pp. 1305–1333. DOI: 10.1148/rg.265065001 (cit. on p. 12).

[40] M. Baglivo et al. "The rise of forensic and post-mortem radiology—Analysis of the literature between the year 2000 and 2011". In: *Journal of Forensic Radiology and Imaging* 1.1 (2013), pp. 3–9. DOI: 10.1016/j.jofri.2012.10.003 (cit. on p. 12).

[41] S. Grabherr et al. "Post-mortem imaging in forensic investigations: current utility, limitations, and ongoing developments". In: *Research and Reports in Forensic Medical Science* 6 (2016), pp. 25–37. DOI: 10.2147/rrfms.s93974 (cit. on pp. 12, 20, 99).

[42] S. Grabherr, J. Grimm, and A. Heinemann, eds. *Atlas of Postmortem Angiography*. Springer International Publishing, 2016 (cit. on pp. 12–16, 122).

[43] H. Fischer and A. Heinemann. "Arbeitsgemeinschaft für Forensische Bildgebung der Deutschen Gesellschaft für Rechtsmedizin: Grundlagen der postmortalen Computertomographie (PMCT) für forensisch-radiologische Anwendungen – Empfehlungen und Indikationskatalog". In: *Rechtsmedizin* 26 (2016), pp. 284–290. DOI: 10.1007/s00194-016-0096-z (cit. on p. 13).

[44] C. Palmiere et al. "Detection of hemorrhage source: The diagnostic value of postmortem CT-angiography". In: *Forensic Science International* 222 (2012), pp. 33–39. DOI: 10.1016/j.forsciint.2012.04.031 (cit. on p. 13).

[45] S. Grabherr et al. "Modern post-mortem imaging: an update on recent developments". In: *Forensic Sciences Research* 2.2 (2017), pp. 52–64. DOI: 10.1080/20961790.2017.1330738 (cit. on pp. 13, 92, 99).

[46] S. G. Ross et al. "Postmortem CT Angiography: Capabilities and Limitations in Traumatic and Natural Causes of Death". In: *RadioGraphics* 34.3 (2014), pp. 830–846. DOI: 10.1148/rg.343115169 (cit. on p. 14).

[47] K. Iizuka et al. "Feasibility of resuscitation contrast-enhanced postmortem computed tomography using cardiopulmonary resuscitation technique with chest compression immediately after death". In: *SpringerPlus* 2.1 (2013), p. 663. DOI: 10.1186/2193-1801-2-663 (cit. on p. 14).

[48] B. Webb et al. "Post-mortem MR angiography: Quantitative investigation and intravascular retention of perfusates in ex situ porcine hearts". In: *International Journal of Legal Medicine* 132.2 (2018), pp. 579–587. DOI: 10.1007/s00414-017-1763-7 (cit. on pp. 14, 18, 65, 99, 117, 145).

[49] S. Grabherr et al. "Postmortem angiography: Review of former and current methods". In: *American Journal of Roentgenology* 188 (2007), pp. 832–838. DOI: 10.2214/ajr.06.0787 (cit. on pp. 14, 65, 101).

[50] G. Inokuchi et al. "The utility of postmortem computed tomography selective coronary angiography in parallel with autopsy". In: *Forensic Science, Medicine, and Pathology* 9 (2013), pp. 506–514. DOI: 10.1007/s12024-013-9473-z (cit. on pp. 14, 100).

[51] C. Jackowski et al. "Virtopsy: postmortem imaging of the human heart in situ using MSCT and MRI". In: *Forensic Science International* 149.1 (2005), pp. 11–23. DOI: 10.1016/j.forsciint.2004.05.019 (cit. on pp. 14, 16).

[52] C. Bruguier et al. "Multi-phase postmortem CT angiography: Recognizing technique-related artefacts and pitfalls". In: *International Journal of Legal Medicine* 127 (2013), pp. 639–652. DOI: 10.1007/s00414-013-0840-9 (cit. on pp. 14–16).

[53] G. Rutty et al. "The effect on toxicology, biochemistry and immunology investigations by the use of targeted post-mortem computed tomography angiography". In: *Forensic Science International* 225.1 (2013). Postmortem Imaging, pp. 42–47. DOI: 10.1016/j.forsciint.2012.05.012 (cit. on p. 15).

[54] C. Palmiere et al. "Detection of coronary thrombosis after multi-phase postmortem CT-angiography". In: *Legal Medicine* 15.1 (2013), pp. 12–18. DOI: 10.1016/j.legalmed.2012.08.005 (cit. on p. 15).

[55] S. Grabherr et al. "Postmortem biochemistry performed on vitreous humor after postmortem CT-angiography". In: *Legal Medicine* 14.6 (2012), pp. 297–303. DOI: 10.1016/j.legalmed.2012.04.010 (cit. on p. 15).

[56] C. Palmiere, S. Grabherr, and M. Augsburger. "Postmortem computed tomography angiography, contrast medium administration and toxicological analyses in urine". In: *Legal Medicine* 17.3 (2014), pp. 157–162. DOI: 10.1016/j.legalmed.2014.12.005 (cit. on p. 15).

[57] S. Grabherr et al. "Advances in post-mortem CT-angiography." In: *The British Journal of Radiology* 87.1036 (2013), p. 20130488. DOI: 10.1259/bjr.20130488 (cit. on p. 15).

[58] T. Ruder, M. Thali, and G. Hatch. "Essentials of forensic post-mortem MR imaging in adults." In: *The British Journal of Radiology* 87.1036 (2014), p. 20130567. DOI: 10.1259/bjr.20130567 (cit. on pp. 16, 17).

[59] K. Michaud et al. "Postmortem imaging of sudden cardiac death". In: *International Journal of Legal Medicine* 128 (2014), pp. 127–137. DOI: 10.1007/s00414-013-0819-6 (cit. on pp. 16, 20, 22).

[60] A. Christe et al. "Clinical radiology and postmortem imaging (Virtopsy) are not the same: Specific and unspecific postmortem signs". In: *Legal Medicine* 12.5 (2010), pp. 215–222. DOI: 10.1016/j.legalmed.2010.05.005 (cit. on p. 16).

[61] T. D. Ruder et al. "The influence of body temperature on image contrast in post mortem MRI". In: *European Journal of Radiology* 81 (2012), pp. 1366–1370. DOI: 10.1016/j.ejrad.2011.02.062 (cit. on p. 16).

[62] N. Adolphi et al. "Determining the temperature-dependence of tissue relaxation times (T1 and T2) for prospective optimization of post-mortem magnetic resonance (PMMR) image contrast". In: *Journal of Forensic Radiology and Imaging* 1.2 (2013), p. 80. DOI: 10.1016/j.jofri.2013.03.002 (cit. on p. 16).

[63] C. Birkl et al. "Temperature-induced changes of magnetic resonance relaxation times in the human brain: A postmortem study". In: *Magnetic Resonance in Medicine* 71.4 (2014), pp. 1575–1580. DOI: 10.1002/mrm.24799 (cit. on pp. 16, 17, 109).

[64] W.-D. Zech et al. "Temperature dependence of postmortem MR quantification for soft tissue discrimination". In: *European Radiology* 25.8 (2015), pp. 2381–9. DOI: 10.1007/s00330-015-3588-4 (cit. on pp. 16, 17, 20, 54, 55, 100, 103, 111, 119, 120).

[65] A. Persson et al. "Temperature-corrected postmortem 3-T MR quantification of histopathological early acute and chronic myocardial infarction: a feasibility study". In: *International Journal of Legal Medicine* 132.2 (2018), pp. 541–549. DOI: 10.1007/s00414-017-1614-6 (cit. on pp. 16, 17, 20, 21, 23, 24, 42, 107–110, 121).

[66] T. Nelson and S. Tung. "Temperature dependence of proton relaxation times in vitro". In: *Magnetic Resonance Imaging* 5.3 (1987), pp. 189–199. DOI: 10.1016/0730-725X(87)90020-8 (cit. on p. 16).

[67] T. Kobayashi et al. "Characteristic signal intensity changes on postmortem magnetic resonance imaging of the brain". In: *Japanese Journal of Radiology* 28.1 (2010), pp. 8–14. DOI: 10.1007/s11604-009-0373-9 (cit. on p. 16).

[68] T. Kobayashi et al. "Optimization of Inversion Time for Postmortem Short-tau Inversion Recovery (STIR) MR Imaging". In: *Magnetic Resonance in Medical Sciences* 13.2 (2014), pp. 67–72. DOI: 10.2463/mrms.2013-0046 (cit. on p. 16).

[69] S. Keller et al. "Postmortem MR diffusion-weighted imaging of the liver: time-behavior of the hepatic apparent diffusion coefficient in the early death interval". In: *International Journal of Legal Medicine* 132.1 (2018), pp. 263–268. DOI: 10.1007/s00414-017-1685-4 (cit. on pp. 16, 113).

[70] A. Bayat, D. Koopmanschap, and W. Klein. "1.10. Postmortem interval estimation: Value of postmortem cerebral CT". In: *Journal of Forensic Radiology and Imaging* 2.2 (2014), p. 98. DOI: 10.1016/j.jofri.2014.02.013 (cit. on p. 16).

[71] J. Bonzon et al. "Rigor mortis at the myocardium investigated by post-mortem magnetic resonance imaging". In: *Forensic Science International* 257 (2015), pp. 93–97. DOI: 10.1016/j.forsciint.2015.07.039 (cit. on p. 16).

[72] O. J. Arthurs et al. "Diffusion-weighted perinatal postmortem magnetic resonance imaging as a marker of postmortem interval". In: *European Radiology* 25.5 (2015), pp. 1399–1406. DOI: 10.1007/s00330-014-3525-y (cit. on p. 16).

[73] J. Wang et al. "Estimation of Postmortem Interval Using the Radiological Techniques, Computed Tomography: A Pilot Study". In: *Journal of Forensic Science and Medicine* 3.1 (2017), pp. 1–8. DOI: 10.4103/jfsm.jfsm_4_17 (cit. on p. 16).

[74] C. Jackowski et al. "Quantitative MRI in Isotropic Spatial Resolution for Forensic Soft Tissue Documentation. Why and How?*". In: *Journal of Forensic Sciences* 56.1 (2011), pp. 208–215. DOI: 10.1111/j.1556-4029.2010.01547.x (cit. on p. 16).

[75] A. Droby et al. "A human post-mortem brain model for the standardization of multi-centre MRI studies". In: *NeuroImage* 110 (2015), pp. 11–21. DOI: 10.1016/j.neuroimage.2015.01.028 (cit. on p. 17).

[76] C. Langkammer et al. "Quantitative MR Imaging of Brain Iron: A Postmortem Validation Study". In: *Radiology* 257.2 (2010), pp. 455–462. DOI: 10.1148/radiol.10100495 (cit. on p. 17).

[77] C. Langkammer et al. "Quantitative susceptibility mapping (QSM) as a means to measure brain iron? A post mortem validation study". In: *NeuroImage* 62.3 (2012), pp. 1593–1599. DOI: 10.1016/j.neuroimage.2012.05.049 (cit. on p. 17).

[78] K. Schmierer et al. "Quantitative magnetic resonance of postmortem multiple sclerosis brain before and after fixation". In: *Magnetic Resonance in Medicine* 59.2 (2008), pp. 268–277. DOI: 10.1002/mrm.21487 (cit. on p. 17).

[79] K. Schmierer et al. "Diffusion tensor imaging of post mortem multiple sclerosis brain". In: *NeuroImage* 35.2 (2007), pp. 467–477. DOI: 10.1016/j.neuroimage.2006.12.010 (cit. on p. 17).

[80] A. M. Evia et al. "Ex-vivo quantitative susceptibility mapping of human brain hemispheres". In: *PLOS ONE* 12.12 (2017), pp. 1–16. DOI: 10.1371/journal.pone.0188395 (cit. on p. 17).

[81] K. Tashiro et al. "Cerebral Relaxation Times from Postmortem MR Imaging of Adults". In: *Magnetic Resonance in Medical Sciences* 14.1 (2015), pp. 51–56. DOI: 10.2463/mrms.2013-0126 (cit. on p. 17).

[82] C. Jackowski et al. "Magnetic resonance imaging goes postmortem: noninvasive detection and assessment of myocardial infarction by postmortem MRI." In: *European Radiology* 21 (2011), pp. 70–8. DOI: 10.1007/s00330-010-1884-6 (cit. on p. 17).

[83] N. Schwendener et al. "Temperature-corrected post-mortem 1.5 T MRI quantification of non-pathologic upper abdominal organs". In: *International Journal of Legal Medicine* 131.5 (2017), pp. 1369–1376. DOI: 10.1007/s00414-017-1622-6 (cit. on p. 17).

[84] W.-D. Zech et al. "Postmortem MR quantification of the heart for characterization and differentiation of ischaemic myocardial lesions". In: *European Radiology* 25.7 (2015), pp. 2067–2073. DOI: 10.1007/s00330-014-3582-2 (cit. on pp. 17, 20, 21, 23, 42, 58, 107, 121, 122).

[85] W.-D. Zech et al. "Postmortem quantitative 1.5-T MRI for the differentiation and characterization of serous fluids, blood, CSF, and putrefied CSF". In: *International Journal of Legal Medicine* 129.5 (2015), pp. 1127–1136. DOI: 10.1007/s00414-015-1218-y (cit. on pp. 17, 102, 108–110).

[86] S. Winklhofer et al. "Post-mortem cardiac diffusion tensor imaging: detection of myocardial infarction and remodeling of myofiber architecture". In: *European Radiology* 24.11 (2014), pp. 2810–2818. DOI: 10.1007/s00330-014-3322-7 (cit. on pp. 17, 20, 21, 27, 107, 113).

[87] H. J. A. Crooijmans et al. "Feasibility of quantitative diffusion imaging of the heart in post-mortem MR". In: *Journal of Forensic Radiology and Imaging* 1.3 (2013), pp. 124–128. DOI: 10.1016/j.jofri.2013.05.009 (cit. on pp. 17, 27).

[88] H. Saitou et al. "Myocardial Relaxation Times Measured from Postmortem Magnetic Resonance Imaging in Adult Humans". In: *Journal of Forensic Radiology and Imaging* 10 (2017), pp. 23–28. DOI: 10.1016/j.jofri.2017.07.001 (cit. on pp. 17, 42).

[89] *Synthetic MR products website: https://www.syntheticmr.com* (cit. on pp. 17, 107, 110).

[90] J. B. M. Warntjes et al. "Rapid magnetic resonance quantification on the brain: Optimization for clinical usage". In: *Magnetic Resonance in Medicine* 60.2 (2008), pp. 320–329. DOI: 10.1002/mrm.21635 (cit. on pp. 17, 107, 108, 110).

[91] C. Bruguier et al. "Postmortem magnetic resonance imaging of the heart ex situ: development of technical protocols". In: *International Journal of Legal Medicine* 129.3 (2015), pp. 559–67. DOI: 10.1007/s00414-014-1058-1 (cit. on pp. 18, 104).

[92] B. Webb et al. "Temperature dependence of viscosity, relaxation times (T1, T2) and simulated contrast for potential perfusates in post-mortem MR angiography (PMMRA)". In: *International Journal of Legal Medicine* 131.3 (2017), pp. 739–749. DOI: 10.1007/s00414-016-1482-5 (cit. on pp. 18, 45, 99, 100, 105, 145).

[93] T. Ruder et al. "Whole Body Postmortem Magnetic Resonance Angiography". In: *Journal of Forensic Sciences* 57 (2012), pp. 778–782. DOI: 10.1111/j.1556-4029.2011.02037.x (cit. on p. 19).

[94] P. J. Laberke et al. "Fast three-dimensional whole-body post-mortem magnetic resonance angiography". In: *Journal of Forensic Radiology and Imaging* 10.Supplement C (2017), pp. 41–46. DOI: 10.1016/j.jofri.2017.08.002 (cit. on p. 19).

[95] K. Michaud et al. "Evaluation of postmortem MDCT and MDCT-angiography for the investigation of sudden cardiac death related to atherosclerotic coronary artery disease". In: *International Journal of Cardiovascular Imaging* 28 (2012), pp. 1807–1822. DOI: 10.1007/s10554-012-0012-x (cit. on pp. 20–22).

[96] O. Arthurs et al. "Diagnostic accuracy of post-mortem MRI for thoracic abnormalities in fetuses and children". In: *European Radiology* 24.11 (2014), pp. 2876–2884. DOI: 10.1007/s00330-014-3313-8 (cit. on p. 20).

[97] S. Thayyil et al. "Post-mortem MRI versus conventional autopsy in fetuses and children: a prospective validation study". In: *The Lancet* 382.9888 (2013), pp. 223–233. DOI: 10.1016/S0140-6736(13)60134-8 (cit. on p. 20).

[98] A. M. Taylor et al. "Postmortem cardiovascular magnetic resonance imaging in fetuses and children: A masked comparison study with conventional autopsy". In: *Circulation* 129 (2014), pp. 1937–1944. DOI: 10.1161/circulationaha.113.005641 (cit. on p. 20).

[99] I. S. D. Roberts et al. "Post-mortem imaging as an alternative to autopsy in the diagnosis of adult deaths: A validation study". In: *The Lancet* 379 (2012), pp. 136–142. DOI: 10.1016/s0140-6736(11)61483-9 (cit. on p. 20).

[100] C. Chevallier et al. "Postmortem computed tomography angiography vs. conventional autopsy: Advantages and inconveniences of each method". In: *International Journal of Legal Medicine* 127 (2013), pp. 981–989. DOI: 10.1007/s00414-012-0814-3 (cit. on pp. 20–22).

[101] B. Morgan et al. "Accuracy of targeted post-mortem computed tomography coronary angiography compared to assessment of serial histological sections". In: *International Journal of Legal Medicine* 127 (2013), pp. 809–817. DOI: 10.1007/s00414-012-0790-7 (cit. on p. 20).

[102] T. D. Ruder et al. "Assessment of coronary artery disease by post-mortem cardiac MR." In: *European journal of radiology* 81 (2012), pp. 2208–14. DOI: 10.1016/j.ejrad.2011.06.042 (cit. on p. 20).

[103] S. E. Westphal et al. "Contrast-enhanced postmortem computed tomography in clinical pathology: enhanced value of 20 clinical autopsies". In: *Human Pathology* 45.9 (2014), pp. 1813–1823. DOI: 10.1016/j.humpath.2014.05.007 (cit. on p. 20).

[104] A. Eriksson et al. "Diagnostic accuracy of postmortem imaging vs autopsy—A systematic review". In: *European Journal of Radiology* 89 (2017), pp. 249–269. DOI: 10.1016/j.ejrad.2016.08.003 (cit. on p. 20).

[105] J. Vanhaebost et al. "Diagnosis of myocardial ischemia combining multiphase post-mortem CT-angiography, histology, and postmortem biochemistry". In: *La Radiologia Medica* 122.2 (2017), pp. 95–105. DOI: 10.1007/s11547-016-0698-2 (cit. on pp. 21, 22, 42, 120, 122).

[106] S. Sabatasso et al. "Visualization of Myocardial Infarction in Postmortem Multiphase Computed Tomography Angiography: A Feasibility Study". In: *The American Journal of Forensic Medicine and Pathology* (2018). DOI: 10.1097/PAF.0000000000000372 (cit. on pp. 21, 22, 42, 122).

[107] C. Jackowski et al. "Post-mortem cardiac 3-T magnetic resonance imaging: Visualization of sudden cardiac death?" In: *Journal of the American College of Cardiology* 62 (2013), pp. 617–629. DOI: 10.1016/j.jacc.2013.01.089 (cit. on pp. 21, 23, 24, 121).

[108] G. J. Stanisz et al. "T1, T2 relaxation and magnetization transfer in tissue at 3T". In: *Magnetic Resonance in Medicine* 54.3 (2005), pp. 507–512. DOI: 10.1002/mrm.20605 (cit. on p. 23).

[109] M. A. Bernstein, K. F. King, and X. J. Zhou. *Handbook of MRI Pulse Sequences*. Burlington, USA: Elsevier Academic Press, 2004 (cit. on pp. 25, 26, 58).

[110] A. J. Wheaton and M. Miyazaki. "Non-contrast enhanced MR angiography: Physical principles". In: *Journal of Magnetic Resonance Imaging* 36.2 (2012), pp. 286–304. DOI: 10.1002/jmri.23641 (cit. on pp. 25, 26).

[111] D. O h-Ici et al. "T1 mapping in ischaemic heart disease". In: *European Heart Journal - Cardiovascular Imaging* 15.6 (2014), pp. 597–602. DOI: 10.1093/ehjci/jeu024 (cit. on p. 26).

[112] R. Metere et al. "Simultaneous Quantitative MRI Mapping of T1, T2* and Magnetic Susceptibility with Multi-Echo MP2RAGE". In: *PLOS ONE* 12.1 (2017), pp. 1–28. DOI: 10.1371/journal.pone.0169265 (cit. on p. 26).

[113] E. Dall'Armellina et al. "Cardiovascular magnetic resonance by non contrast T1-mapping allows assessment of severity of injury in acute myocardial infarction". In: *Journal of Cardiovascular Magnetic Resonance* 14.1 (2012), p. 15. DOI: 10.1186/1532-429X-14-15 (cit. on p. 27).

[114] D. Carrick et al. "Prognostic significance of infarct core pathology revealed by quantitative non-contrast in comparison with contrast cardiac magnetic resonance imaging in reperfused ST-elevation myocardial infarction survivors". In: *European Heart Journal* 37.13 (2016), pp. 1044–1059. DOI: 10.1093/eurheartj/ehv372 (cit. on p. 27).

[115] M. Salerno and C. M. Kramer. "Advances in Parametric Mapping with Cardiac Magnetic Resonance Imaging". In: *JACC: Cardiovascular imaging* 6.7 (2013), pp. 806–822. DOI: 10.1016/j.jcmg.2013.05.005 (cit. on p. 27).

[116] D. Verhaert et al. "Direct T2 Quantification of Myocardial Edema in Acute Ischemic Injury". In: *JACC: Cardiovascular imaging* 4.3 (2011), pp. 269–278. DOI: 10.1016/j.jcmg.2010.09.023 (cit. on pp. 27, 111).

[117] P. Thavendiranathan et al. "Improved Detection of Myocardial Involvement in Acute Inflammatory Cardiomyopathies Using T2 MappingClinical Perspective". In: *Circulation: Cardiovascular Imaging* 5.1 (2012), pp. 102–110. DOI: 10.1161/CIRCIMAGING.111.967836 (cit. on p. 27).

[118] P. K. Kim et al. "Myocardial T1 and T2 Mapping: Techniques and Clinical Applications". In: *Korean J Radiol* 18.1 (2017), pp. 113–131. DOI: 10.3348/kjr.2017.18.1.113 (cit. on p. 27).

[119] C. Nguyen et al. "In vivo cardiac diffusion MRI: second order motion compensated diffusion-prepared balanced steady state free precession (SOMOCO Diff Prep bSSFP)". In: *Journal of Cardiovascular Magnetic Resonance* 15 (Supp).1 (2013), P6. DOI: 10.1186/1532-429X-15-S1-P6 (cit. on p. 27).

[120] C. Mekkaoui et al. "Diffusion MRI in the heart". In: *NMR in Biomedicine* 30.3 (2017), e3426. DOI: 10.1002/nbm.3426 (cit. on pp. 27, 41, 112).

[121] E. X. Wu et al. "MR diffusion tensor imaging study of postinfarct myocardium structural remodeling in a porcine model". In: *Magnetic Resonance in Medicine* 58.4 (2007), pp. 687–695. DOI: 10.1002/mrm.21350 (cit. on p. 27).

[122] D. E. Sosnovik et al. "Diffusion Spectrum MRI Tractography Reveals the Presence of a Complex Network of Residual Myofibers in Infarcted MyocardiumCLINICAL PERSPECTIVE". In: *Circulation: Cardiovascular Imaging* 2.3 (2009), pp. 206–212. DOI: 10.1161/CIRCIMAGING.108.815050 (cit. on p. 27).

[123] C. Rorden, H.-O. Karnath, and L. Bonilha. "Improving Lesion-Symptom Mapping". In: *Journal of Cognitive Neuroscience* 19.7 (2007), pp. 1081–1088. DOI: 10.1162/jocn.2007.19.7.1081 (cit. on p. 32).

[124] O. Dietrich et al. "Measurement of signal-to-noise ratios in MR images: Influence of multichannel coils, parallel imaging, and reconstruction filters". In: *Journal of Magnetic Resonance Imaging* 26.2 (2007), pp. 375–385. DOI: 10.1002/jmri.20969 (cit. on p. 33).

[125] O. Dietrich et al. "Influence of multichannel combination, parallel imaging and other reconstruction techniques on MRI noise characteristics". In: *Magnetic Resonance Imaging* 26.6 (2008), pp. 754–762. DOI: 10.1016/j.mri.2008.02.001 (cit. on pp. 33, 34).

[126] P. Hou et al. "Phase-Sensitive T1 Inversion Recovery Imaging: A Time-Efficient Interleaved Technique for Improved Tissue Contrast in Neuroimaging". In: *American Journal of Neuroradiology* 26.6 (2005), pp. 1432–1438 (cit. on pp. 34, 104).

[127] I. Koktzoglou et al. "Three-dimensional Black-Blood MR Imaging of Carotid Arteries with Segmented Steady-State Free Precession: Initial Experience". In: *Radiology* 243.1 (2007), pp. 220–228. DOI: 10.1148/radiol.2431060310 (cit. on p. 34).

[128] P. S. Foundation. *Python Language Reference, Version 2.7*. Available at http://www.python.org. 2010 (cit. on pp. 34, 40, 68, 69).

[129] F. Crete et al. "The blur effect: perception and estimation with a new no-reference perceptual blur metric". In: *Human Vision and Electronic Imaging XII*. Ed. by B. E. Rogowitz, T. N. Pappas, and S. J. Daly. SPIE, Feb. 2007. DOI: 10.1117/12.702790 (cit. on pp. 34, 35, 64).

[130] A. Bustin et al. "Impact of denoising on precision and accuracy of saturation recovery-based myocardial T1 mapping". In: *Journal of Magnetic Resonance Imaging* 46.5 (2017), pp. 1377–1388. DOI: 10.1002/jmri.25684 (cit. on pp. 36–38, 114).

[131] E. Garyfallidis et al. "Dipy, a library for the analysis of diffusion MRI data." In: *Frontiers in Neuroinformatics* 8.8 (2014), p. 8. DOI: 10.3389/fninf.2014.00008 (cit. on pp. 36–38, 41, 77).

[132] P. Coupé et al. "An Optimized Blockwise Nonlocal Means Denoising Filter for 3-D Magnetic Resonance Images". In: *IEEE Transactions on Medical Imaging* 27.4 (2008), pp. 425–441. DOI: 10.1109/TMI.2007.906087 (cit. on pp. 37, 38).

[133] M.-X. Zhou et al. "Evaluation of Non-Local Means Based Denoising Filters for Diffusion Kurtosis Imaging Using a New Phantom". In: *PLOS ONE* 10.2 (2015), pp. 1–15. DOI: 10.1371/journal.pone.0116986 (cit. on p. 37).

[134] N. Wiest-Daesslé et al. "Non-Local Means Variants for Denoising of Diffusion-Weighted and Diffusion Tensor MRI". In: *Medical Image Computing and Computer-Assisted Intervention – MICCAI 2007*. Ed. by N. Ayache, S. Ourselin, and A. Maeder. Berlin, Heidelberg: Springer Berlin Heidelberg, 2007, pp. 344–351. DOI: 10.1007/978-3-540-75759-7_42 (cit. on p. 37).

[135] A. Buades, B. Coll, and J. M. Morel. "A non-local algorithm for image denoising". In: *2005 IEEE Computer Society Conference on Computer Vision and Pattern Recognition (CVPR'05)*. Vol. 2. June 2005, pp. 60–65. DOI: 10.1109/CVPR.2005.38 (cit. on pp. 37, 38).

[136] P. Coupé et al. "Adaptive multiresolution non-local means filter for three-dimensional magnetic resonance image denoising". English. In: *IET Image Processing* 6 (5 2012), 558–568(10). DOI: 10.1049/iet-ipr.2011.0161 (cit. on pp. 37, 38).

[137] P. Perona and J. Malik. "Scale-space and edge detection using anisotropic diffusion". In: *IEEE Transactions on Pattern Analysis and Machine Intelligence* 12.7 (1990), pp. 629–639. DOI: 10.1109/34.56205 (cit. on p. 38).

[138] L. I. Rudin, S. Osher, and E. Fatemi. "Nonlinear total variation based noise removal algorithms". In: *Physica D: Nonlinear Phenomena* 60.1 (1992), pp. 259–268. DOI: 10.1016/0167-2789(92)90242-F (cit. on p. 38).

[139] M. Descoteaux et al. "Impact of Rician Adapted Non-Local Means Filtering on HARDI". In: *Medical Image Computing and Computer-Assisted Intervention – MICCAI 2008*. Ed. by D. Metaxas et al. Berlin, Heidelberg: Springer Berlin Heidelberg, 2008, pp. 122–130. DOI: 10.1007/978-3-540-85990-1_15 (cit. on p. 38).

[140] G. Palma et al. "A Novel Multiparametric Approach to 3D Quantitative MRI of the Brain". In: *PLOS ONE* 10.8 (2015), e0134963. DOI: 10.1371/journal.pone.0134963 (cit. on p. 38).

[141] P. A. Yushkevich et al. "User-guided 3D active contour segmentation of anatomical structures: Significantly improved efficiency and reliability." In: *NeuroImage* 31.3 (2006), pp. 1116–28. DOI: 10.1016/j.neuroimage.2006.01.015 (cit. on pp. 40, 68).

[142] R Development Core Team. *R: A Language and Environment for Statistical Computing*. ISBN 3-900051-07-0. R Foundation for Statistical Computing. Vienna, Austria, 2008 (cit. on p. 40).

[143] J. Pinheiro et al. *nlme: Linear and Nonlinear Mixed Effects Models*. R package version 3.1-131. 2017 (cit. on p. 40).

[144] M. Newville et al. *LMFIT: Non-Linear Least-Square Minimization and Curve-Fitting for Python*. Sept. 2014. DOI: 10.5281/zenodo.11813 (cit. on p. 40).

[145] P. Tofts. *Quantitative MRI of the Brain*. Chichester, UK: John Wiley & Sons Ltd., 2003 (cit. on pp. 40, 114).

[146] C. F. Maier et al. "T2 quantitation of articular cartilage at 1.5 T". In: *Journal of Magnetic Resonance Imaging* 17.3 (2003), pp. 358–364. DOI: 10.1002/jmri.10263 (cit. on p. 40).

[147] T. J. Mosher, Y. Liu, and C. M. Torok. "Functional cartilage MRI T2 mapping: evaluating the effect of age and training on knee cartilage response to running". In: *Osteoarthritis and Cartilage* 18.3 (2010), pp. 358–364. DOI: 10.1016/j.joca.2009.11.011 (cit. on p. 40).

[148] E. O. Stejskal and J. E. Tanner. "Spin Diffusion Measurements: Spin Echoes in the Presence of a Time-Dependent Field Gradient". In: *The Journal of Chemical Physics* 42.1 (1965), pp. 288–292. DOI: 10.1063/1.1695690 (cit. on p. 41).

[149] P. J. Basser, J. Mattiello, and D. LeBihan. "MR diffusion tensor spectroscopy and imaging." In: *Biophysical Journal* 66.1 (1994), pp. 259–267. DOI: 10.1016/s0006-3495(94)80775-1 (cit. on pp. 41, 42).

[150] P. J. Basser and C. Pierpaoli. "Microstructural and physiological features of tissues elucidated by quantitative-diffusion-tensor MRI". In: *Journal of Magnetic Resonance* 213.2 (2011), pp. 560–570. DOI: doi.org/10.1016/j.jmr.2011.09.022 (cit. on p. 42).

[151] P. S. Foundation. *Python Language Reference, Version 3.4*. Available at http://www.python.org. 2014 (cit. on p. 42).

[152] K. Marstal et al. "SimpleElastix: A user-friendly, multi-lingual library for medical image registration". In: *International Workshop on Biomedical Image Registration (WBIR)*. Ed. by Julia Schnabel and Kensaku Mori. IEEE Conference on Computer Vision and Pattern Recognition Workshops. Las Vegas, Nevada, USA, July 2016, 574–582. DOI: 10.1109/cvprw.2016.78 (cit. on pp. 42, 79).

[153] C. Jackowski et al. "Reduction of postmortem angiography-induced tissue edema by using polyethylene glycol as a contrast agent dissolver". In: *Journal of Forensic Sciences* 51.5 (2006), pp. 1134–1137. DOI: 10.1111/j.1556-4029.2006.00207.x (cit. on pp. 45, 49, 99, 100).

[154] C. Jackowski, A. Persson, and M. J. Thali. "Whole body postmortem angiography with a high viscosity contrast agent solution using poly ethylene glycol as contrast agent dissolver". In: *Journal of Forensic Sciences* 53 (2008), pp. 465–468. DOI: 10.1111/j.1556-4029.2008.00673.x (cit. on p. 45).

[155] J. Kestin, M. Sokolov, and W. A. Wakeham. "Viscosity of Liquid Water in the Range -8°C to 150°C". In: *Journal of Physical and Chemical Reference Data* 7.3 (1978), pp. 941–8. DOI: 10.1063/1.555581 (cit. on pp. 46, 48).

[156] J. Kruisz. "Temperaturabhängikeit der Relaxivität und Relaxationszeiten für post-mortem MRT". Master Thesis. Graz University of Technology, 2013 (cit. on pp. 46, 48, 49, 52–55, 102, 108, 109).

[157] J. Kruisz et al. "Investigation of temperature dependence of tissue relaxation parameters for post-mortem imaging". In: *International Society of Magnetic Resonance in Medicine*. Salt Lake City, 2013, p. 4968 (cit. on pp. 46, 48, 49, 52–55, 58, 102, 105).

[158] T. Mezger. *Rheology Handbook: For Users of Rotational And Oscillatory Rheometers*. 3rd. Hannover: Vincentz Network, 2011 (cit. on p. 48).

[159] A. Tinguely and T. Wantz. "TRM et imagerie forensique: Proportion du mélange huile-produit de contraste en angiographie post-mortem". MA thesis. 2010 (cit. on pp. 49, 100).

[160] J. T. Dodge et al. "Lumen diameter of normal human coronary arteries. Influence of age, sex, anatomic variation, and left ventricular hypertrophy or dilation". In: *Circulation* 86.1 (1992), pp. 232–46. DOI: 10.1161/01.cir.86.1.232 (cit. on pp. 58, 104).

[161] D. Mattes et al. "PET-CT image registration in the chest using free-form deformations". In: *IEEE Transactions on Medical Imaging* 22.1 (2003), pp. 120–128. DOI: 10.1109/TMI.2003.809072 (cit. on p. 68).

[162] M. Styner et al. "Parametric estimate of intensity inhomogeneities applied to MRI." In: *IEEE transactions on medical imaging* 19 (2000), pp. 153–65. DOI: 10.1109/42.845174 (cit. on p. 68).

[163] S. Klein et al. "elastix: A Toolbox for Intensity-Based Medical Image Registration". In: *IEEE Transactions on Medical Imaging* 29.1 (2010), pp. 196–205. DOI: 10.1109/TMI.2009.2035616 (cit. on p. 79).

[164] S. J. Crick et al. "Anatomy of the pig heart : comparisons with normal human cardiac structure". In: *Journal of Anatomy* 193.1 (1998), pp. 105–119. DOI: 10.1046/j.1469-7580.1998.19310105.x (cit. on p. 80).

[165] J. T. Ortiz-Pérez et al. "Correspondence Between the 17-Segment Model and Coronary Arterial Anatomy Using Contrast-Enhanced Cardiac Magnetic Resonance Imaging". In: *JACC: Cardiovascular Imaging* 1.3 (2008), pp. 282–293. DOI: 10.1016/j.jcmg.2008.01.014 (cit. on p. 81).

[166] P. Mukherjee et al. "Diffusion Tensor MR Imaging and Fiber Tractography: Technical Considerations". In: *American Journal of Neuroradiology* 29.5 (2008), pp. 843–852. DOI: 10.3174/ajnr.A1052 (cit. on p. 82).

[167] G. I. Orsmond and E. S. Cohn. "The Distinctive Features of a Feasibility Study: Objectives and Guiding Questions." eng. In: *OTJR : occupation, participation and health* 35 (3 2015), pp. 169–77. DOI: 10.1177/1539449215578649 (cit. on p. 93).

[168] S. Grabherr et al. "Application of contrast media in postmortem imaging (CT and MRI)". In: *La Radiologia Medica* 120.9 (2015), pp. 824–34. DOI: 10.1002/cmmi.425 (cit. on pp. 99, 100, 122).

[169] Z. Obermeyer, J. K. Samra, and S. Mullainathan. "Individual differences in normal body temperature: longitudinal big data analysis of patient records". In: *BMJ* 359 (2017). DOI: 10.1136/bmj.j5468 (cit. on p. 100).

[170] L. Claesson-Welsh. "Vascular permeability - The Essentials". In: *Upsala Journal of Medical Sciences* 120 (2015), pp. 135–143. DOI: 10.3109/03009734.2015.1064501 (cit. on p. 101).

[171] T. Berquist, ed. *MRI of the Musculoskeletal System*. 6th. Lippincott Williams & Wilkins, 2013 (cit. on p. 106).

[172] D. R. Messroghli et al. "Modified Look-Locker inversion recovery (MOLLI) for high-resolution T1 mapping of the heart." eng. In: *Magnetic Resonance in Medicine* 52 (1 2004), pp. 141–6. DOI: 10.1002/mrm.20110 (cit. on p. 107).

[173] P. Kellman and M. S. Hansen. "T1-mapping in the heart: accuracy and precision". In: *Journal of Cardiovascular Magnetic Resonance* 16.1 (2014), p. 2. DOI: 10.1186/1532-429X-16-2 (cit. on pp. 108, 110).

[174] K. Chow et al. "Saturation recovery single-shot acquisition (SASHA) for myocardial T1 mapping". In: *Magnetic Resonance in Medicine* 71.6 (2014), pp. 2082–2095. DOI: 10.1002/mrm.24878 (cit. on p. 108).

[175] S. Weingärtner et al. "Myocardial T1-mapping at 3T using saturation-recovery: reference values, precision and comparison with MOLLI". In: *Journal of Cardiovascular Magnetic Resonance* 18.1 (2016), p. 84. DOI: 10.1186/s12968-016-0302-x (cit. on p. 108).

[176] T. Bjerner et al. "In and ex vivo MR evaluation of acute myocardial ischemia in pigs by determining R1 in steady state after the administration of the intravascular contrast agent NC100150 injection." eng. In: *Investigative radiology* 39 (8 2004), pp. 479–86. DOI: 10.1097/01.rli.0000128658.63611.b3 (cit. on p. 108).

[177] D. Dabir et al. "Reference values for healthy human myocardium using a T1 mapping methodology: results from the International T1 Multicenter cardiovascular magnetic resonance study". In: *Journal of Cardiovascular Magnetic Resonance* 16.1 (2014), p. 69. DOI: 10.1186/s12968-014-0069-x (cit. on p. 108).

[178] R. T. Constable et al. "Factors influencing contrast in fast spin-echo MR imaging." eng. In: *Magnetic Resonance Imaging* 10.4 (4 1992), pp. 497–511. DOI: 10.1016/0730-725x(92)90001-g (cit. on p. 108).

[179] R. Turner et al. "Optimised in vivo visualisation of cortical structures in the human brain at 3 T using IR-TSE". In: *Magnetic Resonance Imaging* 26.7 (2008). Proceedings of the International School on Magnetic Resonance and Brain Function, pp. 935–942. DOI: 10.1016/j.mri.2008.01.043 (cit. on pp. 108, 109).

[180] B. Baeßler et al. "A systematic evaluation of three different cardiac T2-mapping sequences at 1.5 and 3T in healthy volunteers". In: *European Journal of Radiology* 84.11 (2015), pp. 2161–2170. DOI: 10.1016/j.ejrad.2015.08.002 (cit. on p. 109).

[181] J. G. Cobb. "Measuring transver relaxation in myocardial tissue with 3T MRI". MA thesis. Nashville, Tennesse: Graduate School of Vanderbilt University, 2008 (cit. on p. 109).

[182] R. J. Dawe et al. "Postmortem MRI of Human Brain Hemispheres: T(2) Relaxation Times during Formaldehyde Fixation". In: *Magnetic Resonance in Medicine* 61.4 (2009), pp. 810–818. DOI: 10.1002/mrm.21909 (cit. on p. 110).

[183] M. I. Kettunen et al. "Effects of intracellular pH, blood, and tissue oxygen tension on T1-rho relaxation in rat brain". In: *Magnetic Resonance in Medicine* 48.3 (2002), pp. 470–477. DOI: 10.1002/mrm.10233 (cit. on p. 110).

[184] M. van Assen et al. "Cardiac magnetic resonance T1 reactivity in coronary artery disease". In: European Congress of Radiology. Vienna, Mar. 2018 (cit. on pp. 110, 121).

[185] L. Hanzhang et al. "Determining the longitudinal relaxation time (T1) of blood at 3.0 Tesla". In: *Magnetic Resonance in Medicine* 52.3 (2004), pp. 679–682. DOI: 10.1002/mrm.20178 (cit. on p. 111).

[186] A. B. Lakshmi et al. "A simple slide test to assess erythrocyte aggregation in acute ST-elevated myocardial infarction and acute ischemic stroke: its prognostic significance." eng. In: *Indian journal of pathology & microbiology* 54 (1 2011), pp. 63–9. DOI: 10.21276/sjams.2016.4.7.3 (cit. on p. 111).

[187] L. Woudstra et al. "Lymphocytic myocarditis occurs with myocardial infarction and coincides with increased inflammation, hemorrhage and instability in coronary artery atherosclerotic plaques". In: *International Journal of Cardiology* 232 (2017), pp. 53–62. DOI: 10.1016/j.ijcard.2017.01.052 (cit. on p. 111).

[188] R. Wassmuth et al. "Variability and homogeneity of cardiovascular magnetic resonance myocardial T2-mapping in volunteers compared to patients with edema". In: *Journal of Cardiovascular Magnetic Resonance* 15.1 (2013), p. 27. DOI: 10.1186/1532-429X-15-27 (cit. on p. 111).

[189] P. Montant et al. "MR imaging assessment of myocardial edema with T2 mapping". In: *Diagnostic and Interventional Imaging* 96.9 (2015), pp. 885–890. DOI: 10.1016/j.diii.2014.07.008 (cit. on p. 111).

[190] F. Calamante et al. "Early changes in water diffusion, perfusion, T1, and T2 during focal cerebral ischemia in the rat studied at 8.5 T". In: *Magnetic Resonance in Medicine* 41.3 (1999), pp. 479–485. DOI: 10.1002/(SICI)1522-2594(199903)41:3<479::AID-MRM9>3.0.CO;2-2 (cit. on p. 111).

[191] C. Jackowski, S. Grabherr, and N. Schwendener. "Pulmonary thrombembolism as cause of death on unenhanced postmortem 3T MRI". In: *European Radiology* 23 (2013), pp. 1266–1270. DOI: 10.1007/s00330-012-2728-3 (cit. on p. 111).

[192] A. Schilling et al. "Intracerebral pH affects the T2 relaxation time of brain tissue". In: *Neuroradiology* 44.12 (2002), pp. 968–972. DOI: 10.1007/s00234-002-0873-0 (cit. on p. 111).

[193] E. A. Louie et al. "Transverse Relaxation and Magnetization Transfer in Skeletal Muscle: Effect of pH". In: *Magnetic Resonance in Medicine* 61.3 (2009), pp. 560–569. DOI: 10.1002/mrm.21847 (cit. on p. 111).

[194] R. M. Dongaonkar et al. "Myocardial microvascular permeability, interstitial oedema, and compromised cardiac function". In: *Cardiovascular Research* 87.2 (2010), pp. 331–339. DOI: 10.1093/cvr/cvq145 (cit. on p. 112).

[195] S. M. Meyers et al. "Measuring water content using T2 relaxation at 3T: Phantom validations and simulations." eng. In: *Magnetic Resonance Imaging* 34 (3 2016), pp. 246–51. DOI: 10.1016/j.mri.2015.11.008 (cit. on p. 112).

[196] V. Chianca et al. "Diffusion tensor imaging in the musculoskeletal and peripheral nerve systems: from experimental to clinical applications". In: *European Radiology Experimental* 1.1 (2017), p. 12. DOI: 10.1186/s41747-017-0018-1 (cit. on p. 112).

[197] K. W. Muir et al. "Imaging of acute stroke". In: *The Lancet Neurology* 5.9 (2006), pp. 755–768. DOI: 10.1016/s1474-4422(06)70545-2 (cit. on p. 112).

[198] A. C. Alegiani et al. "Comprehensive analysis of early fractional anisotropy changes in acute ischemic stroke". In: *PLOS ONE* 12.11 (2017), pp. 1–11. DOI: 10.1371/journal.pone.0188318 (cit. on pp. 112, 121).

[199] D. Davis et al. "Rapid monitoring of changes in water diffusion coefficients during reversible ischemia in cat and rat brain". In: *Magnetic Resonance in Medicine* 31.4 (1994), pp. 454–460. DOI: 10.1002/mrm.1910310416 (cit. on p. 112).

[200] G. Barrio-Arranz et al. "Impact of MR Acquisition Parameters on DTI Scalar Indexes: A Tractography Based Approach". In: *PLOS ONE* 10.10 (2015), e0137905. DOI: 10.1371/journal.pone.0137905 (cit. on pp. 112, 113).

[201] R. Mazumder et al. "Diffusion Tensor Imaging of Healthy and Infarcted Porcine Hearts: Study on the Impact of Formalin Fixation". In: *Journal of Medical Imaging and Radiation Sciences* 47.1 (2016), pp. 74–85. DOI: 10.1016/j.jmir.2015.10.007 (cit. on pp. 113, 121).

[202] N. Stikov et al. "On the accuracy of T1 mapping: Searching for common ground". In: *Magnetic Resonance in Medicine* 73.2 (2015), pp. 514–522. DOI: 10.1002/mrm.25135 (cit. on p. 114).

[203] N. Ben-Eliezer, D. K. Sodickson, and T. K. Block. "Rapid and Accurate T2 Mapping from Multi Spin Echo Data Using Bloch-Simulation-Based Reconstruction". In: *Magnetic Resonance in Medicine* 73.2 (2015), pp. 809–817. DOI: 10.1002/mrm.25156 (cit. on p. 114).

[204] N. N. Lukzen et al. "The generating functions formalism for the analysis of spin response to the periodic trains of RF pulses. Echo sequences with arbitrary refocusing angles and resonance offsets." eng. In: *Journal of Magnetic Resonance* 196 (2 2009), pp. 164–9. DOI: 10.1016/j.jmr.2008.11.008 (cit. on p. 114).

[205] A. Schuster et al. "An isolated perfused pig heart model for the development, validation and translation of novel cardiovascular magnetic resonance techniques". In: *Journal of Cardiovascular Magnetic Resonance* 12.1 (2010), p. 53. DOI: 10.1186/1532-429x-12-53 (cit. on p. 115).

[206] W. Kim et al. "A porcine model of ischemic heart failure produced by intracoronary injection of ethyl alcohol". In: *Heart Vessels* 26.3 (2010), pp. 342–8. DOI: 10.1007/s00380-010-0022-3 (cit. on p. 115).

[207] Z. Q. Li et al. "Experimental study of relationship between intracoronary alcohol injection and the size of resultant myocardial infarct". In: *International Journal of Cardiology* 91.1 (2003), pp. 93–96. DOI: 10.1016/s0167-5273(02)00592-2 (cit. on p. 115).

List of publications

Peer-reviewed impact factor journal publications

1. B. Webb, T. Widek, S. Scheicher, T. Schwark, and R. Stollberger. "Post-mortem MR angiography: Quantitative investigation and intravascular retention of perfusates in ex situ porcine hearts". In: *International Journal of Legal Medicine* 132.2 (2018), pp. 579–587. DOI: 10.1007/s00414-017-1763-7

2. B. Webb, T. Widek, B. Neumayer, C. Bruguier, S. Scheicher, H. Sprenger, S. Grabherr, T. Schwark, and R. Stollberger. "Temperature dependence of viscosity, relaxation times (T1, T2) and simulated contrast for potential perfusates in post-mortem MR angiography (PMMRA)". In: *International Journal of Legal Medicine* 131.3 (2017), pp. 739–749. DOI: 10.1007/s00414-016-1482-5

3. B. Webb, A. Petrovic, M. Urschler, and A. Scheurer. "Assessment of fiducial markers to enable the co-registration of photographs and MRI data". In: *Forensic Science International* 248 (2015), pp. 148–153. DOI: 10.1016/j.forsciint.2014.12.027

Other peer-reviewed journal publications

1. S. Kerbacher, M. Pfeifer, B. Webb, and R. Riener-Hofer. "Clinical forensic imaging and fundamental rights in Austria". In: *Forensic Sciences Research* 2.2 (2017), pp. 65–74. DOI: 10.1080/20961790.2017.1328808

2. B. Webb and S. Scheicher. "Engaging police and community: The role of forensic practitioners in responding to abusive situations". In: *European Police Science and Research Bulletin* 13 (2015), pp. 37–42

3. R. Riener-Hofer, B. Webb, and E. Scheurer. "Forensigraphy: The integration of imaging techniques into the criminal justice system". In: *European Police Science and Research Bulletin* 11 (2014), pp. 47–56

Peer-reviewed conference abstracts

1. B. Webb, M. Urschler, M. Leoni, B. Neumayer, T. Widek, S. Scheicher, R. Stollberger, and T. Schwark. "Cause of death or caused by death: Differentiation of thromboemboli and post-mortem clots using quantitative MRI". In: *Proceedings of the 25th Annual Scientific Meeting of the ISMRM*. [Poster]. Honolulu, Apr. 2017, p. 887

2. B. Webb, K. Baron, M. Urschler, S. Scheicher, and R. Stollberger. "Developing an approach to post-mortem MR angiography (PMMRA): Investigation of vascular retention of perfusates in ex situ porcine hearts". In: *Proceedings of the 6th Annual Meeting of the International Society of Forensic Radiology and Imaging*. [Oral]. Odense, May 2017

3. B. Webb, T. Widek, D. Kirchmeyr, H. Sprenger, and R. Stollberger. "Darstellung postmortaler Gefässe mittels MRT: Anwendung eines Schlauch- Schweinebauch-Modells zum Vergleich von MR-Sequenzen". In: *Proceedings of the 95. Jahrestagung Deutsche Gesellschaft für Rechtsmedizin*. [Oral]. Heidelberg, Sept. 2016

4. B. Webb, D. Kirchmeyr, T. Widek, M. Urschler, R. Stollberger, and T. Schwark. "Evaluation of MRI sequences and liquids potentially suitable for post-mortem vascular perfusion". In: *Proceedings of the 5th Annual Meeting of the International Society of Forensic Radiology and Imaging*. [Oral]. Amsterdam, May 2016

5. B. Webb, T. Widek, B. Neumayer, R. Stollberger, and T. Schwark. "Post-mortem reperfusion of the vascular system and examination in MRI: Temperature-dependent characterisation of perfusates and contrast simulations". In: *Proceedings of the 24th Annual Scientific Meeting of the ISMRM*. [Poster]. Singapore, May 2016

6. B. Webb, A. Petrovic, T. Schwark, and E. Scheurer. "Characterisation and systematic selection of MRI phantoms for implementation as novel knee-based reference standards". In: *Proceedings of the 32nd Annual Scientific Meeting of the ESMRMB*. [Poster]. Edinburgh, Oct. 2015

7. B. Webb, A. Petrovic, M. Urschler, and E. Scheurer. "Co-registration of photographs and MRI data: Evaluation and application of external fiducial markers in the forensic investigation of subcutaneous hematomas". In: *Proceedings of the 4th Annual Meeting of the International Society of Forensic Radiology and Imaging*. [Oral]. Leicester, Apr. 2015

8. B. Webb, T. Widek, R. Stollberger, and T. Schwark. “Temperature-dependent characterisation of relaxation parameters (T1, T2) of potential perfusates in post-mortem MR angiography (PMMRA)”. In: *Proceedings of the 32nd Annual Scientific Meeting of the ESMRMB*. [Poster]. Edinburgh, Oct. 2015

9. B. Webb, A. Petrovic, and E. Scheurer. “Correlation of MRI and externally visible findings by external fiducial markers”. In: *Proceedings of the 22nd Joint Annual Meeting of the ISMRM-ESMRMB*. [Poster]. Milan, May 2014

10. B. Webb, A. Petrovic, and E. Scheurer. “Correlation of Macroscopic and Histopathologic Findings with MRI in Forensic Examinations.” In: *Proceedings of the BMT 2013 - Dreiländertagung der Deutschen, Schweizerischen und Österreichischen Gesellschaft für Biomedizinische Technik*. Vol. BMT2013:801. [Oral]. Graz, Sept. 2013